2002

Gamma prime precipitation modeling and strength responses in powder metallurgy superalloys

Jian Mao
West Virginia University

Gamma Prime Precipitation Modeling and Strength Responses in Powder Metallurgy Superalloys

Jian Mao

Dissertation submitted to the
College of Engineering and Mineral Resources
at West Virginia University
in partial fulfillment of the requirements
for the degree of

Doctor of Philosophy
in
Mechanical Engineering

Keh-Minn Chang, Ph.D., Chair
Ismail Celik, Ph.D.
David Ulrich Furrer, Ph.D.
Bruce S. Kang, Ph.D.
Gary Morris, Ph.D.

Department of Mechanical and Aerospace Engineering

Morgantown, West Virginia
2002

Keywords: Superalloy, precipitation, U720LI, Rene88DT, modeling, simulation, cooling, gamma prime

ABSTRACT

Gamma Prime Precipitation Modeling and Strength Response in Powder Metallurgy Superalloys

Jian Mao

Precipitation-hardened nickel-based superalloys have been widely used as high temperature structural materials in gas turbine engine applications for more than 50 years. Powder metallurgy (P/M) technology was introduced as an innovative manufacturing process to overcome severe segregation and poor workability of alloys with high alloying contents. The excellent mechanical properties of P/M superalloys also depend upon the characteristic microstructures, including grain size and size distribution of γ' precipitates. Heat treatment is the most critical processing step that has ultimate influences on the microstructure, and hence, on the mechanical properties of the materials. The main objective of this research was to study the γ' precipitation kinetics in various cooling circumstances and also study the strength response to the cooling history in two model alloys, Rne88DT and U720LI. The research is summarized below:

1. An experimental method was developed to allow accurate simulation and control of any desired cooling profile. Two novel cooling methods were introduced: continuous cooling and interrupt cooling. Isothermal aging was also carried out.

2. The growth and coarsening kinetics of the cooling γ' precipitates were experimentally studied under different cooling and aging conditions, and the empirical equations were established. It was found that the cooling γ' precipitate versus the cooling rate follows a power law. The γ' precipitate size versus aging time obeys the LSW cube law for coarsening.

3. The strengthening of the material responses to the cooling rate and the decreasing temperature during cooling was investigated in both alloys. The tensile strength increases with the cooling rate. In addition, the non-monotonic response of strength versus interrupt temperature is of great interest.

4. An energy-driven model integrated with the classic growth and coarsen theories was successfully embedded in a computer program developed to simulate the cooling γ' precipitation based on the first principle of thermodynamics. The combination of the thermodynamic and the kinetic approaches provided a more practical method to determine the critical nucleation energy.

5. The simulation results proved the γ' burst theory and the existence of the multi-stage burst of γ' precipitates, which shows good agreement with the experimental data in a variety of aspects.

To my parents, ZhuoHua Mao and YiRu Li

To my husband, Wanhong Yang

To my lovely son, Charlie Yang

ACKNOWLEDGMENTS

The author wishes to express her sincere thanks to her advisor, Dr. Keh-Minn Chang, for his continuously support, encouragement, and guidance he provided in the years passed. She would like to thank her colleagues Dr. Xingbo Liu and Dr. Zhengdong Long for their constructive suggestion on thermodynamic calculation and modeling approaches. Miss Li Yang, Mr. Matthew Burris, Mr. Robert Coulter and Dr. Longzou Ma provided their assistance at different stages during the research. Their contributions are also highly appreciated.

The author would like to give Drs. David U. Furrer and Ganshu Sheng great appreciation for their generous support and constructive advice. She also appreciates the support from Diane Schwegler-Berry, NIOSH, Morgantown, WV, with the scanning electron microscope (SEM) operations.

A special thanks is extended to Dr. Wanhong Yang for his solid assistance on the thermodynamic simulation and year-round encouragement.

Finally, the author would like to acknowledge all the committee members for their time in reviewing the proposal and the dissertation, and their comments on various topics.

TABLE OF CONTENT

LIST OF FIGURES

LIST OF TABLES

LIST of EQUATIONS

$$\Delta G_m^{ideal} = RT(u \cdot (y_{Ni}^1 \cdot \log_e y_{Ni}^1 + y_{Cr}^1 \cdot \log_e y_{Cr}^1 + y_{Co}^1 \cdot \log_e y_{Co}^1 + y_W^1 \cdot \log_e y_W^1 + y_{Mo}^1 \cdot \log_e y_{Mo}^1$$
$$+ y_{Ti}^1 \cdot \log_e y_{Ti}^1 + y_{Zr}^1 \cdot \log_e y_{Zr}^1 + y_{Al}^1 \cdot \log_e y_{Al}^1 + y_{Nb}^1 \cdot \log_e y_{Nb}^1) + v(y_{Va}^1 \cdot \log_e y_{Va}^1))$$
$$= RTu \sum_i y_i^1 \log_e y_{Va}^2$$

7-17……..117

$$\Delta G_m^{xs} = y_{Ni}^1 \cdot y_{Cr}^1 \cdot y_{Va}^2 \left[\sum_v L_{Ni,Cr:Va}^v (y_{Ni}^1 - y_{Cr}^1)^v \right] + y_{Ni}^1 \cdot y_{Co}^1 \cdot y_{Va}^2 \left[\sum_v L_{Ni,Co:Va}^v (y_{Ni}^1 - y_{Co}^1)^v \right]$$
$$+ y_{Cr}^1 \cdot y_{Co}^1 \cdot y_{Va}^2 \left[\sum_v L_{Cr,Co:Va}^v (y_{Cr}^1 - y_{Co}^1)^u \right] + \ldots + y_{Al}^1 \cdot y_{Nb}^1 \cdot y_{Va}^2 \left[\sum_v L_{Al,Nb:Va}^v (y_{Al}^1 - y_{Nb}^1)^u \right]$$
$$+ y_{Ni}^1 \cdot y_{Cr}^1 \cdot y_{Co}^1 \cdot y_{Va}^2 \left[\sum_v L_{Ni,Cr,Co:Va}^v (y_{Ni}^1 - y_{Cr}^1 - y_{Co}^1)^v \right] + \ldots$$
$$= \sum_v (y_i^1 \cdot y_j^1 \cdot y_{Va}^2 (\sum_v L_{i,j:Va}^v (y_i^1 - y_j^1)^v)) + \sum_v (y_i^1 \cdot y_j^1 \cdot y_k^1 \cdot y_{Va}^2 (\sum L_{i,j,k:Va}^v (y_i^1 - y_j^1 - y_k^1)^v))$$

7-18……..117

$T_{max} = -0.3593*(dT/dt) + 1066$ 7-19……..120

$EnergyBarrier = 3.0888(dT/dt)^2 + 18.25(dT/dt) + 18.569$ 7-20……..121

$D\gamma' = 0.5764\ (dT/dt^{)-0.39}$ 7-21……..125

Chapter 1. Introduction

1.1 Introduction

Precipitation-hardened nickel-base superalloys have been widely used as high temperature structural materials in gas turbine engine applications for more than 50 years. Powder metallurgy (P/M) technology was introduced as an innovative manufacturing process to overcome the severe segregation and the poor workability of alloys with high alloying contents. Powder metallurgy process that produces a fine, homogenous, and macrosegregation-free structure through rapid cooling during powder atomization can greatly improve the workability and the mechanical properties of alloys. In addition to the improvement of segregation, the excellent mechanical properties of P/M superalloys also depends upon the characteristic microstructures including grain size and the distribution of γ' precipitates. Heat treatment is the most critical processing step that has ultimate influences on the microstructure, and hence, on the mechanical properties of the materials.

Heat treatment of P/M superalloys consists of two sequential steps: solution treatment and aging treatment. The solution temperature mainly controls the grain size during the solution treatment. Both quenching after solution treatment and aging determine the size, morphology and distribution of γ' precipitates. However, quenching process plays a much more important role in superalloy heat treatment than aging because it significantly controls the nucleation and growth kinetics of γ' precipitates and sets the stage for subsequent aging. It is found that the higher the cooling rate is, the higher the strength will be. Nevertheless, fast cooling during quenching is accompanied by the high risk of cracking and distortion of the quenched component due to the higher residual thermal stresses induced. The challenge in designing a quench process is to control the cooling rate to achieve a balance between obtaining the desired optimum properties and minimizing the possibility of quench cracking and severe shape distortion.

Thermal process simulation of heat treatment has been extensively employed to simulate temperature field and residual thermal stresses field in a quenching component to optimize the quenching procedures without expensive trials. The thermal simulation can provide information about the cooling profiles at different locations in a component. One of the goal of the thermal simulation is to predict the mechanical properties of the component by correlating the cooling profiles with mechanical properties. In this latter approach, past experiences was to take an

averaged cooling rate over a certain temperature range and find the relationship between the cooling rate and properties. Obviously, this approach can only provide approximate prediction of mechanical properties because the distribution of γ' depends upon the actual cooling profile rather than only on the averaged cooling rate.

The objectives of this research are: 1) to develop an experimental method to allow accurate control and simulation of any desired cooling profiles. 2) to experimentally study the growth and coarsening kinetics of γ′ precipitates under different cooling and aging conditions, and to establish the empirical correlations between the cooling rate, aging time and the γ′ precipitate size in both Rene88DT and U720LI superalloys, which will provide strong experimental data to support and verify simulation results; 3) to develop a simulation tool to model on-cooling γ′ precipitation, and to be able to predict the size and the size distribution of the γ′ precipitates based on the first principle of thermodynamics; 4) to experimentally study the strengthening responses of materials during cooling.

1.2 Literature review

1.2.1 Powder metallurgy superalloy

Superalloys have been introduced to the gas turbine application since 1950's. With the improvement of engine performance, new materials are required not only having high strength but also possessing good fracture mechanical properties. Two major approaches being used to improve material performances are 1) to modify the manufacture route and 2) to develop new alloy by adding more alloying elements to the alloys. However, from developing new alloy point of view, high alloying makes conventional cast & wrought process very difficult due to severe segregation and poor workability of the materials. Powder metallurgy technology was then introduced and led to the development of the first generation powder metallurgy (P/M) superalloys, such as Rene'95, IN100, MERL76, and Astroloy. The manufacturing route of P/M superalloys and typical microstructure of superalloy powder are shown in Figure 1.1[1].

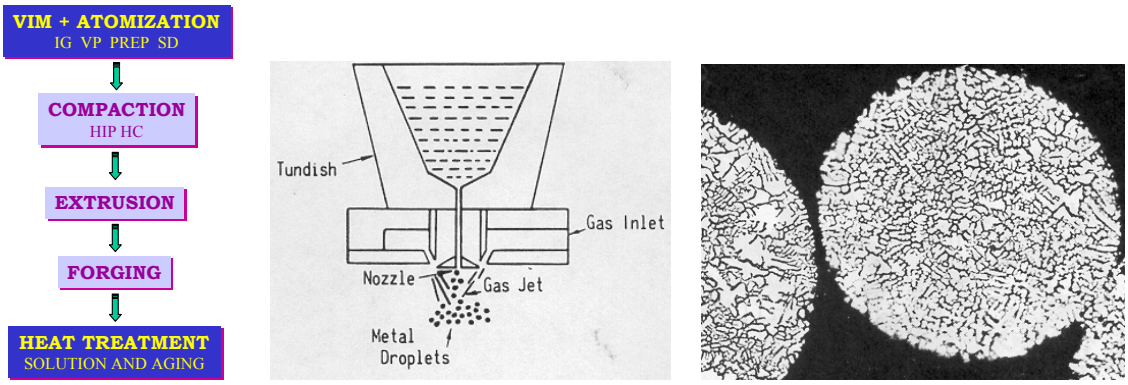

a) Processing route b) Powder atomization c) Microstructure within particles

Figure 1.1 The manufacture route of P/M superalloys and typical microstructure of powder[1]

The advantage of P\M superalloys is that the segregation due to high alloying is restricted within a particle scale. Therefore, the macro-segregation is eliminated and homogeneous microstructure is produced. Rene'95 P/M superalloy was one of the most popular P/M superalloys in the aircraft engine application at the time from 1980 to 1990's because of its highest strength and fatigue properties. High strength of Rene'95 alloy is mainly derived from its high γ′ volume fraction and very fine grain size, being about ASTM 11-13. The disadvantage of this alloy was later realized for its high fatigue crack growth rate and notch sensitivity at high temperature, which limits its further application for long term service in aircraft engine.

In requirement of the further increase of engine temperature and the decrease of cost, the design philosophy of the disk alloys was changed from the strength criterion to the damage tolerant criterion. Lower fatigue crack growth rate and higher creep resistance are considered as additional critical requirements. Therefore, metallurgical control of the fatigue crack propagation in superalloys was emphasized [2]. A new alloy, Rene88DT, was then developed according to this philosophy by General Electric Co. (GE) in 1990, which aimed at improving damage tolerance of the materials. Rene88DT alloy contains less γ′, about 40%, with a very low positive lattice mismatch to the matrix, which benefits the stability for prolonged 650°C long-term service. Rene88DT alloy also shows its excellent resistance to fatigue crack growth and creep, which are contributed to supersolvus solution treatment [3]. However, because of lower γ′ content and larger grain size as compared to Rene'95, the strength level of Rene88DT needs further improvement.

N18 [4], Modified MERL 76 [5], U720LI superalloys[6] were also come into the application for advanced engines. Cast & wrought U720 alloy used to be turbine blade materials. Modified PM U720LI (low inclusion) was developed to improve the phase stability by reducing carbide and boride content. U720LI alloy has received increased interest for the application as a turbine disk material due to its good balance between mechanical properties and economic potential [7].

1.2.2 Processing-Microstructure-Mechanical property

The excellent mechanical properties of powder metallurgy (P/M) superalloys is partially due to the precipitation of ordered and coherent γ′(Ni_3Al) phase from the solid solution matrix and partially due to solid solution hardening in the γ-matrix. The distribution of γ' precipitates strongly relies on the manufacturing process, especially the heat treatment, which determines the final mechanical properties of the materials. The cooling profile during quench is the most significant parameter affecting the nucleation and growth kinetics of the γ' precipitates. If the cooling rate is fast enough to avoid or limit the formation and growth of extensive cooling γ′ precipitates during quench, a high density of fine γ′ precipitates can be subsequently developed to achieve desirable properties during subsequent aging treatment. A lot of efforts have been made to simulate the cooling curve in a component, the residual thermal stress field to avoid quench cracking, and to study the relationship between cooling rate and mechanical properties. Figure 1.2, 1.3, 1.4 show the simulation results of the cooling profiles in a quenching component, residual stress and the strength prediction as a function of cooling rate, respectively[8, 9]. It was seen in figure 1.4 that the strength increases with the increase of cooling rate. However, the strength gained from fast quenching would be limited by the possibility of quench cracking or severe shape distortion due to high thermal stresses induced [10, 11,12].

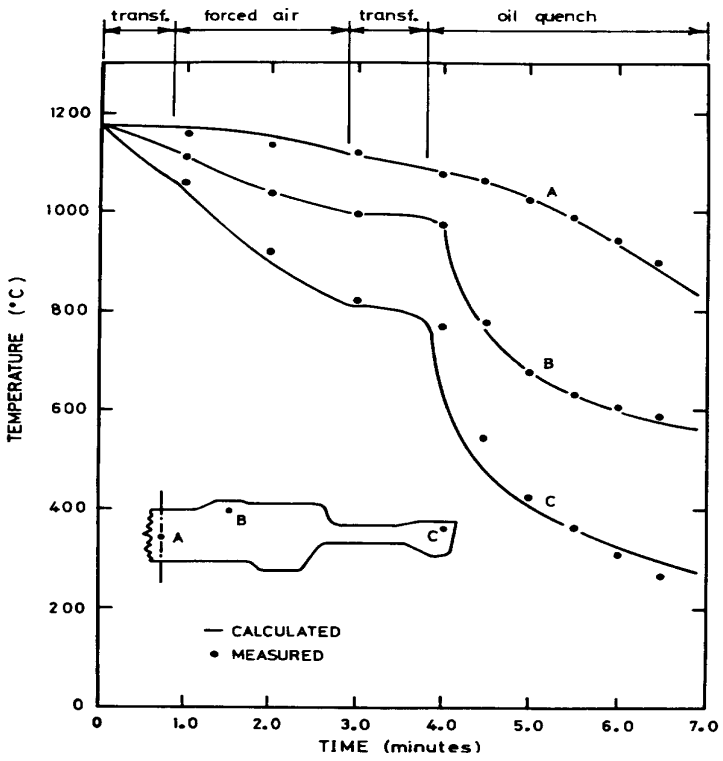

Figure 1.2 Predicted cooling curves in a disk, compared with experimental ones[8]

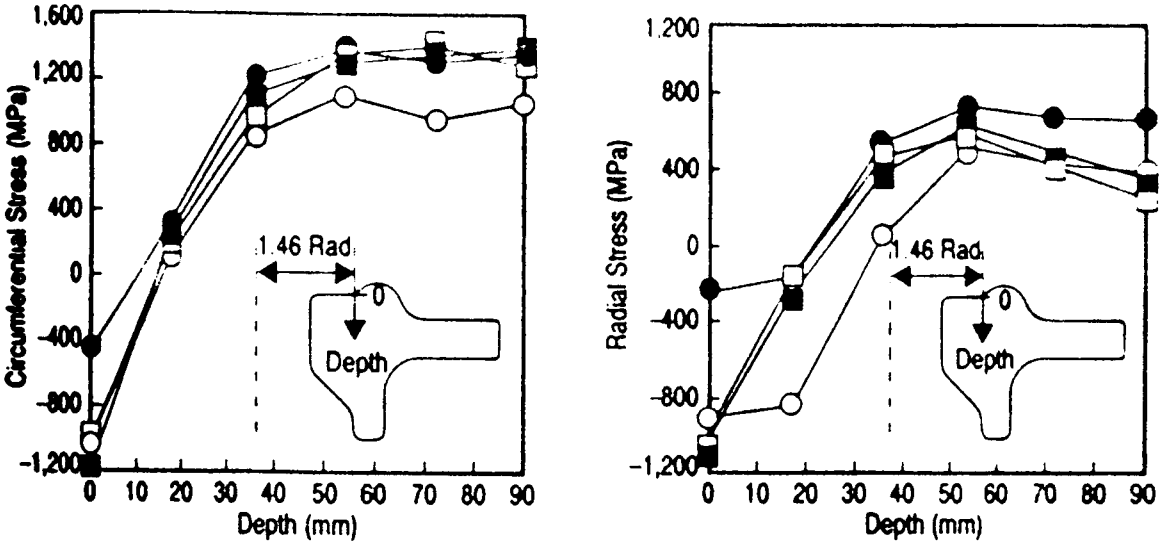

Figure 1.3 Calculated on-cooling residual stress in a disk[9]

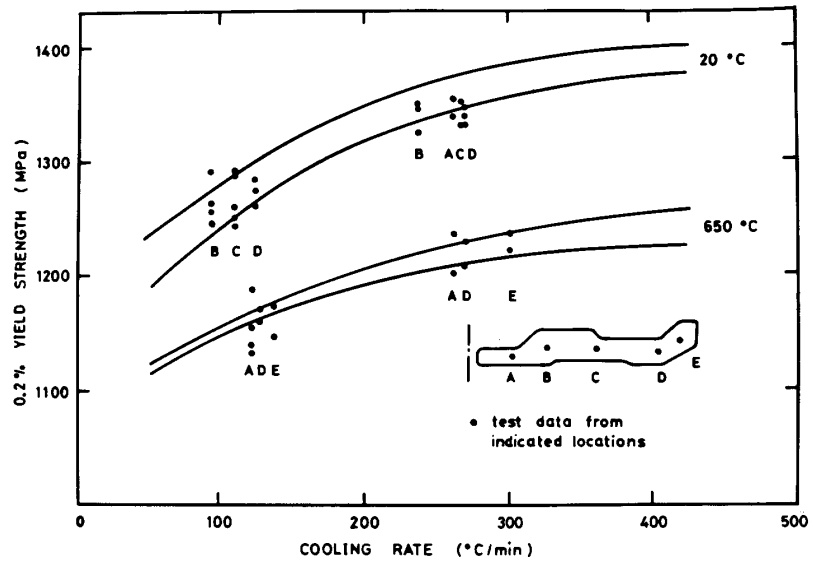

Figure 1.4 Calculated and experimental yield strength as a function of cooling rate in alloy 901[9]

The problem with accurately characterizing the relationship between cooling rate and mechanical properties is associated with the description of the cooling rate itself. Traditional cooling studies were mostly conducted by quenching a component into different quenchant bath after holding it at the solution temperature for a certain period. Another method for obtaining different cooling rates was the Jominy Bar Test, which yields different cooling rate along different location of the quenched bar [13]. In both cases, the cooling rate depends upon the heat transfer coefficient of the quenchant, which varies as a function of decreasing temperature during quenching [14,15]. In consequence, the cooling rate varies also with the decreasing temperature. As a result, using an average cooling rate within a temperature range can only produce an approximate relationship between cooling rate and mechanical properties because the size of precipitates are really determined by the actual cooling profile rather than the average cooling rate. Therefore, identification of the size of cooling precipitates as a function of real cooling profile becomes a key issue in accurate modeling of γ′ precipitation, and then prediction of mechanical properties.

1.2.3 Precipitation theory in isothermal aging

Three types of gamma-prime are identified according to observations: primary, cooling and aging γ′. Primary γ′ are those remained precipitates from previous process during sub-solvus solution treatment. During supersolvus solution treatment, all primary γ′ are dissolved. Cooling γ′ precipitates are referred to the precipitates formed only during quench. Aging γ’ precipitates are

those formed during subsequent aging treatment. A number of precipitation models have been proposed to analyze the γ′ precipitation kinetics during isothermal aging and a few focus on continuous cooling precipitation [13, 16]. Numerical simulation has recently been introduced to simulate the γ′ precipitation on some alloys.

1.2.3.1 Precipitation theory for isothermal aging

Three basic steps are considered to be involved in γ′ precipitation during isothermal aging, which are nucleation, growth and coarsening. The theoretical formulations of γ′ precipitation are described in this section.

Nucleation

According to the classic nucleation theory, nucleation is an energy driven process. As solute γ-matrix is heated up to a supersolvus temperature and quenched from that temperature, new γ′ precipitates will nucleate from the saturated γ-matrix. The Gibbs energy changes due to the nucleation of new γ′ phase can be expressed as [17]:

$$\Delta G = V_{\gamma'} \cdot (\Delta G_V + \Delta G_E) + A_{\gamma'} \cdot \sigma$$

where

ΔGv — chemical free energy per unit volume, which is the driving force of the nucleation.

ΔG_E — elastic strain energy per unit volume, which is induced by the lattice misfit between matrix and precipitate

σ — interface energy between the matrix and the precipitate

V — volume of the nucleus of γ' precipitate, which is equal to $V_{\gamma'} = \frac{4}{3}\pi \cdot r^3$

$A_{\gamma'}$ — interface area between the matrix and the nucleus, $A_{\gamma'} = 4\pi \cdot r^2$

When the volume free energy becomes big enough to overcome the strain energy and interface energy, the nucleation occurs. As shown in Figure 1.5, there exists a critical radius, which is obtained by zeroing the first order derivative of ΔG. Then the critical nucleus size and the critical free energy can be derived:

$$r^* = \frac{2\sigma}{\Delta G_V + \Delta G_E}$$

$$\Delta G^* = \frac{16\pi \cdot \sigma^3}{3(\Delta G_V + \Delta G_E)^2} = \frac{4\pi\sigma}{3} r^{*2}$$

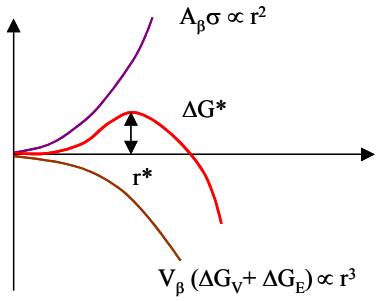

Figure 1.5 Schematic of the free energy of nucleation [17]

When nucleus size equals to the critical size, the possibility of disappearance and growth of nucleus is the same. When an additional atom happens to jump onto the nucleus, the nucleus size becomes larger than the critical size. In that case, the nucleus will survive and grow stably. As a result of it, the total free energy of the system decreases with the continuing growth of the nucleus.

Based on the classic nucleation theory, the steady-state nucleation rate I (per unit volume) in a condensed system is introduced to determine the amount of nucleation, which is given as [17]:

$$I = n_v A^* \nu \exp(-\frac{\Delta G_m}{kT}) \exp(-\frac{\Delta G^*}{kT})$$

where

ν — atom vibration frequency;

ΔG_m — atom active energy;

$\nu \exp(-\frac{\Delta G_m}{kT})$ — the frequency of the atom nearby the nucleus surface jumping into the nucleus;

A* — the number of the sites on the surface of the critical nucleus which can accept the atoms;

n_v — the number of the atomic site per unit volume which can form nucleus.

The nucleation rate can also be expressed in an alternative form: [18]

$$I = N_e \nu_0 \beta \left(\frac{\Delta G_n^*}{3\pi kT} \right) \exp\left(-\frac{\Delta G_n^* + \Delta g}{kT} \right)$$

where N_e is the number of atoms per unit volume, ν_0 the atomic vibration frequency, β the ratio of surface to interior atom numbers in R* and Δg is the activation energy for the growth of the

nucleus, which is essentially the activation energy of long range diffusion. ΔG_n^* is the molar critical free energy for the nucleation.

The difficulty in calculating the nucleation rate is that a lot of empirical equations have to be introduced to determine those coefficients based on either hypothesis or experimental results[13].

The chemical free energy ΔG_v is related to the supersaturation. Increasing the supersaturation, which means increasing the cooling rate, will increase the ΔG_v, thus decrease the critical free energy ΔG^* and critical nucleus size r*. The strain energy ΔG_E is related to the lattice misfit of alloy. The smaller absolute lattice misfit is, the lower strain energy ΔG_E is, then the smaller critical nucleus is needed.

To determine the nucleation rate the volume free energy (driving force) δG_p (= ΔG_v+ΔG_E) was calculated as a function of the actual supersaturation. The plotting of critical radius r* vs supersaturation ΔC=Ce-Cm is given by H.Wendt [18], as shown in Figure 1.6. It indicates that the critical nucleus size decreases dramatically with the increase of supersaturation in matrix and increase of δG_p. Here an assumption was made that the nucleus is of the same composition as the γ-bulk phase in equilibrium with the matrix. This cannot be true for the modeling of the cooling precipitation, because the composition of γ' precipitate is a function of the concurrent temperature.

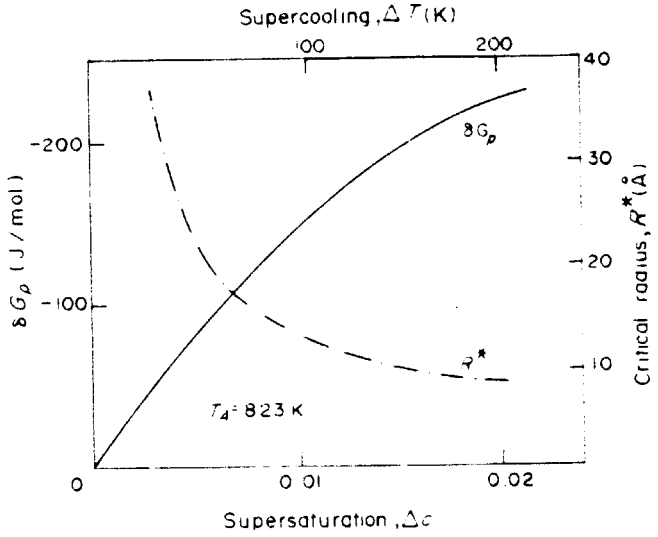

Figure 1.6 Plotting of critical radius R* vs supersaturation ΔC [18]

Growth

The growth of particle is driven by the reduction of the free energy, i.e., the free energy difference between new precipitate and matrix. Figure 1.7 plots the free energy vs. composition, which shows that the formation and growth of new precipitates will lower the free energy as the composition of matrix moves from X_0 to X_α. The growth of the nucleus is proved as a long-distance diffusion process of solute elements. During the growing, the interface between nucleus and matrix moves from the particle into matrix, as shown schematically in Figure 1.8. The interface immigration rate is given as [17]:

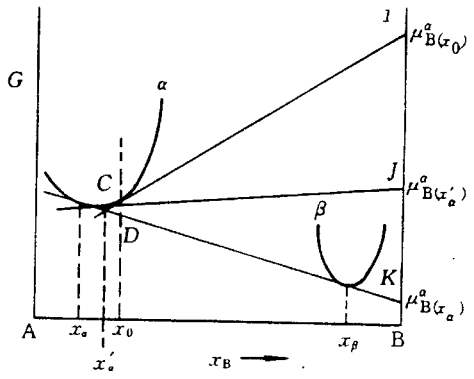

Figure 1.7 Free energy variation with composition[17]

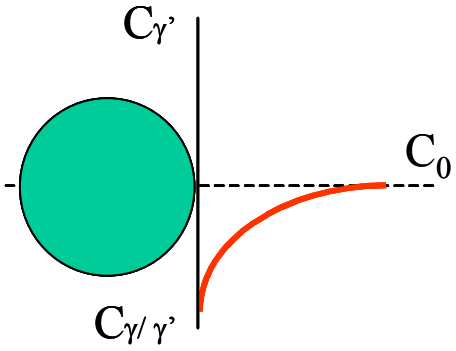

Figure 1.8 Concentration distribuition at the interface and the boundary condition

$$\frac{dr}{dt} = \frac{D}{(C_{\gamma'} - C_{\gamma/\gamma'})}\frac{\partial C}{\partial r}$$

Based on Fick's second law, for a sphere particle nucleation, the concentration with respect to time is given as:

$$\frac{\partial C}{\partial t} = \nabla(D\nabla C)$$

$$\frac{\partial C}{\partial t} = \frac{1}{r^2}\frac{\partial}{\partial r}(Dr^2\frac{\partial C}{\partial r})$$

where the initial condition is: $C(r,o)=C_0$; the boundary conditions are $C(\eta,t)=C_{\gamma/\gamma'}$ and $C(\infty,t)=C_0$. Combining with the boundary conditions, the analytical solution for above partial differential equation is obtained, which is given as:

$$C(r,t) = C_0 + (C_{\gamma/\gamma'} - C_0)\frac{\varphi_j(r/\sqrt{Dt})}{\varphi_j(\eta/\sqrt{Dt})}$$

where $\varphi_j(x) = \int \xi^{1-j} \exp(-\xi^2/4) d\xi$

Two dimensionless parameter α_j and Ω are introduced after a series of substitutions, the interface immigration rate is obtained as:

$$v = \frac{dr}{dt} = \Omega \frac{(\alpha_j)^{1-j}}{\varphi_j(\alpha_j)} \sqrt{\frac{D}{t}} \exp(-\frac{\alpha^2{}_j}{4})$$

$$(\alpha_j)^j = 2\Omega \frac{\exp(-\alpha_j^2/4)}{\varphi_j(\alpha_j)}$$

where $\alpha_j = r/\sqrt{Dt}$ — dimensionless growth coefficient

and $\Omega = (C_0 - C_{\gamma/\gamma'})/(C_{\gamma'} - C_{\gamma/\gamma'})$ — dimensionless supersaturation parameter

where C_0 is the initial composition of the matrix and $C_{\gamma/\gamma'}$ is the matrix composition at the interface between the precipitate and the matrix.

Some assumption had been made to solve the above equation. It assumed that diffusivity is not a function of the concentration. As a new phase grows, the diffusion field does not overlap between each other. So the growth is in an infinity matrix.

Coarsening

The original theory of volume-diffusion controlled coarsening was developed by Lifshiz and Slyozow [19] and Wagner [20](LSW theory). The precipitate coarsening involves competitive growth process in which the larger particles grow by consuming smaller one, while the volume fraction of precipitates in the system remained same even the total number of precipitates decreses. The driving force of coarsening is the reduction in interfacial energy of the system. The rate of coarsening is governed by the mass transfer rate from the shrinking particles to the growing ones through the γ-matrix. The scheme of the mass transfer is shown in Figure 1.9. Based on the LSW coarsening theory, the mass transfer between growing particle and shrinking particle is given as [17]:

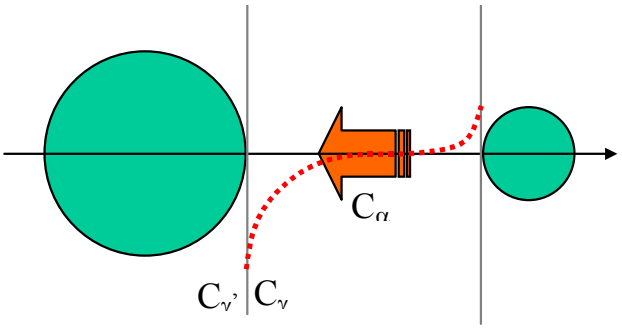

Figure 1.9 Mass transformation during coarsening

$$v 4\pi r_1^2 (C_{\gamma'} - C_{\gamma/\gamma'}) = 4\pi r^2 D \frac{dC}{dr}$$

$$\int_{r_1}^{\infty} \frac{dr}{r^2} = \int_{C_{\gamma/\gamma'}}^{C_{\gamma/\gamma'}} \frac{D}{r_1^2 v (C_{\gamma'} - C_{\gamma/\gamma'})} dC$$

By integrating above equation, we get :

$$v = \frac{D(C_{\bar{\gamma}} - C_{\gamma/\gamma'})}{r_1 (C_{\gamma'} - C_{\gamma/\gamma'})} = \frac{dr}{dt}$$

According to the Gibbs-Thomson equation,

$$C_{\gamma/\gamma'} = C_0 (1 + \frac{2\sigma V_m}{RTr})$$

Therefore, the coarsening rate is calculated as:

$$\frac{dr}{dt} = \frac{2D\sigma V_m C_0}{(C_{\gamma'} - C_{\gamma/\gamma'})RT} \cdot \frac{1}{r_1} (\frac{1}{\bar{r}_1} - \frac{1}{r_1})$$

From the above equation, the maximum coarsening rate is achieved by the particles having a radius of $r_1 = 2\bar{r}_1$. If particle grows at the maximum rate, then at time t, the particle size can be calculated by:

$$\bar{r}_1^{-3} - \bar{r}_0^{-3} = bt \quad \text{with} \quad b = \frac{3\sigma D C_e V_m}{2RT}$$

where: $\bar{r}_1$ = mean particle radius

$\bar{r}_0$ = mean particle radius at the onset of coarsening

σ = interface energy of the particle

D = diffusion coefficient of the solute in the matrix

C_e = equilibrium solute concentrition; and

V_m = molar volume of a precipitate.

This theory is based on the assumption of small and almost constant volume fraction of the precipitates and misfit-free spherical particles. However, the volume fraction is usually as much as 0.6 after aging in nickel base heat resistance alloys. When the volume fraction of precipitates is large in alloys, as in isothermal aging condition, the volume fraction effect cannot be neglected since the diffusion fields of the particles overlap and elastic fields are generated as a result of lattice mismatch between the precipitates and matrix.

Another theory, the continuum diffuse-interface phase-field theory, was proposed to take into account the elastic energy and interaction of particles. In the continuum phase-field model[21], a two-phase microstructure in a binary system is described by a composition field C(r), which describes the spatial compositional distribution, and/or a structural order parameter field, η(r), which distinguishes the structural difference between the two phases. To specified the thermodynamics of two-phase mixture at a given temperature, local free energy density function is employed:

$$f(c,\eta) = \frac{A_1}{2}(c - C_1)^2 + \frac{A_2}{6}(C_2 - c)^2 \sum_1^3 \eta_i^2 - \frac{A_3}{3}\prod_1^3 \eta_i + \frac{A_4}{24}\sum_1^3 \eta_i^4 + \frac{A_5}{24}\sum_1^3 \eta_i^2 \eta_j^2$$

where C_1 and C_2 are constants close to the equilibrium compositions of two phases. A1, A2, A3, A4, A5 are positive constants which are functions of composition and temperature. The total free energy of an inhomogenuous system with isotropic interfacial energy is given by:

$$F = \int (f(c,\eta) + \sum_1^3 \frac{\beta_i}{2}(\nabla \eta_i)^2 + \frac{\alpha}{2}(\nabla c)^2) dV$$

where α, β_i are gradient energy coefficients.

The temporal evolution of field variables, hence the microstructure, is obtained by solving Cahn-Hilliard and Allen-Cahn equations. With thermal noise, the equations are:

$$\frac{\partial c(\vec{r},t)}{\partial t} = M\nabla^2 \frac{\delta F}{\delta c(\vec{r},t)} + \xi(\vec{r},t)$$
$$\frac{\partial \eta(\vec{r},t)}{\partial t} = -L\frac{\delta F}{\delta \eta_i(\vec{r},t)} + \zeta_i(\vec{r},t);$$

where $\xi(\vec{r},t)$ and $\zeta_i(\vec{r},t)$ are noise terms which have Gaussian distribution and satisfies the correlation condition.

Base on the phase-field theory, the 2-D coarsening of δ'-Al_3Li precipitates in Al-Li alloy was simulated. The simulation result is shown Figure 1.10[21]. In addition, 3-D simulation of coarsening of γ′ precipitates in a Ni-Al alloy was also conducted [22]. The result is shown in Figure 1.11. It was found that the elastic energy anisotropy and particle interactions influence the shape of the precipitates changing from sphere to cuboid and thin plates and also precipitate alignment along elastically soft directions. The morphology evolution plot from 3D has some similarities with the 2D result and agrees qualitatively with the experimental result. The growth exponent value obtained from the simulation is 3, which remains the same as conventional coarsening theory. The coarsening kinetics in 3D is found to be much faster than 2D by the simulation.

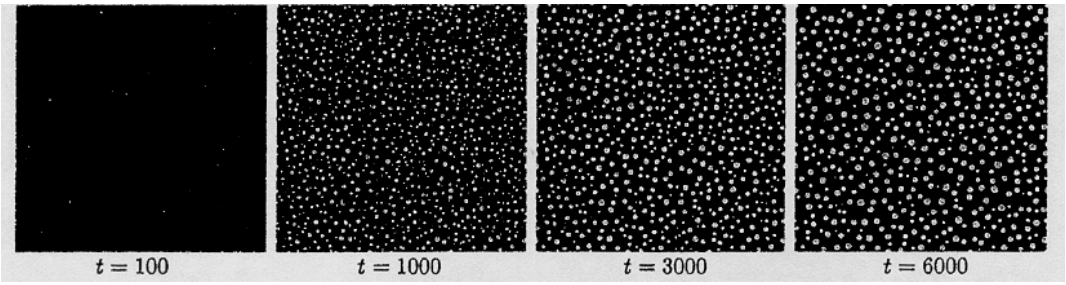

Figure 1.10 Microstrctural evolution from 2D simulation, showing nucleation, growth, and coarsening of δ' particles from an α disordered matrix[21]

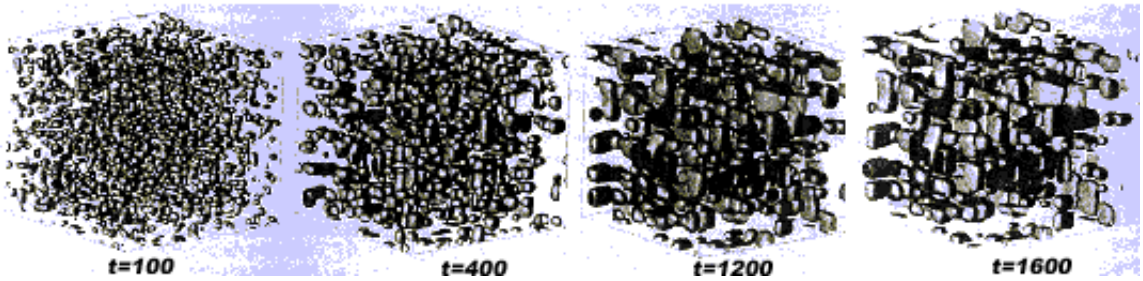

Figure 1.11 Morphological evolution of γ' precipitates from 3D simulation in a Ni-Al alloy[22]

The assumption of spherical particles, no strain, and small volume fraction of precipitate in LSW model results in over-prediction of γ′ size for slow cooling and under-prediction for fast cooling. A modified model based on the volume fraction correction yielded closer results to the actual

isothermal test data. The work has been done on MERL76 [16] to correct the basic model through comparison of precipitation theory. However, this correction was proved to be not effective for the continuous cooling. It was suggested that an accurate model would have to calculate the supersaturation due to the undercooling for each step. This supersaturation is to be used to determine the volume of γ′ that would precipitate out of solute matrix in that cooling step.

The other theories such as MLSW(modified Lifshiz-Slyozov-Wagner) and LSEM(L-S encounter modified), and KE(Kawasaki-Enomoto) [23] and BW(Brailsford-Wynblatt), BWEM(B-W encounter modified), and the VG (Voorhees-Glicksman) have also been proposed, in which the volume fraction of precipitates, elastic strain and elastic interaction was taken into account. The comparison among some of these theories such as BW, BWEM models was done by MacKAY [24]. It was found that although the cubic law was observed during coarsening, none of the presently available coarsening theories showed complete agreement in particle size distributions (PSD's) with the experimental data. These discrepancies were thought to be due to elastic coherency strains that were not considered by the available models. In addition, it was found that increasing the Mo content significantly influenced the PSD's and decreased the coarsening rate of the γ′, as a result of increasing the magnitude of the lattice mismatch [].

1.2.3.2 Diffusion activation energy in coarsening

The precipitates size vs. aging time at different temperatures were studied [24]. By plotting the size of the precipitates versus time, it was found that the relationship between cubic of the precipitates size and aging time obeys a linear law, as seen in Figure 1.12. This is usually called as cubic rate law. The slope of the linear line is called coarsening rate constant, k. Therefore, for different aging temperature, we can obtain different k based on the following equation:

$$r^3 = kt$$

$$k = A\frac{C_e}{T}\exp(-\frac{Q}{RT})$$

Apply logorism,

$$Ln\,(k \cdot \frac{T}{C_e}) = LnA - \frac{Q}{RT}$$

Assuming that the Ce/T term does not significant influences the value of Q, the plot of log k vs. 1/T is shown in Figure 1.13. Therefore, the activition energy of γ′ precipitate coarsening is then obtained from the slope of the plot in Fig.1.13.

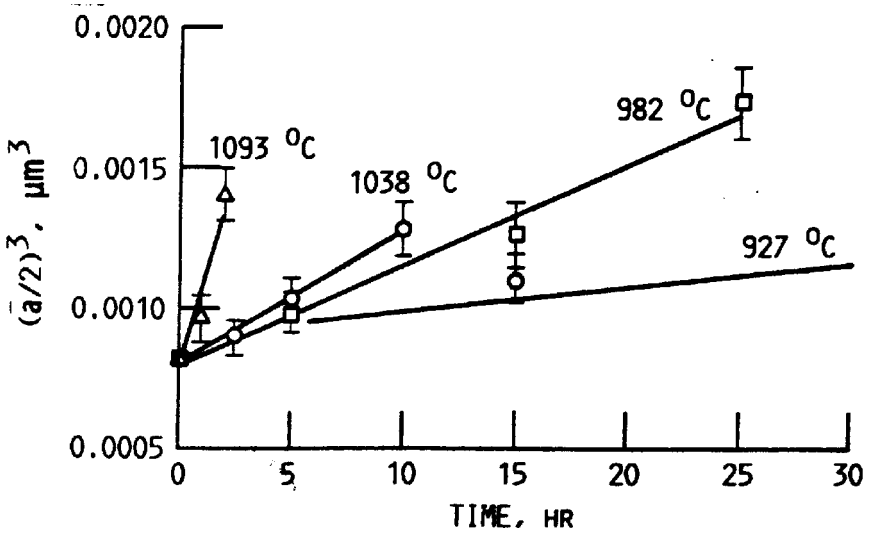

Figure 1.12 γ′ precipitate size as a function of time at the isothermal aging[24]

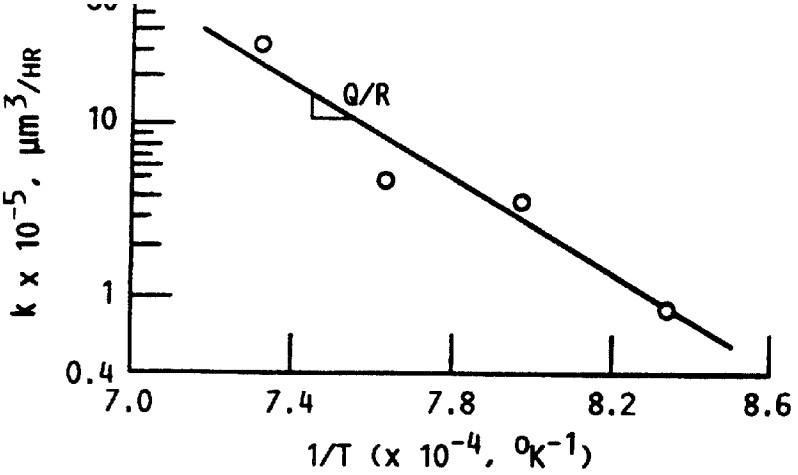

Figure 1.13 Temperature dependence of the coarsening rate k for the 14.0wt% Mo alloy [24]

1.2.4 Precipitation modeling in continuous cooling

The classic nucleation, growth and coarsening theories are derived to be used on isothermal aging. In continuous cooling, the application of the theories has been studied recently. The key difference between isothermal aging and continuous cooling is that, in isothermal case, first, the initial supersaturation of the matrix is determined by the quench after solution treatment. The critical energy is not a function of temperature. The supersaturation is consumed by the growth

and coarsening of the precipitates. Secondly, because the temperature is fixed, the nucleation and growth of precipitates is only the function of time. In addition, the diffusivity is constant, if we consider diffusivity is not a function of concentration. However, in continuous cooling, there is a complex process of supersaturation generation due to continuous cooling and supersaturation consumption as a result of nucleation and particle growth. The critical energy of nucleation is a not only the function of temperature, but also the function of composition. Diffusivity is also no longer kept constant. Only a few researches were conducted in the study of the precipitation under continuous cooling [13]. The research uses numerical tool to simulate the γ′ precipitation. The concept is:

1) Integrate the analytical solution from nucleation, growth and coarsening theories;
2) Set up thermodynamic database for a particular alloy;
3) Apply them to each temperature step;
4) Update the remaining solute concentration using the mass conservation;
5) Obtain the average size of cooling γ′ precipitates.

The simulation result was shown in Figure 1.14 [13]. It was found that the precipitate size increased as the temperature decreases. Figure 1.15 shows the simulated supersaturation in γ-matrix varied with decreasing temperature [13]. It was noted that there are two peaks in the chart, which is believed to be associated with the potential of two stages nucleation.

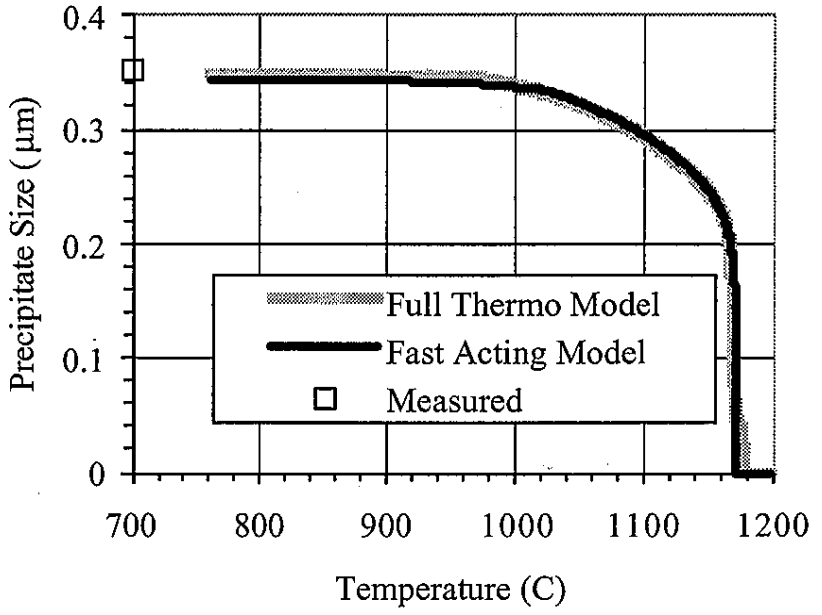

Figure 1.14 The primary cooling γ′ precipitate size predicted by the model[13]

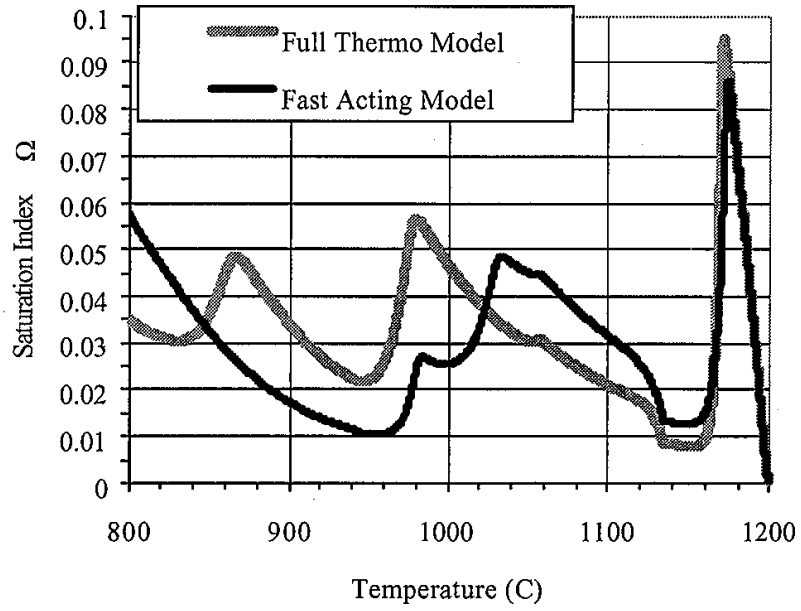

Figure 1.15 Supersaturation levels predicted using the model[13]

Figure 1.16 shows the γ′ morphology in CH98 alloy after quenching, in which the bi-modal size distribution was demonstrated.

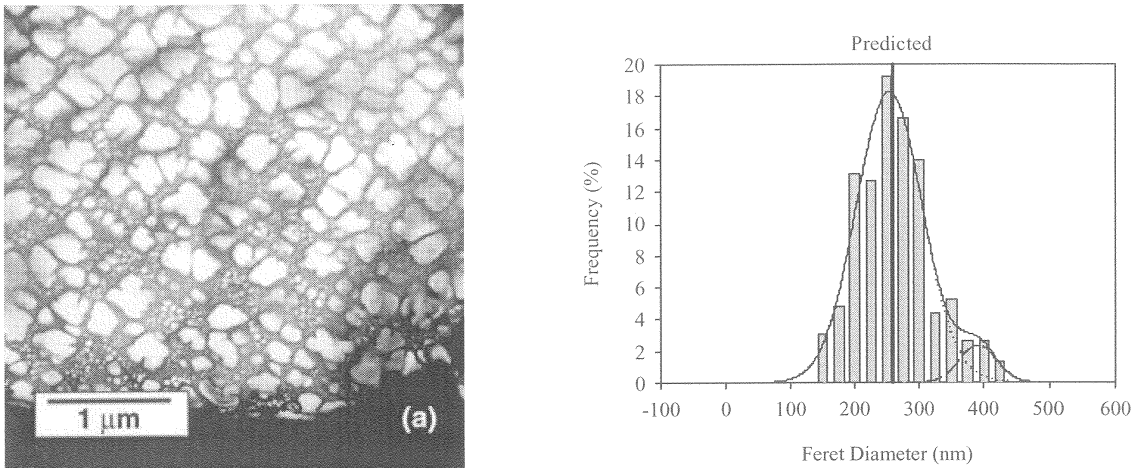

Figure 1.16 γ′ morphology and the size distribution after supersolvus heat treatment[13]

1.2.5 Experimental study on cooling precipitation

The study of precipitation and growth kinetics has been conducted experimentally on several alloys, Rene88DT, N18, MERL 76, U720LI and other Ni-Cr-Co alloys, which is described below.

R88DT

Wlodek and Kelly studied the structure in Rene88DT [3]. Specimens were subjected to a supersolvus solution for one hour, and cooled at different cooling rates, and then aged. It was found that the size of cooling γ′ precipitates decreases with the increase of cooling rate. When cooling rate is fast than about 300°C/min only one type sized cooling γ′ precipitates formed, but when cooling rate is slower than 300°C/min, two type sized cooling precipitates were observed. The two types of γ′ precipitates have different lattice mismatch. The larger ones (first burst) are formed strictly during cooling, the shape of which changes from spherical to cubical to dentritic with the decrease of cooling rate. Very small γ′ precipitates (second burst) that forms at cooling rate slower than about 300°C/min, are considered to be precipitated in the later part of the cooling cycle, which are always spherical and do not have a strong dependence on the cooling rate. The size of precipitate vs. cooling rate is shown in Figure 1.17. Diameter of the cooling γ′ precipitate can be expressed as a function of cooling rate dT/dt, and is given as [3]:

$$\mathrm{Log}D_{\gamma'} = 0.178-0.551\mathrm{Log}\,(dT/dt), \quad R^2=0.93$$

which dT/dt is in °C/min, D is in micron.

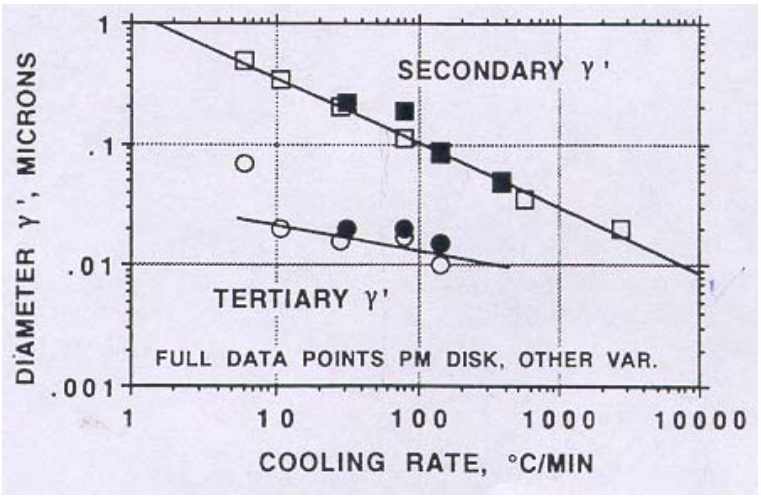

Figure 1.17 Relationship of cooling precipitates size and cooling rate in Rene88DT alloy [3]

The precipitation of the very fine γ′ and its growth is a main structural activity during aging [3]. The existence of tertiary γ′ is a combination of time and temperature effects. At long term exposure, the growth of these very fine γ′ stopped when these precipitates reached a diameter of some 0.05μm.

Superior properties of Rene88DT is due to its high γ′ content and the low positive mismatch (mismatch of 0.05%) of the γ′ that allows a highly coherent and finer γ′ precipitation [3]. Low mismatch alloy not only produces the highly coherent precipitate, but also reduces the free energy change that must be overcome on nucleation, and thus increases the nucleation rate of the γ′ and forms finer γ′ precipitates compared to other disk alloys. Low mismatch is a direct result of the judicious use of tungsten, which, unlike Mo, increases the γ phase lattice parameter without appreciably affecting γ′ [3]. The beneficial effects of a coherent γ′ precipitates may be responsible for the relatively lower growth rate of this phase during service.

U720LI

The precipitation kinetics of γ′ on U720LI had also been studied. M.P Jackson and Roger Reed investigated the influence of cooling rate and aging temperature on γ′ precipitation [25]. It was found that secondary γ′ size decreased from 450 to 60nm as the cooling rate increases from 20K/min to 280K/min, and γ′ size exhibited a bi-modal distribution. The secondary γ′ is considered to have a diameter greater than 90nm and tertiary γ′ is less than this value. Aging treatment leads to the preferential coarsening of tertiary γ′ while the size of secondary γ′ being unaffected, as seen in Figure 1.18, which was also pointed out in the study of Rene88DT [3].

The existence of bi-modal distributions of intragranular γ′ precipitates had been rationalized by the authors in the following way. Early on quenching from the solution temperature, secondary γ′ precipitates nucleate from the supersaturated γ-matrix. As the temperature decreases further, growth of the secondary γ′ precipitates occurs with partitioning of solutes into the surrounding matrix. Eventually, the diffusion rates of solute slow down and the γ′ precipitates cannot grow fast enough to keep the supersaturation of the matrix low. After that, at a critical undercooling, the driving force for nucleation is sufficient to allow the nucleation of tertiary γ′ precipitates to occur again. According to the authors, the lattice mismatch of secondary γ′ differs from that in tertiary γ′, which is determined by surrounding chemistry and solubility of solute at different

temperature. Therefore, the lattice mismatch varies with temperature, which is listed in Table 2.1 [25].

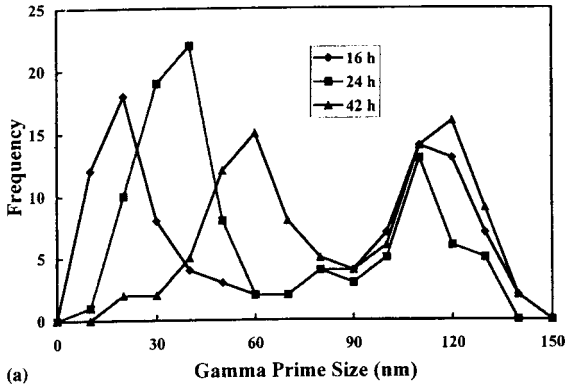

Figure 1.18 Effect of aging time on γ′ precipitate size in U720LI alloy at aging of 700°C/24hrs

Table 1-I Variation of the lattice parameter mismatch between γ and γ′ with temperature [25]

Temperature, °C	a_{γ}, A°	$a_{\gamma'}$, A°	Mismatch, %
20	3.59083	3.58862	
300	3.60367	3.60166	
600	3.61784	3.61784	
900	3.63860	3.63937	

David Furrer studied the formation of γ′ in Superalloy U720LI [26] and confirmed that there exists a multi-modal distribution of γ′ particle sizes in which each size fraction is precipitated at different temperatures and from a different chemistry γ phase. For supersolvus heat treatments, it is stated that the initial nucleation events are controlled by results from the initial precipitation. Subsequent nucleation events depend on the initial precipitation, subsequent cooling path, new γ′ phase nucleation kinetics, and diffusion-controlled growth kinetics of the previously precipitated γ′. The diffusion distances are proportional to the square root of the diffusivity and time. The relationship of size and cooling rate that is in unit of °C/min is given as (Figure 1.19) [26]:

$$\text{Log } D = 0.5022-0.4712*(dT/dt), \quad R^2=0.9424$$

A TTT curve was obtained based on the cooling curves, precipitation temperature data and the γ′ morphology from metallography examination, as shown in Figure 1.20 [27]. The undercooling temperature was found to be a level ranged from 31-55°C over the cooling rates range examined (7.2~858°C/min) for different type of γ′ precipitates. It means that the sufficient undercooling for

the γ′ nucleation varies with cooling rate, e.g., the higher the cooling rate, the larger the undercooling is required.

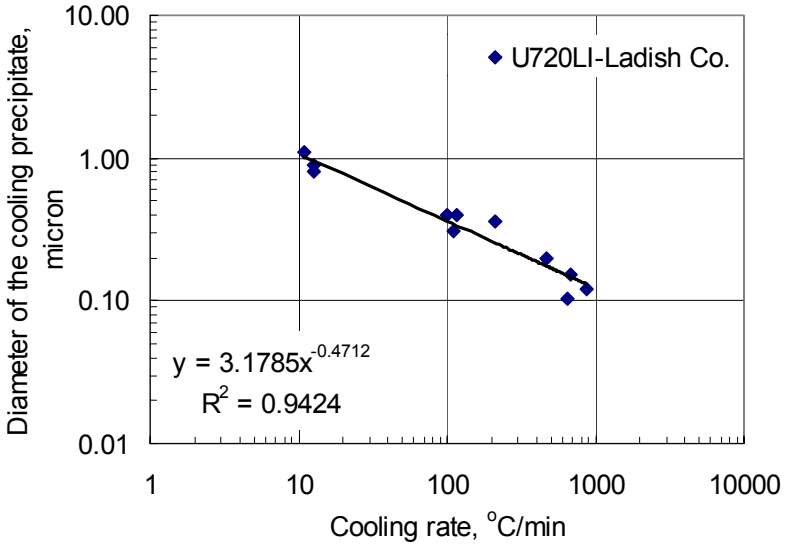

Figure 1.19 Variation of the size of cooling precipitates with cooling rates in U720LI [26]

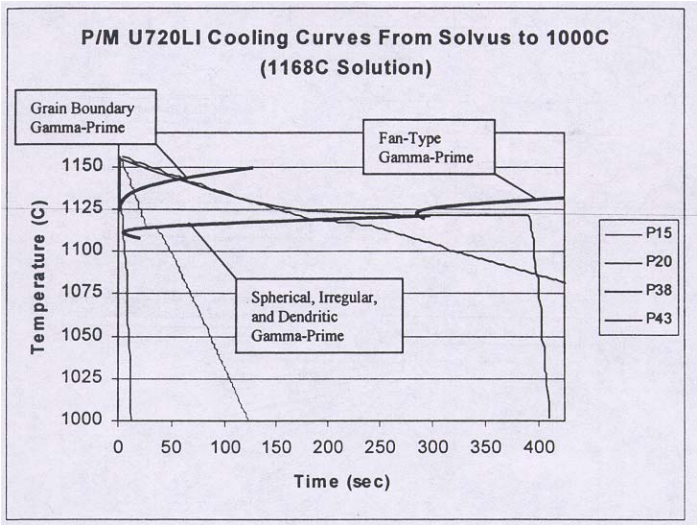

Figure 1.20 TTT curves during cooling correponding to the various forms of γ′ in U720LI [27]

N18

Study of the cooling precipitation on N18 had been done by Wlodek et al [28]. Three γ′ sizes was found in aged specimens. All these γ′ precipitates exhibited a negative mismatch to the matrix, the degree of mismatch being –0.23% for the primary fraction and –0.38% for the tertiary which

is probably coherent with the matrix. Relationship of the secondary γ′ precipitates size and the cooling rate is list below and shown in Figure 1.21.

$$LogD=0.257-1.97*10^{-3}(dT/dt)\ (°C/min),\quad R^2=0.95$$

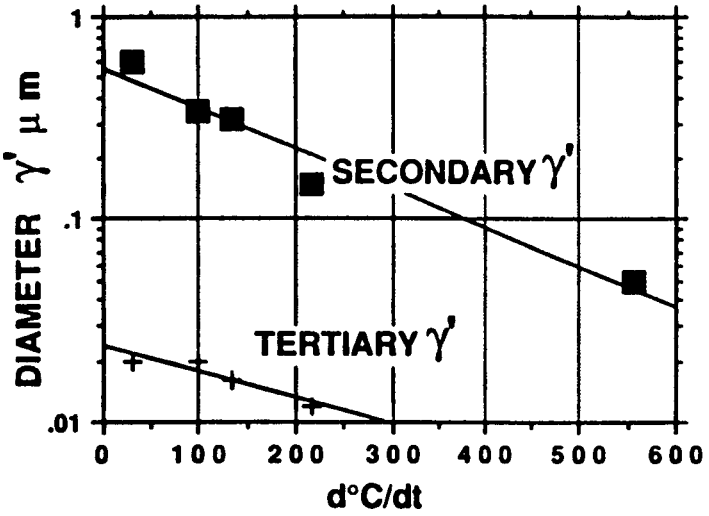

Figure 1.21 Cooling precipitates size as a function of cooling rate in N18 alloy [28]

It is believed that the fine tertiary γ' precipitates (<0.02μm) is formed at about 700-870°C in N18, essentially on or after water quenching. Each of three γ′ structures is formed under completely different conditions, accounting for the varying γ′ chemistry and lattice parameter. Long term exposure results in a rapid reduction in the fine γ′, particularly above 700C. Excellent properties of N18 are associated with the presence of the ultrafine, aging γ′ precipitates whose solution dictates the useful temperature maximum for this alloy. Gayraud [4] studied the kinetics of γ′ precipitation in N18 alloy. The relationship between the secondary precipitate size and the cooling rate obeys a $(dT/dt)^{-1/2}$ law, seen in Figure 1.22. The change of the γ′ morphology with the cooling rate was proposed in the way shown in Figure.1.23.

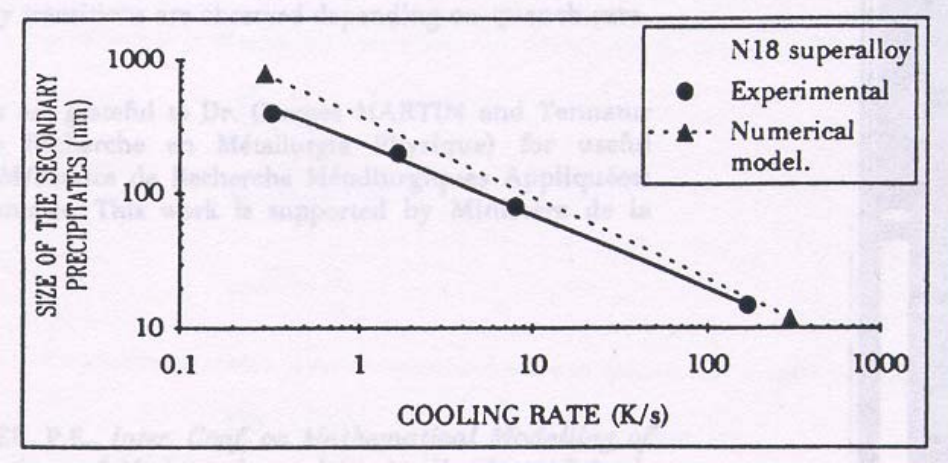

Figure 1.22 Experimental and calculated size of the secondary γ′ precipitates versus cooling rate[28]

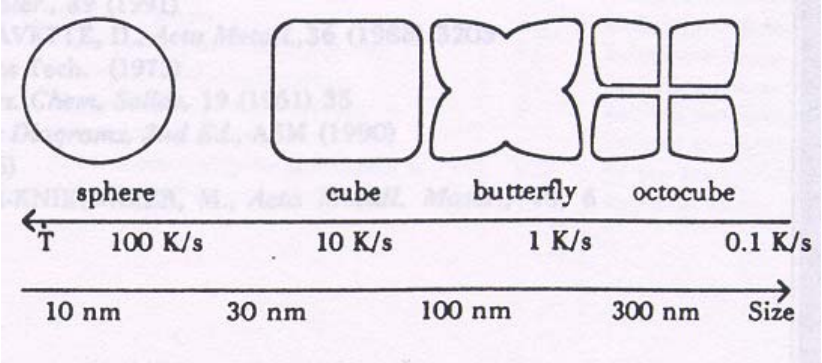

Figure 1.23 Morphology transitions of the secondary γ′ precipitates from rapid to slow cooling rates: spherical, cuboidal, butterfly distortion and octocuboidal[28]

Effect of continuous cooling rate on the precipitation of γ′ in other Nickel-based superalloy, like MERL76 [16], Rene95 [29], and Wasploy [30] are also studied. It is concluded that the morphology and the size of cooling γ′ precipitates was a strong function of cooling rate from solution temperature. Bi-modal precipitation was observed in several alloys. When cooling rate is higher than 300°C/min, no tertiary γ′ precipitates were examined. Moreover, the size of the tertiary γ′ precipitates does not strongly depend on the cooling rate. In addition, the mismatch of γ-matrix and γ′ precipitates is differed in different alloys and also between secondary and tertiary γ′ precipitates.

1.2.6 Strengthening theory

The strengthening of alloys by precipitates can be expressed in the simplest form in terms of alloy hardness vs. particle size. Such a curve for Ni-22%Cr-2.8%Ti-3.1%Al alloy is seen in Figure 1.24 from Mitchell [31]. On the ascending curve, γ′ precipitates are cut by dislocations, on the descending curve, dislocations by-pass γ′ precipitates. Several basic factors contribute to the magnitude of hardening: anti-phase boundary (APB) and fault energy of γ′, γ strength, γ′ strength, coherency strains, volume percent γ′ precipitates, particle size of γ′ precipitates, diffusivity in γ′ and γ′, and, possibly, γ-γ′ module mismatch [31].

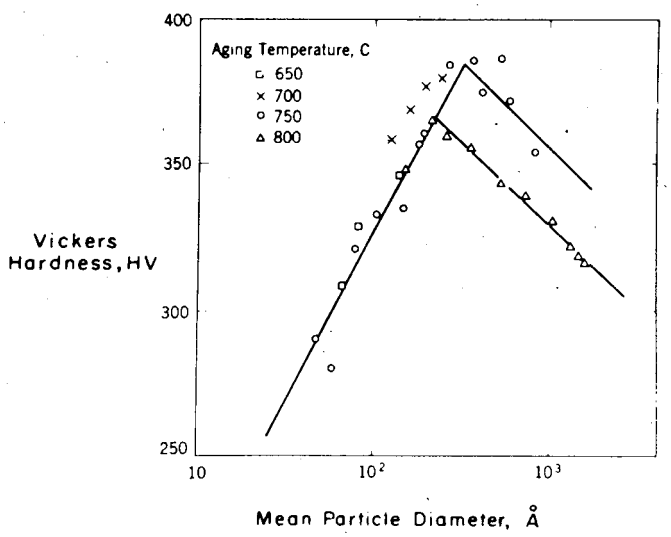

Figure 1.24 Effect of particle size on hardness of Ni-Cr-Al-Ti alloys [31]

Mott and Nabarro recognized that the strain field resulted from mismatch between a particle and the matrix would be a source of strengthening. The estimation of the strengthening due to coherency strain is [32]:

$$\Delta\sigma = 6G\left(\frac{r}{b}\right)^{1/2} f^{1/2}\varepsilon^{3/2}$$

where r is the particle size, f is the volume fraction and ε is the measure of the strain field.

Strength due to ordered particles is responsible for the good high-temperature strength of many superalloys. If the particles have an ordered structure then anti-phase boundaries are introduced when they are sheared. The increment of hardening is given by:

$$\Delta\sigma = \frac{2}{\sqrt{\pi E}}\left(\frac{\gamma_{apb}}{b}\right)^{3/2} r^{1/2} f^{1/2}$$

Where γ_{apb} is anti-phase boundary energy. The model of strengthening from ordered particles depends on the details of the size and spacing of the particles.

Numbers of hardening mechanisms were proposed regarding the nature of obstacles. The application of these mechanisms and the agreement between theoretical model and experimental result varies with the alloys.

Dislocation pair cutting theory was applied to describe the precipitation hardening in U720Li alloy [25]. There are two models introduced. One is for describing the CRSS (critical resolved shear stress) for two weakly coupled dislocations to cut through ordered precipitates in a disordered matrix. The other is for describing the same motion for strongly coupled dislocations. The situations are illustrated schematically in Figure 1.25. Both models assume that low coherency strain is between the particles, which are taken to be spheres of identical size. The low mismatch between γ and γ' in U720Li and Rene88DT alloys has been recognized [3,25]. For the small particles, the CRSS $\Delta\tau_0$ is determined by the stress necessary to move weakly coupled dislocation pairs:

$$\Delta\tau_0 = \frac{1}{2}\left(\frac{\Gamma}{b}\right)^{3/2}\left(\frac{bdf}{T}\right)^{1/2} A - \frac{1}{2}\left(\frac{\Gamma}{b}\right) f$$

where Γ is the APBE (Anti-phase Boundary Energy) of the γ' in the {111} plane, $\boldsymbol{b}$ is the burgers vector of the edge dislocation in the γ matrix, d the particle diameter, f the volume fraction of the γ' precipitates, T the line tension of the dislocation and A a numerical factor depending on the morphology of the particles.

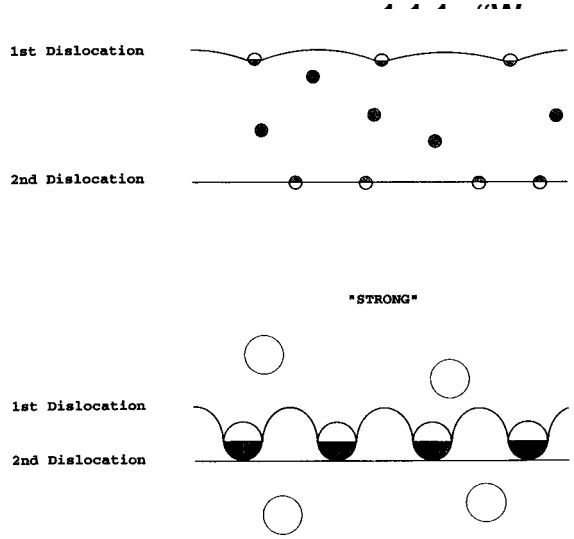

Figure 1.25 Scheme diagram of the dislacation movement mechanisms involving weak coupling and strong coupling[25]

For larger spherical particles, where dislocations cut in strongly coupled pairs, the CRSS is given by [25]:

$$\Delta\tau_0 = \frac{1}{2}1.72\frac{Tf^{1/2}w}{bd}\left(1.28\frac{d\Gamma}{wT}\right)^{1/2}$$

Where w is a constant which accounts for the elastic repulsion between the strongly paired dislocations, and which is of the order of unity.

A plot of particle diameter d versus CRSS $\Delta\tau_0$ for the two dislocations movement mechanisms [25] is presented in Figure 1.26. For cutting in weakly coupled pairs, $\Delta\tau_0$ increases monotonically with increasing d. For cutting by strongly coupled dislocations, $\Delta\tau_0$ initially increase with d then decrease. The transition value appears to be 40nm. Comparing this value with the Figure 1.18, which shows particle size histograms in U720LI, it seems that only tertiary γ' with size less than 60nm will increase the strength by cutting in weakly coupled pairs. When γ' size is larger than this value, the CRSS actually decreases with the increase of γ' precipitate size.

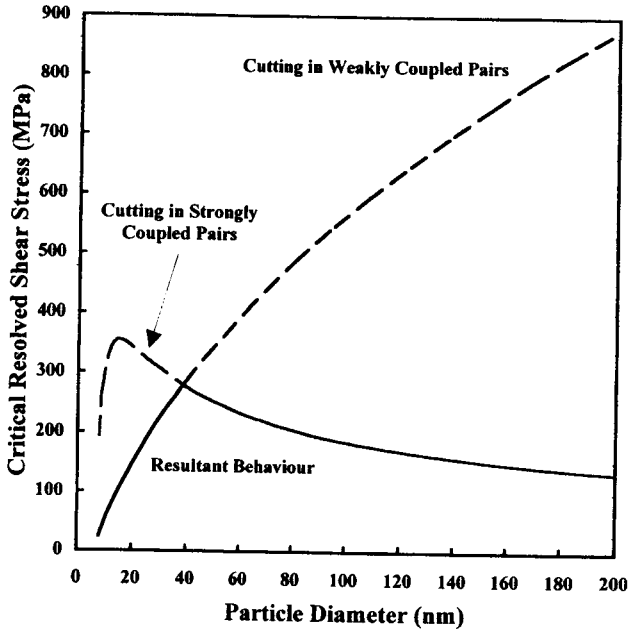

Figure 1.26 Theoretical critical resolved shear stress versus particle diameter relationships for the two deformation mechanisms at 700°C[25]

There are several other strengthening theories were summarized in Ref.[33,34]]. Precipitation hardening is directly derived by the morphology, the size and the volume fraction of γ′ strengthening phases, especially cooling precipitates, which is turned out to be affected strongly by heat treatment, including solution treatment, quenching and aging. The constitutive modeling of cooling precipitation based on the intensive understanding of the kinetics of nucleation and subsequent growth of γ′ precipitates will leverage processing, microstructure, and properties, and to provide more accurate prediction of mechanical properties of materials.

Chapter 2: Experimental

This chapter introduces the experimental techniques used to study the γ′ precipitation kinetics during quenching and aging. Related topics are also described to fulfill the research objectives, such as materials selection, equipment capacity continuous cooling / interrupt cooling /aging test procedure, metallographic examination, image processing and data analysis, and tensile test.

2.1 Materials

U720LI and Rene88DT powder metallurgy superalloys were chosen to be the model alloys in this study. Both materials were provided by Ladish Co. Inc., Cudhay, WI., and were produced by standard manufacturing processes including alloy atomization, hot isostatic pressing, extrusion and isothermal forging. Nominal compositions of alloys are listed in Table 2-I. Blank sheet specimens were cut from the rim of an isothermal forged disk in a tangential direction by a wire electrolytic-discharge machine (EDM). The specimen size is about 19×3.2×89mm, as shown in Figure 2.1. Tensile specimen was machined from the quenched blank sheet into a dog-bone shape with the size of 0.75×0.125×3.5". The cut-off parts, identified in Figure 2.1 by hatched lines, were used for the metallographic examination.

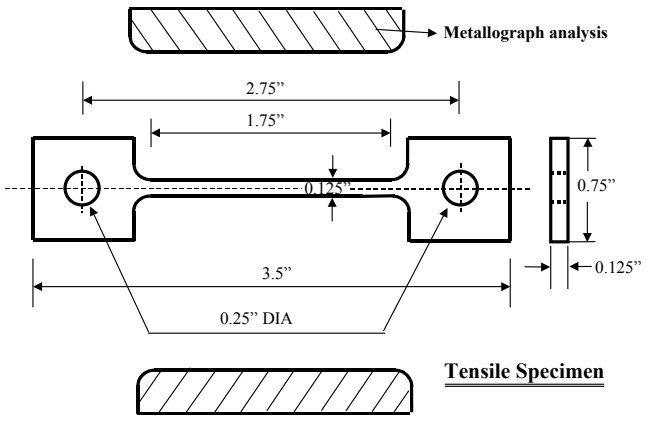

Figure 2.1 Specimen drawing for cooling study and tensile test

Table 2-I Nominal compositions of Rene88DT and U720LI superalloys

Alloy	C	S	W	Mo	Nb	Zr	Co	Al	B	Cr	Ti	Fe	Ni
U720LI	0.025	0.005	1.3	3.02		0.035	14.75	2.46		16.35	4.99	0.06	Bal
Rene88DT	0.049		3.88	4.00	0.70	0.043	12.99	1.99	0.016	15.67	3.72		Bal

2.2 Quenching system

Conventional approach for cooling study is to cool the specimen in a different quenchant after solution treatment. The cooling rate passively relies on the thermal transfer coefficient between quenchant and quenching specimen. In that case, average cooling rate is calculated from the temperature-time profile recorded by the thermo-couples spot-welded on the specimen.

Instead of using the above conventional approach, our cooling tests were conducted on a fully computer-controlled quenching system equipped with an infrared high power quartz heater [35], which is shown in the picture of Figure 2.2. The key features of the system are:

- Cooling profile is controllable. The system can be programmed in varieties of cooling pattern, such as linear cooling at a fixed cooling rate, multi-step cooling or under any other desired cooling profiles over a desired temperature range or entire cooling process.
- On-cooling data tracking makes it possible to examine real cooling profile.
- Maximum temperature capacity of the furnace is 1260°C, and the highest cooling rate can be reached to around 1050°C/min.
- Real-time multi-channel temperature control and display at a specified sampling rate;

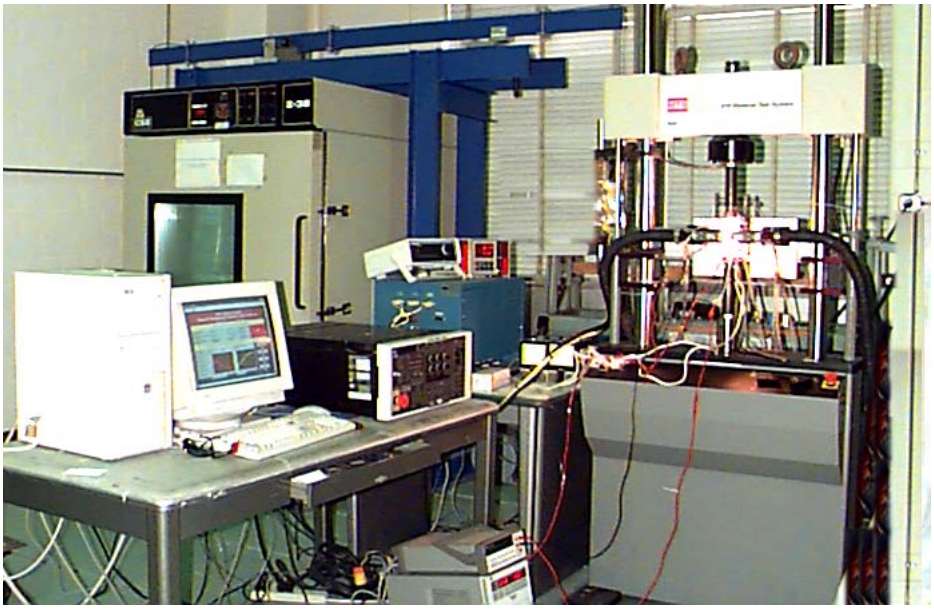

Figure 2.2 The computer contorlled quenching system

2.3 Cooling procedure design

Two cooling approaches, continuous cooling and interrupted cooling, were applied to the study of the cooling γ′ precipitation kinetics.

2.3.1 Continuous cooling study

Continuous cooling test was designed to study the effect of the linear, fixed cooling rates on the size of the cooling γ′ precipitates. Several cooling rates were selected based on the cooling rates at different locations of a model disk predicted by the computer simulation. From the continuous cooling tests, the following goals were expected to achieve:

- Relationship between linear cooling rate and the cooling γ′ precipitate size;
- Cooling precipitation responses to the real cooling profiles;
- Cooling precipitation responses to the multi-step cooling profile

2.3.1.1 Continuous cooling with fixed cooling rate

Continuous cooling was carried out by heating up the specimen to a supersolvus solution temperature, holding for a certain time, and then quenching at different controlled cooling rates. Six different cooling rates: 11°C/min (20°F/min), 27°C/min (50°F/min), 55°C/min (100°F/min), 111°C/min (200°F/min), 167°C/min (300°F/min), and natural cooling

800°C/min (1440°F/min) were used in this study. On reaching 650°C in each cooling, the specimens were rapidly quenched by turning off the power. Natural cooling was achieved by turning off the power of the quartz heater after the holding time to freeze the microstructure at high temperature. For each test, the cooling profile was recorded through a pair of thermocouples spot-welded onto the two faces of each specimen.

Figure 2.3 and 2.4 show the recorded temperature-time profiles of both Rene88DT and U720LI alloys, respectively. The solution temperatures for both alloys are 1150°C and 1175°C, which are higher than their γ′ solvus temperatures, respectively. A 5 minutes holding time at solution temperature was based on the study of the grain growth kinetics []. Linear control of the cooling processes within an interested temperature range from the solution temperature to 650°C was maintained. The comparison of the preset cooling rates and the real cooling rates obtained from recorded data fitting were listed on Table 2-II. The control accuracy of the quench system to maintain preset cooling rates over a wide range is apparent.

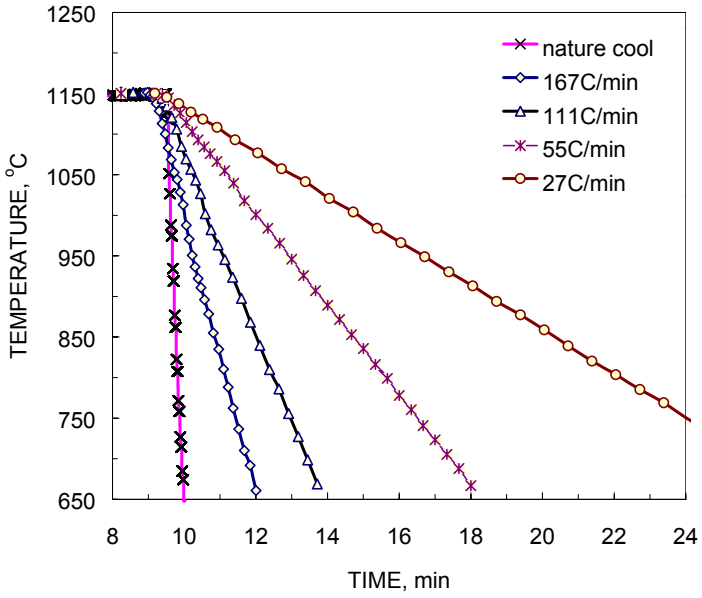

Figure 2.3 Linear cooling profiles of Rene88DT

Table 2-II The comparison of the preset and the real cooling rates in U720LI

	Cooling Rate, °C/min					
Preset	11	27	55	111	167	Nature Cooling
Measured	11.0	27.6	56.5	110.2	171.6	800.3

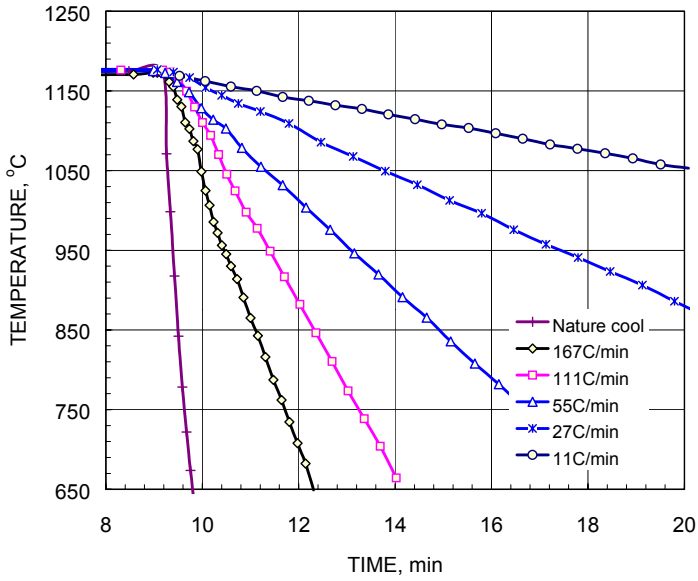

Figure 2.4 Linear cooling profiles of U720 LI

2.3.1.2 Simulating real cooling profiles

In order to simulate the cooling in a disk, the cooling profile obtained from the thermal process simulation of heat treatment of a Rene88DT model disk were input into the cooling system. Figure 2.5 shows the simulation result of the disk, which was done by Ladish Co. The cooling profile B corresponds to the corner point B at right edge in the disk, and the cooling profile A corresponds to the center point A at the left edge. These two cooling profiles were then input into the quenching system as preset cooling profiles.

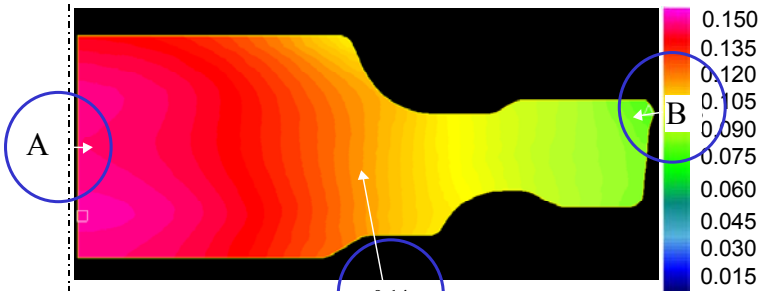

Figure 2.5 The temperature field of a quenching disk[36]

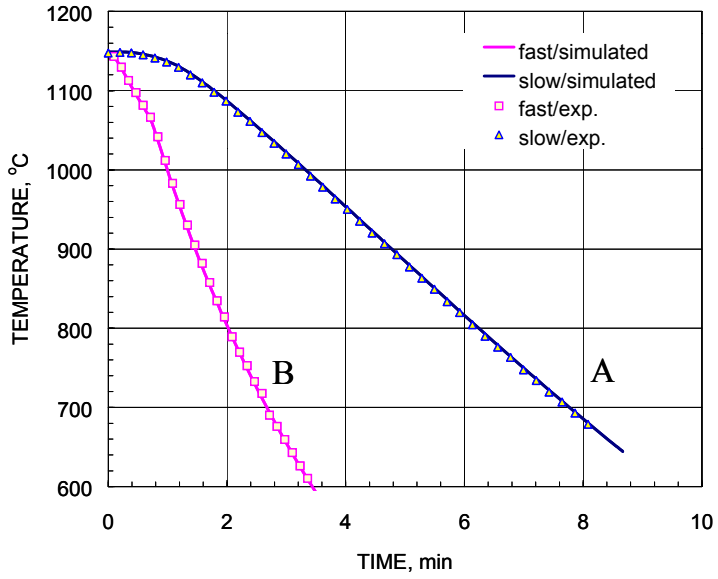

Figure 2.6 Simulated disk cooling profiles

In the Figure 2.6, the solid line is the preset input cooling profiles, and the marks in the chart represent the experimental data point recorded by the quench system. As mentioned before, the system could well simulate the input cooling profiles

2.3.1.3 Multi-step cooling

In practical disk quenching, the multi-step cooling is sometimes applied to reduce thermal stress and mitigate the risk of quench cracking. The situation was also simulated in our study.Therefore, the cooling precipitation under a multi-step cooling condition was also investigated in Rene88DT. The specimen was heated up to a solution temperature

1150°C, held for 5 minutes, then quenched at the rate of 55°C/min to an intermediate temperature, and held for another 40s, then quench again at the same cooling rate to 650°C. The specimen size was the same as the previous tests. The designed and the recorded cooling profile are shown in Figure 2.7. It was also shown the flexibility of cooling profile control through the quench system.

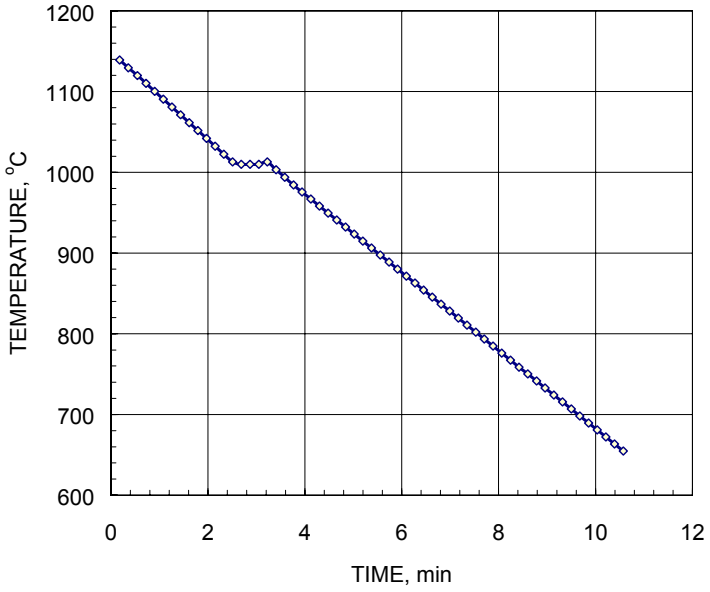

Figure 2.7 Multi-step cooling pattern

2.3.2 Interrupt cooling

Another novel cooling approach applied is interrupt cooling, which is aimed at the study of the development of cooling γ′ precipitates during a quenching process. Each individual specimen was heated up to a supersolvus solution temperature, held for 5 minutes, and then quenched at a cooling rate of 55°C/min. the solution temperatures are 1150°C and 1175°C for Rene88DT and U720LI, respectively. This test were then discontinued at a designated interrupt temperature and followed by a rapidly quenching at a rate above 800-1000°C/min to room temperature. Interrupt temperatures applied to both alloys were summarized in Table 2-III. The recorded interrupt cooling curves for Rene88DT and U720LI were shown in Figure 2.8, and 2.9, respectively. The transition points in the curves are corresponding to the each interrupt temperature during the tests. It is expected

that the rapid quenching from the interrupt temperature freezes the microstructure corresponding to the interrupt temperatures.

Table 2-III The interrupt temperatures

Rene88DT	1150°C	1093°C	1037°C	982°C	927°C	650°C	
U720LI	1175°C	1121°C	1065°C	1010°C	954°C	899°C	650°C

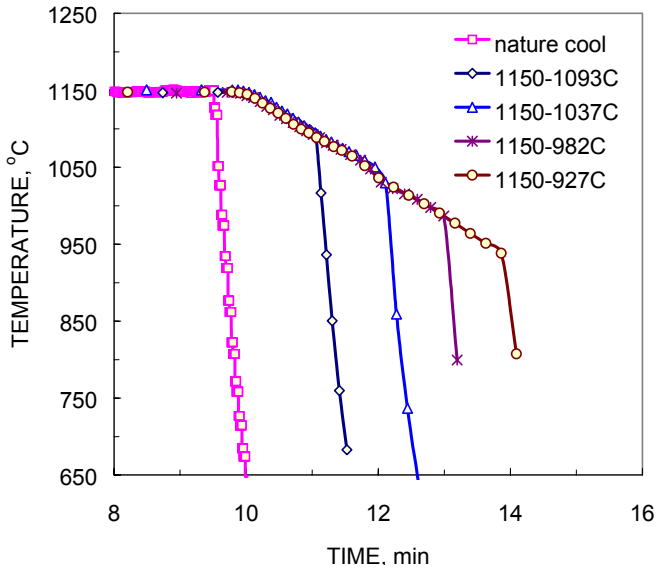

Figure 2.8 Recorded interrupt cooling profiles of Rene88DT

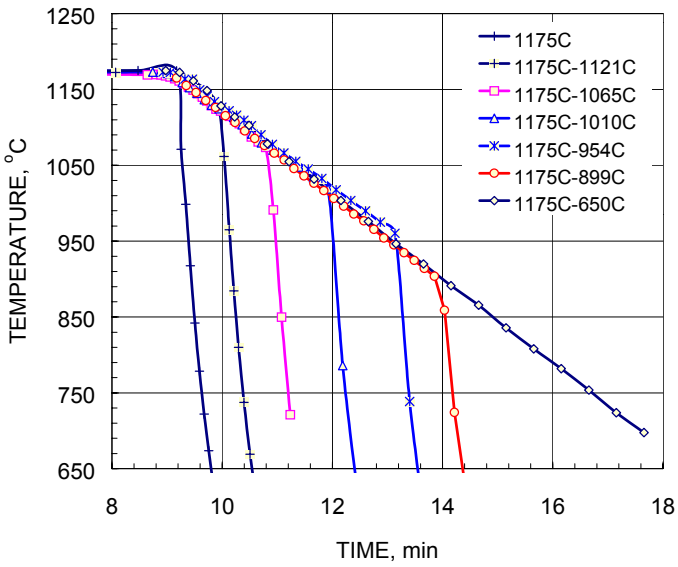

Figure 2.9 Recorded interrupt cooling profiles of U720LI

2.4 Isothermal aging

Isothermal aging was also carried out to study the coarsening kinetics of the γ′ precipitates during aging. The activation energy of coarsening could be calculated based on this study. Following results were expected to obtain:

- Precipitation as a function of holding time at fixed temperatures during aging
- Precipitation as a function of holding temperature at fixed times
- The activation energy

2.4.1 Experimental approach

The tests were performed in a modified 1600 DTA (Differential Thermal Analyze) furnace with an oil bath underneath the DTA chamber [37]. The experimental kit of the modified DTA furnace is demonstrated in Figure 2.10. A specimen was placed on the top of a support ceramic rod and heated to a designated temperature. After holding, the specimen was then pushed off the top of the ceramic rod and fell into the oil bath. As a result, the microstructure at high temperature was retained. Two monitoring thermocouples were located just below the specimen position and at the side of the ceramic rod. This differential arrangement of the two thermocouples made it possible not

only to keep track of the temperature of the specimen, but also to know the exact transition temperature and transition time.

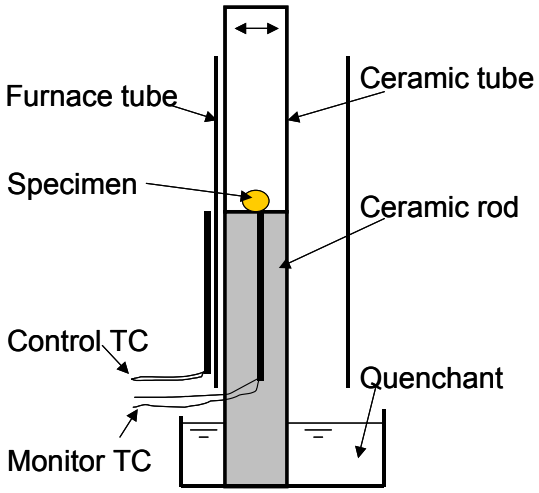

Figure 2.10 Quenching kit for isothermal aging test[37]]

2.4.2 Test procedure

All the specimens prior to the aging treatment were subjected a solution treatment at supersolvus temperature (1150°C for Rene88 and 1175°C for U720LI), and followed by water quench. After that, each specimen was aged under different condition of temperature and time, as listed in Table 2-IV, and Table 2-V for U720LI and Rene88DT, respectively. The sample size was about ϕ3×3mm.

Table 2-IV Isothrmal aging procedure for U720LI

Isothermal temp, °C \ Time, min	4	8	16	32
990	✔	✔	✔	✔
1010	✔	✔	✔	✔
1037	✔	✔	✔	✔
1065	✔	✔	✔	✔
1121	✔	✔	✔	✔

Table 2-V Isothrmal aging procedure for Rene88DT

Isothermal temp, °C \ Time, min	8	16	32	64	128
960		✔	✔	✔	✔
990		✔	✔	✔	✔
1020		✔	✔	✔	✔
1050	✔	✔	✔	✔	
1080	✔	✔	✔	✔	

2.5 Analytical approach

Metallographic sample from each cooling / aging test was cut from the center of the cut-off part from the quenched blank (see hatched region in Figure 2.1). The samples were manually ground to 800 grit on a Handimet2 roll grinder, electrolytically polished and electrolytically etched. After each step, the samples were rinsed in methanol and then blow-dried to avoid any stains. The γ' phase was easily highlighted in the etched samples. The key to sample preparation for the precipitate size measurement is to assure that only one layer of γ' precipitates on the surface is etched, and there is no overlapping of the particles. Sample preparation procedures were summarized in Table 2-VI.

Table 2-VI Sample preparation procedure

	Enchant solution	Voltage, v	Time, sec	phase
Electrolytic-polishing	80% Methanol + 20% HCL	25~30	15	
Electrolytic-etching	170mlH_3PO_4+16gCrO_3+10ml H_2SO_4	3~5	2~3	γ'

Cooling precipitate examination was conducted on a JEOL-6400 Scanning Electron Microscope (SEM). The operating voltage was 20KV and the current of the condenser lens was 0.06 nA. The magnification was between 10kx to 50kx.

Image processing and analysis were carried out using *ScionImage* and Microsoft Excel®. *ScionImage* is a public domain software from the National Institute of Health

(www.nih.gov), which is able to count every particle in the view domain and calculate the area of each particle. After that, the equivalent circle diameter for each particle was converted from the area (e.g. the diameter of a circle having the same area as the particle), and characterized as the precipitate size. In order to insure the accuracy of statistical analysis, the total number of particles counted in each specimen was between 200-1000. Statistical analysis were then performed using descriptive analysis and histogram analysis in Microsoft Excel® to obtain the mean diameter and size distribution of the γ' precipitates. Because of the resolution restriction of SEM, particles counted were those with the size larger than 0.04μm.

Particle density was defined as the number of the particles per unit area, which was calculated by:

$$\rho = \frac{\sum N_i + (\sum n_i)/2}{A}$$

Where $\sum N_i$ is the total number of the particles excluding the particles touching picture edge; $\sum n_i$ are the total number of the particles touching the picture edge. A is the total area examined.

2.6 Tensile test

Cooling rate is expected to significantly affect the cooling precipitation, and furthermore, the mechanical properties. In this research, tensile tests were conducted to study the effect of cooling rate on the tensile strength of both as-quenched and quenched + aged specimens. The tensile tests were performed at room temperature on an MTS machine with a computer control platform supported by Labview. The strain rate for the tensile tests was 0.0024mm/min.

Five different cooling rates (27°C/min, 55°C/min, 111°C/min, 167°C/min, and nature cooling) were chosen, which corresponded to the cooling rates in continuous cooling study. Single aging treatments (760°C for 8 hours, air cool for Rene88DT and 700°C for

24 hours, air cool for U720LI) were applied after supersolvus solution treatment to study the effect of aging treatment on tensile strength.

Tensile tests were also conducted on the specimens undergone the interrupted cooling. The interrupt cooling procedures are the same as that in the interrupt cooling study. The test design was aimed to study the strengthening mechanism during cooling.

2.7 Summary

1. Computer-controlled quench system equipped with an infrared high power quartz heater was proved to be sufficient to accomplish the research work. The control accuracy and flexibility of the system with a variety of cooling patterns is accomplished.
2. Two novel cooling approaches, continuous cooling and interrupt cooling, and isothermal aging were able to be carried out in the system and modified DTA furnace to study the γ' precipitation kinetics for both U720LI and Rene88DT alloys during continuous cooling and isothermal aging.
3. Tensile tests were performed in MTS machine to study the effect of the cooling rate, the interrupt temperature on the tensile strength on both as-quenched and quenched + aged conditions.
4. Precipitates examination, image processing, and statistic data analysis were carried out using scanning electronic microscope, *ScionImage* and Microsoft Excel® software.

Chapter 3: γ′ precipitation kinetics under continuous cooling

The systematic study of γ′ precipitation kinetics under controlled cooling condition in Rene88DT and U720LI alloys is the key to build the constitutive models for computational materials design and process optimization. This chapter begins with the calculation of the phase transformation to identify some critical thermodynamic parameters. Then the empirical relationship between the size of the cooling γ′ precipitates and cooling rate was then erected for both alloys. The comparison of the γ′ precipitation kinetics between both alloys was also carried out.

3.1 Phase transformation in the alloys

Before went on with the experimental study, we first explored the phase transformation in the alloys using a thermodynamic model. This CALPHAD (Calculation of Phase Diagram) method can usually provides us with valuable information about the transformation temperatures and equilibrium volumes of precipitates. The phase transformation simulation was performed using the popular commercial software Thermal-Calc, together with the all-element database for nickel base alloys. Figure 3.1 and 3.2 presented the phase diagrams at the state of equilibrium during cooling for Rene88DT and U720LI, respectively. In both alloys, the mole fraction of γ′ precipitates increased with the decrease of temperature, while the mole fraction of γ phase decreased.

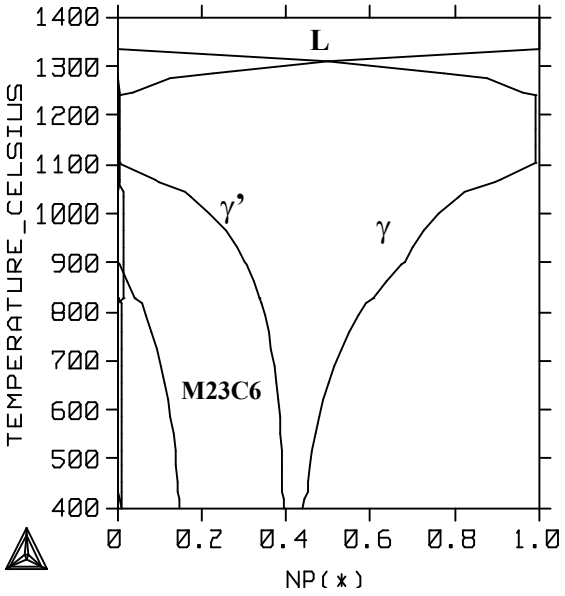

Figure 3.1 The mole fraction of γ' precipitates varied with temperature in Rene88DT

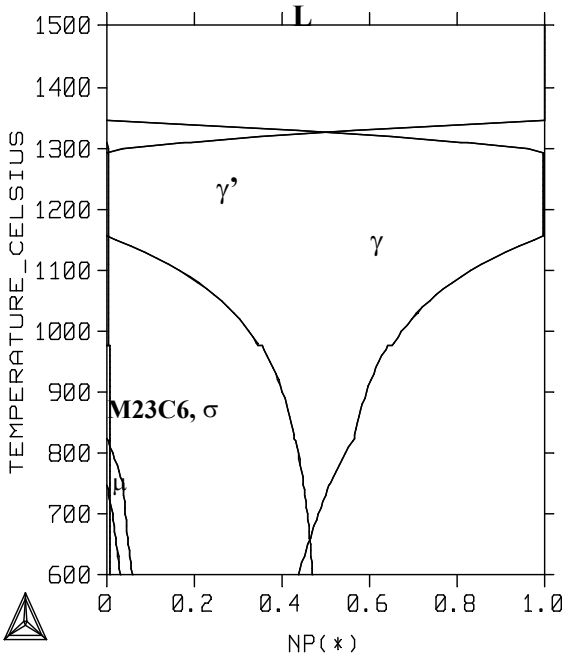

Figure 3.2 The mole fraction of γ' precipitates varied with temperature in U720LI

From the simulation, the key thermodynamic parameters were obtained and summarized in Table 3-I. The γ'solvus temperature of Rene88DT and U720LI are approximately

1103°C and 1153°C, respectively. The molar fraction of γ' precipitates at 760°C (aging temperature) is about 0.36 in Rene88DT and 0.44 at the 700°C (aging temperature) in U720LI.

Table 3-I The key thermodynamic parameters obtained from Thero-Calc simulation

Alloy	Liquidus, °C	Solidus, °C	γ' Solvus, °C	γ' molar fraction.
Rene88DT	1333	1240	1103	0.36 at 760°C
U720LI	1340	1290	1153	0.44 at 700°C

The DTA tests were also conducted to verify the Thermo-Calc simulation results. The heating and cooling rate used was 2°C/min. It was found that the γ' solvus temperatures measured from DTA test show good consistency with the results from the Thermo-Calc[38, 39].

3.2 γ′ precipitation versus cooling rate

3.2.1 Cooling γ′ precipitates morphology

Cooling γ′ precipitates were defined as the precipitates that were precipitated inside the grains during quenching after supersolvus solution treatment. The morphology of the cooling γ′ precipitates varies with the cooling rate in both Rene88DT and U720LI alloys is shown in Figure 3.3 and 3.4, respectively. As we see, the cooling γ′ precipitates were uniformly distributed in the matrix. With the decrease in cooling rate, the sizes of the homogenous distributed cooling γ′ precipitates increased, and their shapes changed from spherical to near cuboidal in Rene88DT. In U720LI, the shape of the cooling γ′ precipitates even changed to irregular ones. The γ′ precipitate size in Rene88DT is much smaller than that in U720LI in all cooling rate case. The average size of γ′ precipitates is around 0.05~0.15μm in Rene88DT and around 0.15~0.45μm in U720LI.

Besides, large blocky cooling precipitates and very fine precipitates were also found along grain boundaries at the lower cooling rate cases, as shown in Figure 3.5 and 3.6 in Rene88DT and U720LI, respectively.

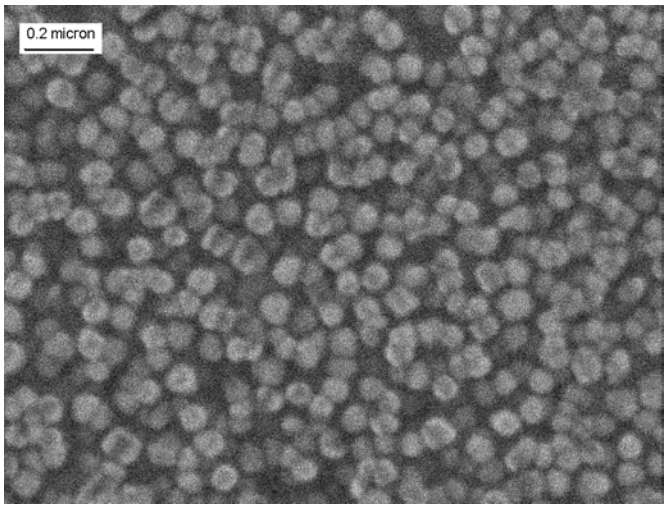

a) Solution: 1150°C, cooling rate: 174°C/min

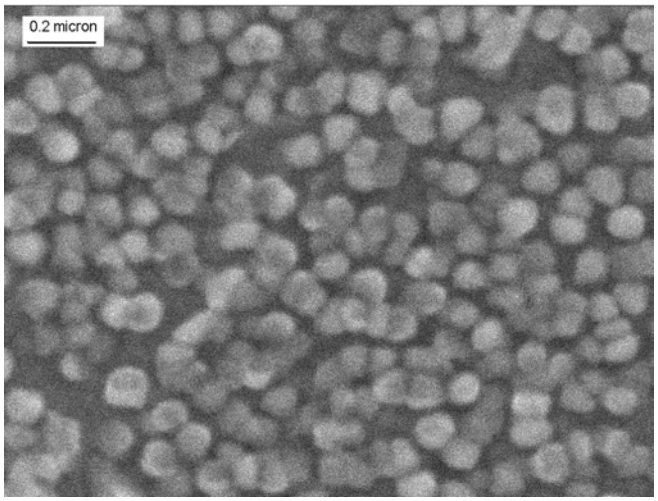

b) Solution: 1150°C, cooling rate: 111°C/min

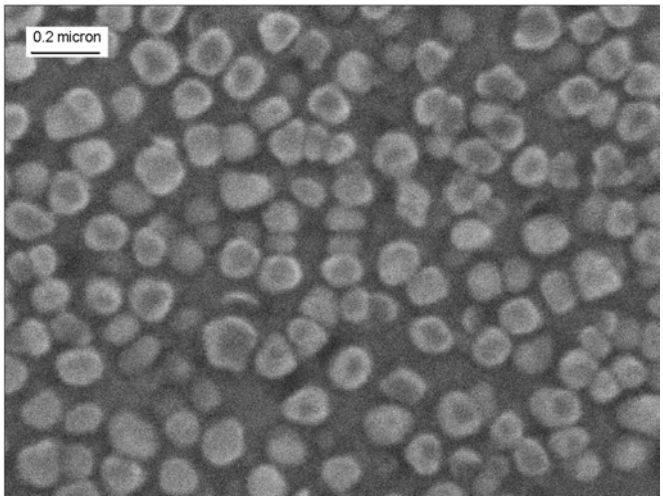

c) Solution: 1150°C, cooling rate: 55°C/min

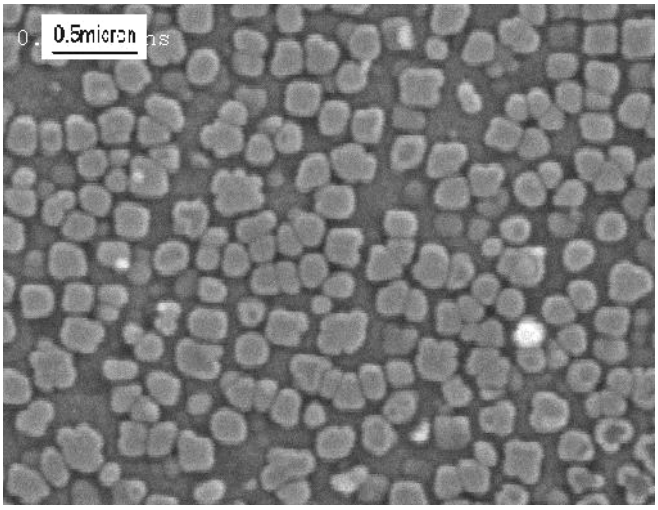

d) Solution: 1150°C, cooling rate: 27°C/min

Figure 3.3 The morphology of the cooling γ′ precipitates varies with cooling rates in Rene88DT

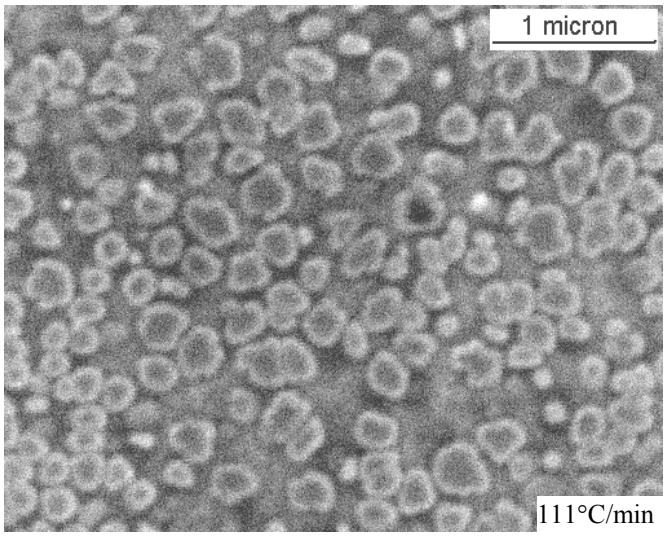

a) Solution: 1175°C, cooling rate: 111°C/min

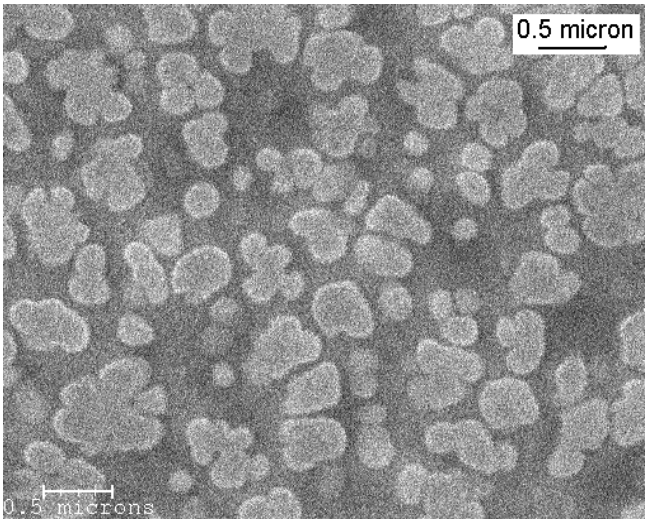

b) Solution: 1175°C, cooling rate: 11°C/min

Figure 3.4 The morphology of the cooling γ′ precipitates vs. cooling rate in U720LI

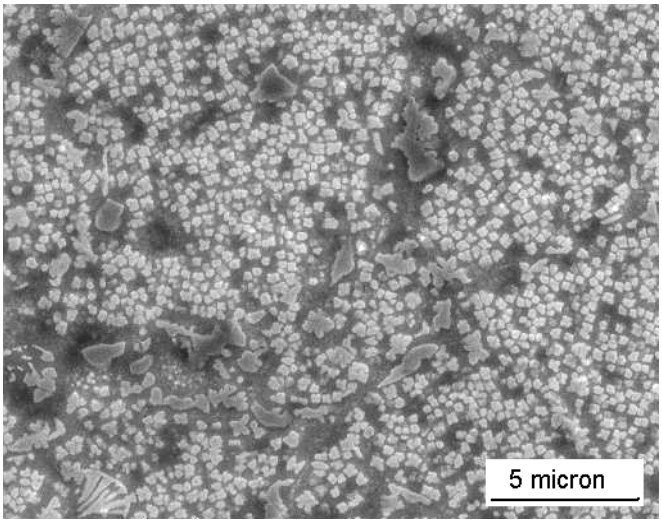

Solution: 1150°C, cooling rate: 11°C/min

Figure 3.5 γ ′ precipitates along grain boundaries in Rene88DT

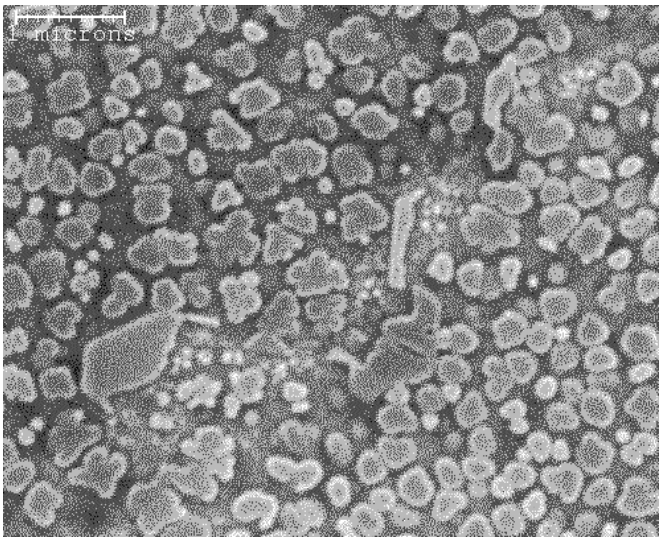

Solution: 1175°C, cooling rate: 55°C/min

Figure 3.6 γ′ precipitates along grain boundary in U720LI

3.2.2 Dependence of cooling γ′ precipitate size on the cooling rate

Cooling rate significantly affects the cooling γ′ precipitate size and their volume fraction. Empirical models were developed to characterize the relationship between the size of cooling γ′ precipitates and cooling rate for both alloys. The size of a cooling γ′ precipitate was characterized by the equivalent diameter in the statistical analysis as mentioned in Chapter 2. The statistical analysis was extensively carried out based on the measurement results of 200 ~ 1000 particles from each specimens. The statistical results were summarized in Table 3-II and 3-III in both Rene88DT and U720LI, respectively. It was noted that both the mean diameter of particles and standard deviation increased with the decrease in cooling rate. In Table 3-III, two categories of before-separation and after-separation were used. The indication of the categorizations will be explained later. The data under category of before-separation is the original measured data.

Table 3-II Cooling γ' precipitate size vs. cooling rates in Rene88DT

Specimen I.D.	cooling rate °C/min	Mean diameter μm	Standard deviation	Volume Fraction
R804	174.4	0.055	0.014	0.273
R805	110.6	0.074	0.018	0.287
R806	56.5	0.092	0.022	0.362
R807	27.4	0.138	0.035	0.34

Table 3-III Cooling γ′ precipitate size vs. cooling rates in U720LI

Specimen	cooling rate	Before-separation		After-separation		Volume
I.D.	°C/min	Mean diameter, μm	Standard deviation	Mean diameter, μm	Standard deviation	Fraction %
U702a	171.6	0.166	0.041	0.166	0.041	33.3
U703b	110.2	0.196	0.060	0.196	0.060	37.5
U704c	56.5	0.256	0.075	0.256	0.075	42.5
U706d	27.6	0.216	0.093	0.319	0.051	45.8
U721g	11.0	0.314	0.134	0.440	0.080	44.1

By plotting the mean diameter of the cooling γ′ precipitates versus cooling rate, the function of the size on the cooling rate were obtained. Figure 3.7 shows the cooling γ′ precipitates size as a function of cooling rate in Rene88DT. The precipitate size decreases with the increase in cooling rate. By the least-square data fitting, it was found that the relation between the cooling γ′ precipitate size and cooling rate obeys a power law, with an exponential being 0.47, which is given as:

$$\text{Log}D_{\gamma'} = -0.2029-0.4655*\text{Log}(dT/dt), \text{ or } :D_{\gamma'} = 0.6267\ (dT/dt)^{-0.4655} \qquad R^2 = 0.99 \qquad 3\text{-}1$$

where the precipitate diameter $D_{\gamma'}$ is in micron, and the cooling rate dT/dt in °C/min.

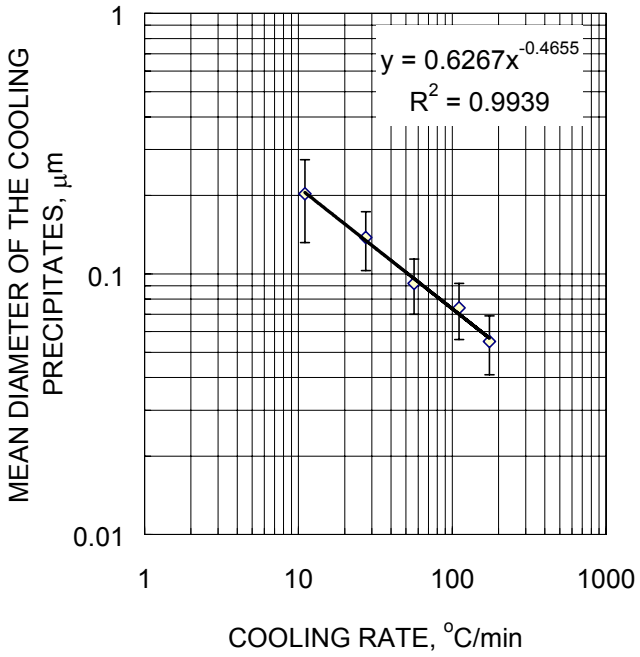

Figure 3.7 Plot of cooling precipitate size against cooling rate in Rene88DT

The cooling γ′ precipitates in Rene88DT alloy have a diameter around 0.04-0.2 μm at the cooling rate range studied. The volume fraction and particle density in Rene88DT were plotted against the cooling rate in Figure 3.8. The γ′ particle density increases with the cooling rate while the volume fraction of cooling γ′ precipitates decreases with the increase in cooling rate. This is because higher cooling rate results in more supersaturation buildup in the γ-matrix, which decreases the critical nuclei size according to the classic nucleation theory. Therefore, more γ′ precipitates are nucleated. In addition, fast cooling suppressed the growth of the cooling γ′ precipitates. Therefore, lower γ' volume fraction is observed.

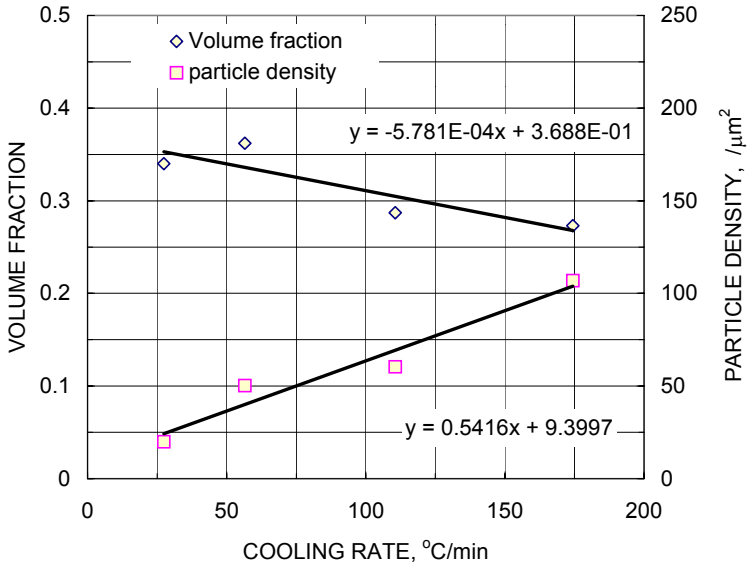

Figure 3.8 The volume fraction and the particle density of the cooling γ′ precipitates varies with cooling rate in Rene88DT

The regression function of the volume fraction and the particle density of the cooling γ′ precipitates are given as:

$$\text{Volume fraction of } \gamma' = -5.781E\text{-}04*(dT/dt) + 0.3688 \qquad 3\text{-}2$$

$$\text{Particle density} = 0.5416*(dT/dt) + 9.3997 \qquad 3\text{-}3$$

In contrast with Rene88DT, the mean diameter of the particles versus cooling rate in U720LI did not show apparent power law relationship, as seen in Figure 3.9. It was found that the mean diameter of the cooling γ′ precipitates increased with the decrease in the cooling rate. However, when the cooling rate is dropped to below 27°C/min, the mean diameter of the cooling γ′ precipitates decreased dramatically and shifted away from the trend line. The mean diameter increased again when the cooling rate decreased to 11°C/min. This phenomenon is different from the result obtained in Rene88DT and brought a puzzle and doubt about the measurement results. After repeating the measurement, the same phenomenon shows up again. In order to explain this, a histogram analysis of the particle size was carried out.

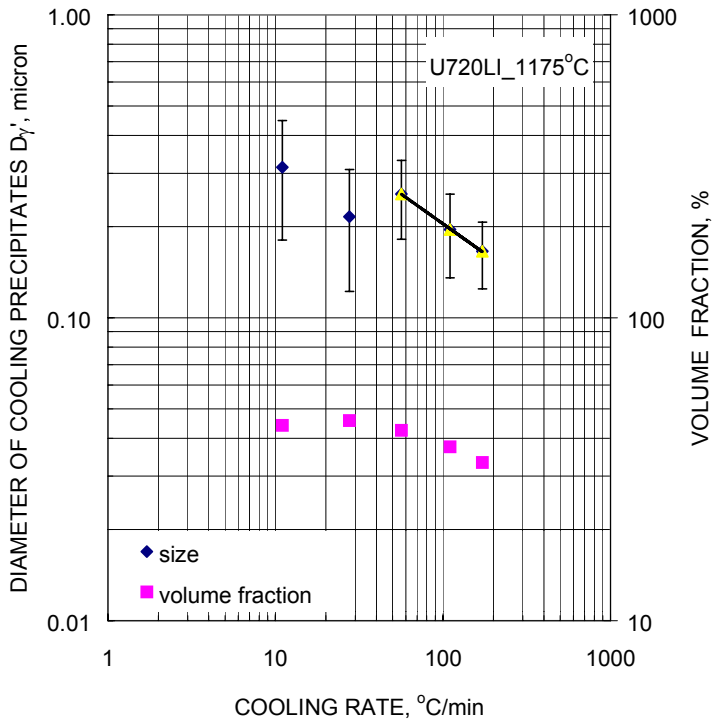

Figure 3.9 Plot of the cooling γ' precipitate size and volume fraction against cooling rate

3.2.3 Size distribution of the cooling γ′ precipitates

To study the size distribution of the cooling γ′ precipitates, histogram analyses corresponding to different cooling rates were carried out and results were shown in Figure 3.10 and Figure 3.11 for Rene88DT and U720LI, respectively. In the legends of charts, 'Frequency' is defined as the percentage of particles with diameters within an interval range and 'Cumulative %' means the percentage of particles with a diameter smaller than a particular value. It was noted that the size corresponding to the peak frequency moved toward a larger value with the decrease of the cooling rate in both charts, which means that the average size increases with the decrease of cooling rate. A normal distribution of the precipitate size with a single peak was observed in all cooling rate cases in Rene88DT.

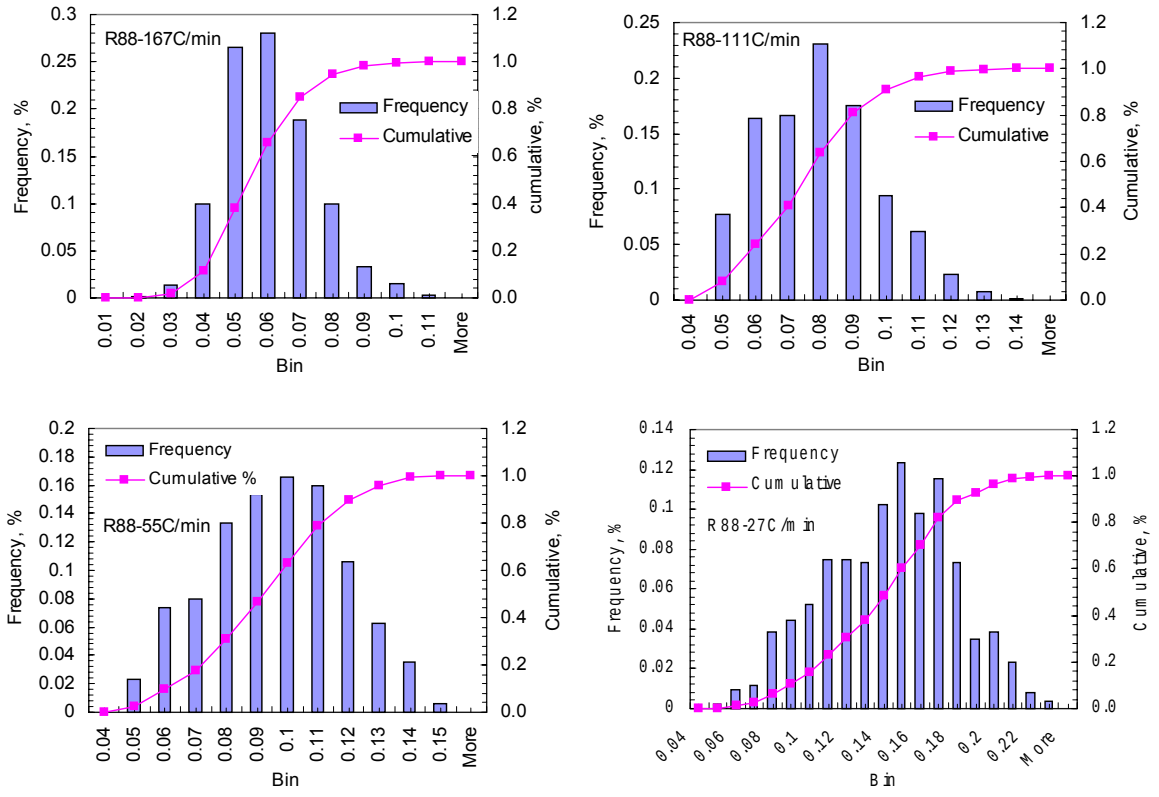

Figure 3.10 Histogram charts of the cooling γ′ precipitates versus cooling rates in Rene88DT

However, in U720LI, the binomial distribution was discovered at the cooling rate lower than 55°C/min. It was shown in Figure 3.11 that a normal size distribution with a single peak was observed in higher cooling rate cases and peak size corresponding to the highest frequency moves toward a larger value with the decrease in cooling rate. As cooling rate lower than 55°C/min, binomial distribution was shown obviously. The bi-model distributions is believed to be due to a second round of γ′ precipitate nucleation during quenching, here onward referred to as secondary burst cooling γ′ precipitates. The secondary burst cooling γ′ precipitates are much smaller than the primary ones. This binomial distribution brought down the average size of the cooling γ′ precipitates.

The bi-model distribution provides great experimental support for the multi-burst hypothesis and will lead further study on nucleation theory and strengthening theory in the continuous cooling condition.

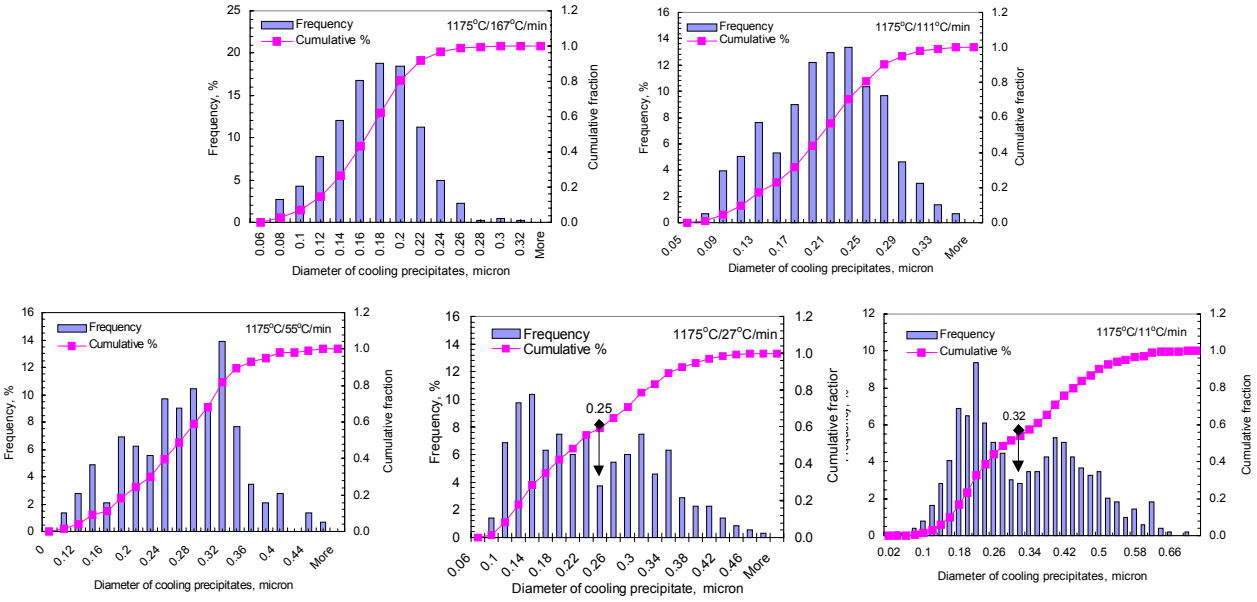

Figure 3.11 Size distribution of cooling precipitates in U720LI

In order to give an experimental correlation between the cooling γ′ precipitate size and cooling rate, the effect of the smaller sized secondary burst cooling γ′ precipitates on the average size was excluded when calculated the average γ′ size. This was done by identifying the crossover point in the bimodal distributions at low cooling rates, and re-calculating the average size of just the first burst γ′ precipitates with only those precipitates size larger than the cross-point value as seen in Fig.3.11. For instance, the first burst cooling γ′ precipitates are those with the size larger than 0.25μm at the cooling rate of 27°C/min and 0.32μm at the cooling rate of 11°C/min. After the recalculation and plotting in Figure 3.12, it was found that the relationship between the size of first burst cooling precipitates and cooling rate also follows a normal power law well, and with an exponent of about 0.35. The empirical equation was given as:

$$\text{Log } D_{\gamma'} = 0.0165 - 0.354 * \text{Log } (dT/dt) \quad R^2 = 0.998 \qquad 3\text{-}4$$

where the precipitate diameter $D_{\gamma'}$ is in micron, and the constant cooling rate dT/dt in °C/min.

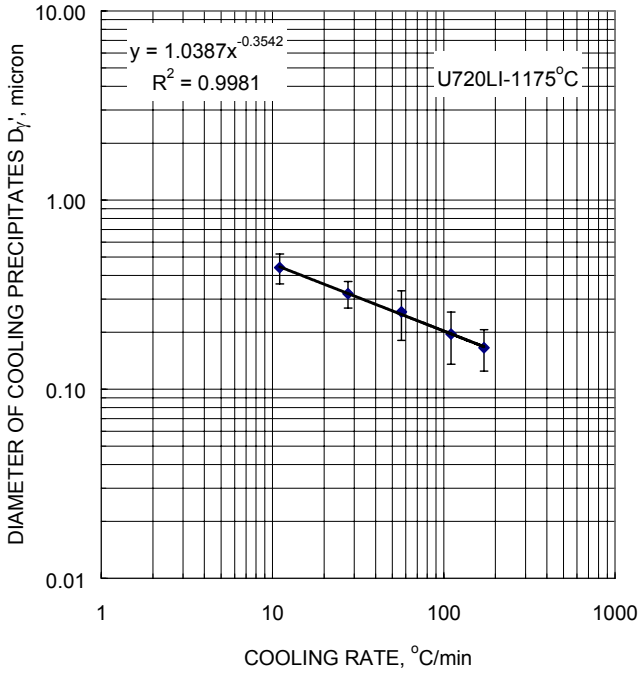

Figure 3.12 Modified the cooling γ′ precipitates size vs. cooling rate (leaving out the secondary burst γ')

All these precipitates were examined under SEM and the accountable size was restricted by the resolution of SEM, e.g. all these are larger than 0.04μm. Transmission electric microscope (TEM) examination should be carried out for further fine scale investigation.

3.2.4 Cooling γ′ precipitation under special cooling profiles

γ′ Precipitation corresponding to the simulated cooling profiles

To simulate the real cooling path from thermal process simulation in the model disk, the specimen was quenched at the input cooling profile as described before. The corresponding morphology of the cooling γ′ precipitates was shown in Figure 3.13.

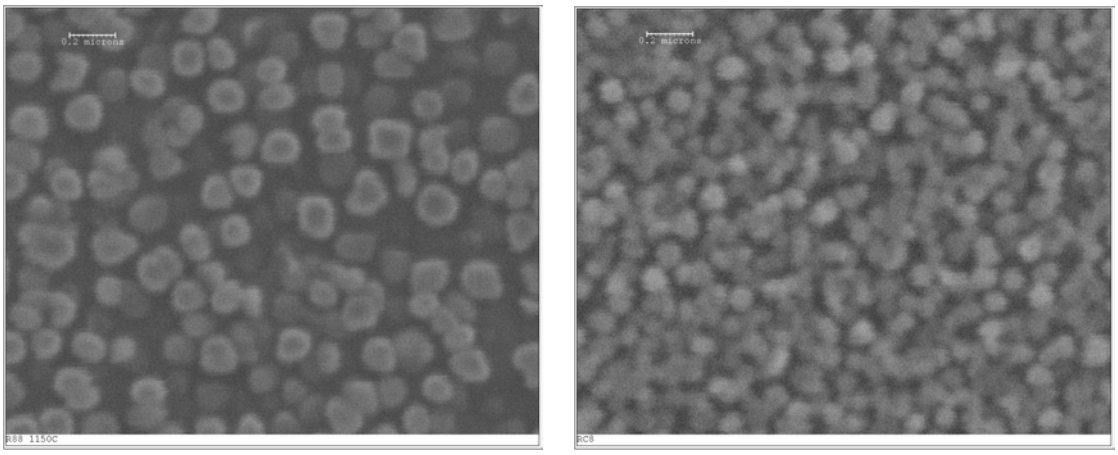

a) Slow cooling, profile B b) Fast cooling, profile A

Figure 3.13 Morphology of cooling γ′ precipitates corresponding to real cooling profiles

Cooling under a designated multi-step profile

After multi-step quenching, the morphology of the cooling γ′ precipitates was shown in Figure 3.14. It was seen that the particle size is larger than that from direct continuous cooling.

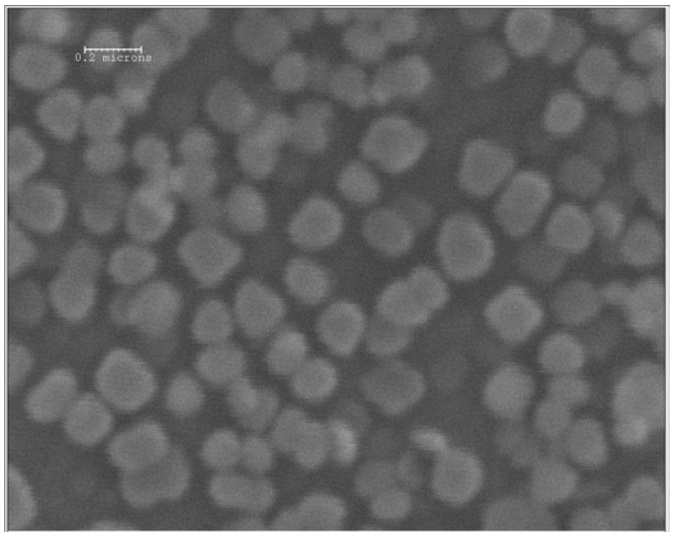

Figure 3.14 The morphology of γ′ precipitates from multi-step cooling in Rene88DT 1150°C to 900°C at 56°C/min + hold 1 minute + quenched to 650°C at 56°C/min

3.3 Discussion

There are three stages of the cooling γ′ precipitate formation during an entire cooling process: nucleation, growth and coarsening of the cooling γ′ precipitates. Even though γ′ nucleation actually might be suppressed at very high cooling rates[40], but it is practically impossible. According the classic nucleation theory, stable critical nucleus size is given by [18]:

$$R^* = \frac{2\sigma V_m}{\Delta G_p}$$

where Δf_δ - strain energy per unit volume

σ - interfacial energy per unit area

V_m – the molar volume of the precipitates

ΔG_p the molar free energy of precipitate formation, which can be expressed as:

$$\Delta G_p = \Delta f_v - \Delta f_{\delta,}$$

where Δf_v - chemical free energy, driving force of nucleation

Δf_δ - *interface energy*

Nucleation of γ' phase depends on two major factors; one is the chemical free energy provided by the supersaturation in the matrix, the other is the interface energy including surface energy and elastic strain energy generated by the lattice mismatch between γ and γ′ phases. Therefore, supersaturation and lattice mismatch are two competing parameters that controls γ' nucleation. Higher supersaturation results in the larger molar free energy for the formation of the cooling γ′ precipitates, and therefore, the critical nucleus size of cooling γ′ precipitates is smaller. Also, smaller the lattice mismatch between γ and γ′ phase, the lower the interface strain energy, and smaller the critical nuclei size is required.

In aging or isothermal precipitation cases, initial supersaturation in the matrix is obtained by rapidly quenching after solution treatment. Therefore, during the aging, the supersaturation only decreases as the γ' precipitates form and grow. However, in continuos cooling condition, the change of supersaturation is a complex process, which includes the supersaturation generation due to the continuous cooling and supersaturation

consumption due to γ' nucleation and growth. The nucleation and grow of γ' precipitates depends on the competition of these two processes.

Figure 3.15 schematically shows the effect of cooling rate on γ' formation during quenching. The higher cooling rate results in more undercooling, and then more supersatuation building-up. Therefore, a large amount of γ′ precipitates with small nuclei size is nucleated with small inter-particle spacing. On the other hand, fast cooling may suppress the diffusion-controlled γ' growth, even though the small inter-particle spacing requires short-distance diffusion. That is why the fast cooling rate results in the formation of the larger amount of smaller cooling γ′ precipitates with smaller inter-particle spacing.

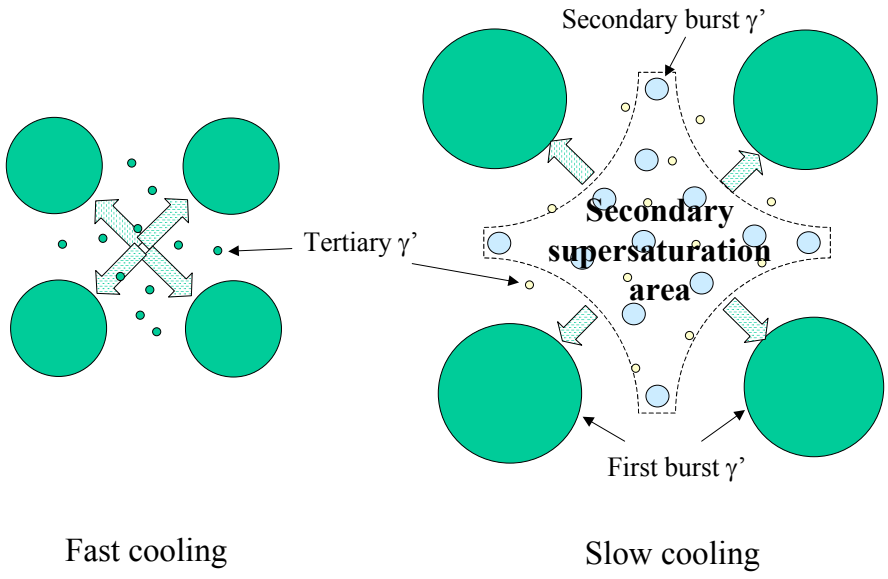

Figure 3.15 γ' formation scheme under different cooling rates

When cooling rate is slower, the undercooling is less, and hence the matrix is less supersaturated. Small ΔG_p results in larger critical nucleus size. The first burst cooling γ′ precipitates is therefore bigger and the inter-particle spacing is larger. Although the lower cooling rate allows diffusion to proceed and hence produces larger γ′ particles, the long distance diffusion is somehow restricted due to the continuous cooling. Therefore, with the temperature decreases continuously, there is a chance for secondary supersaturation to be built up again around the local area between the first burst γ′ precipitates. As the

secondary supersaturation becomes big enough and the accumulated chemical energy in γ-matrix became big enough to overcome the energy barrier for a new round of nucleation, the secondary burst of γ′ precipitates becomes possible. This accounts for the double-peak distribution of γ′ observed at the slower cooling case (cooling rate <27°C/min) as seen in continuous cooling in U720LI. Since at that time, the temperature is too low to allow intensive solute diffusion, the growth of the secondary burst precipitates is restricted. Consequently, the secondary burst precipitates are much smaller than the first burst particles. Also, because of the variation of composition in γ and γ′ with temperature during formation, it is expected that the secondary burst γ' has different lattice mismatch from the first burst ones [27]. The multi-nucleation was also found in the precipitation simulation in a P/M superalloy CH98. [13].

It is possible to see the secondary burst cooling γ′ precipitates for higher cooling rates or the tertiary burst cooling γ′ precipitates for lower cooling rates only at high magnification examination such as using transmission electron microscope (TEM).

No bi-model distribution was observed in Rene88DT at the current SEM examination condition. One of the reasons is believed to be related to the smaller mismatch in Rene88DT. The smaller mismatch means smaller elastic strain energy induced during nucleation and smaller interface energy. Therefore the critical nucleus size is smaller and growth rate of particle is higher, then the secondary supersaturation is more difficult to build up due to the larger amount of particle forming with a small inter-particle spacing in comparison to the U720LI. However, it does not mean that there is no multi-stage nucleation of γ′ precipitates in Rene88DT. Further TEM examination should be carried out.

3.4 Summary

This work covered the researches on cooling precipitation kinetics in P/M superalloys U720LI and Rene88DT under continuous cooling. The empirical models were established to describe the relationship between cooling precipitates size and cooling rate in both alloys.

1. Of the most significance is the multiple nucleation and resultant binomial distribution of the cooling γ' precipitates formed at lower cooling rate cases in U720LI. No observation of bi-model distribution of the cooling γ' precipitates is in Rene88DT. However double precipitation cannot be excluded because of the limitation of the experimental method used.

2. The size of the cooling γ' precipitates was found to increases with the decrease of the cooling rate and the relationship follows a power law with an exponential being about 0.47 for Rene88DT and 0.35 for U720LI.

3. At the cooling rate range of 11°C/min ~167°C/min, the mean diameter of the cooling γ' precipitates are around 0.04μm ~ 0.2μm in Rene88DT and 0.15μm ~ 0.45 μm in U720LI. The mean diameter of the cooling γ' precipitates in Rene88DT is much smaller than that in U720LI at all cooling rates cases.

Chapter 4: γ′ Precipitation kinetics in interrupt cooling

The γ′ precipitation during continuous cooling had been studied to understand the size of the cooling γ′ precipitates as a function of cooling rate in the previous chapter. The objective of the interrupt cooling study is to understand the step-by-step development of the cooling γ' precipitates during a quenching process, which will provide a growing picture of the cooling γ′ precipitates. This work can only be done with the reliable control of the quench system.

This chapter began with the investigation of the morphology change of the cooling γ′ precipitates during entire cooling process. Then the size of the cooling γ′ precipitates varied with the decreasing temperature was studied. Finally, an empirical model of the size of the cooling γ′ precipitates as a function of decreasing temperature in both U720LI and Rene88DT alloys were developed.

4.1 Cooling γ' precipitates morphology

As described in chapter 2, the interrupt cooling was accomplished by heating up the specimen to a solution temperature, holding for 5 minutes, and then quenching it at the cooling rate of 55°C/min to different intermediate temperatures, i.e. interrupt temperatures. Figure 4.1 and 4.2 shows the morphology of the cooling γ′ precipitate corresponding to each interrupt temperature in both Rene88DT and U720LI, respectively. As we can see, the cooling γ′ precipitates grow dramatically as the temperature decreases. At the same time, the volume fraction of the γ′ precipitates increases.

In Rene88DT, the first interrupt temperature is 1093°C. γ′ precipitates were invisible at that temperature. At the temperature of 1037°C, homogeneously distributed small and spherical cooling γ′ precipitates were observed. After that, the cooling γ′ precipitates grow rapidly and remain almost spherical shape with the decrease of the interrupt temperatures, which implies that the growth of the cooling γ′ precipitates dominates the quenching process and no coalescence take place.

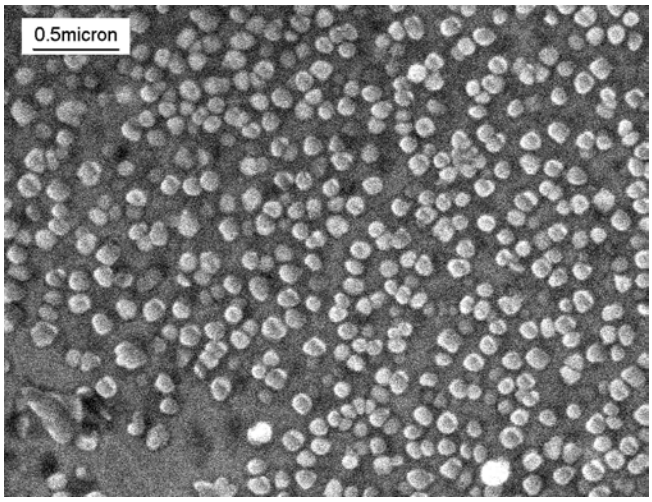

a) Rene88DT: Solution: 1150°C, Interrupt:1037°C

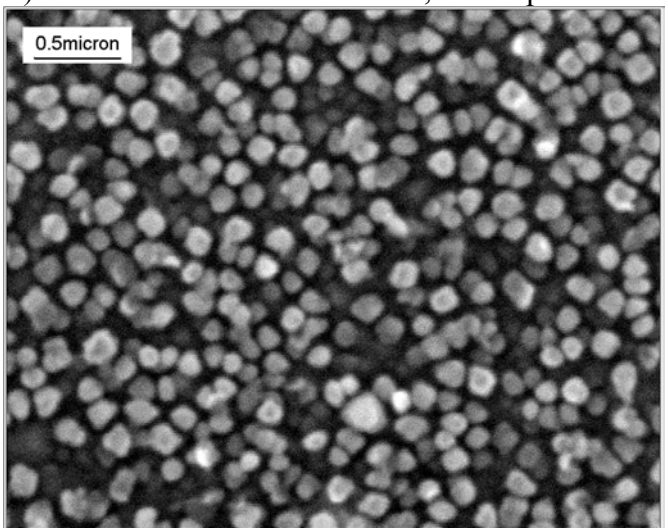

b) Rene88DT: Solution: 1150°C, Interrupt:983°C

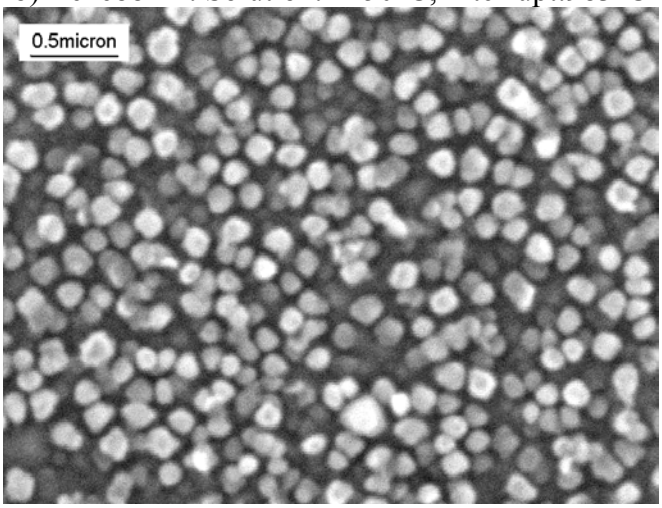

c) Rene88DT: Solution: 1150°C, Interrupt: 926° C

Figure 4.1 Cooling γ′ precipitates in different temperature steps in Rene88DT

In U720LI, the initially formed cooling γ′ precipitates are mostly between spherical and cuboidal shapes with an average size of about 0.16 micron at 1121°C, which is much bigger than that observed in Rene88DT. The cooling γ′ precipitates grow continuously and the shape of the γ′ particles changes gradually from spherical to cuboidal. When the temperature is dropped to about 900°C, irregular shaped cooling γ′ precipitates shows up. The irregular morphological change in U720LI is believed to be associated with the coarsening or coalesce of the γ′ precipitates in the late stage of the coarsening.

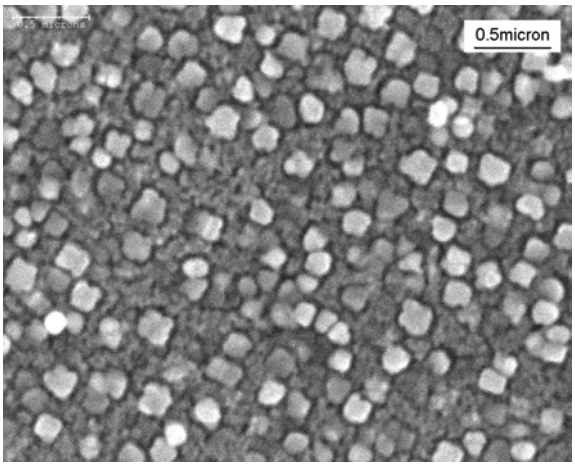

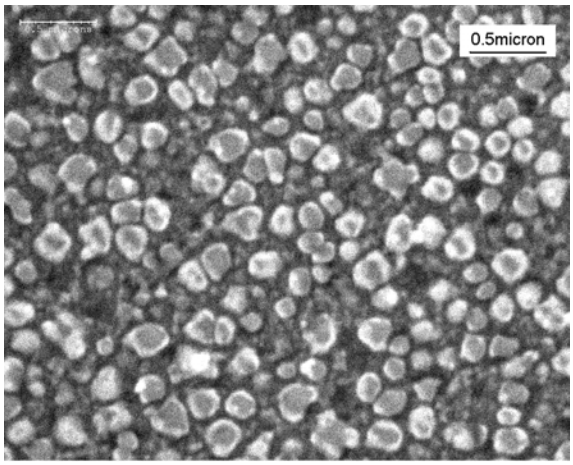

a)U720LI: Solution:1175°C, Interrupt:1121°C b) U720LI: Solution: 1175°C, Interrupt: 1065°C

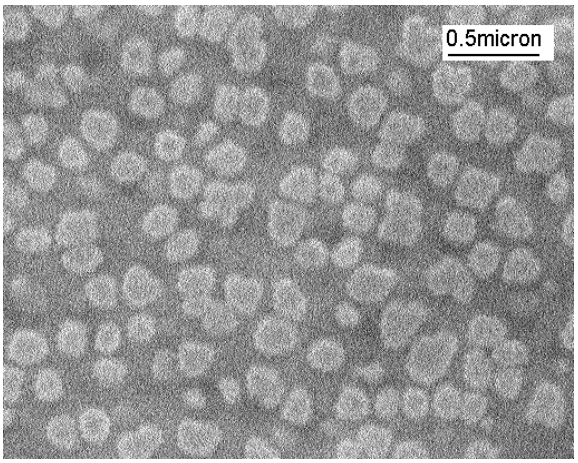

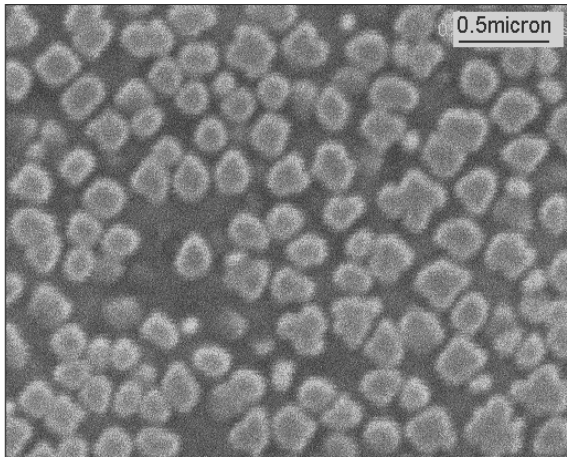

c) U720LI: Solution: 1175°C, Interrupt: 1010°C d) U720LI: Solution: 1175°C, Interrupt: 954°C

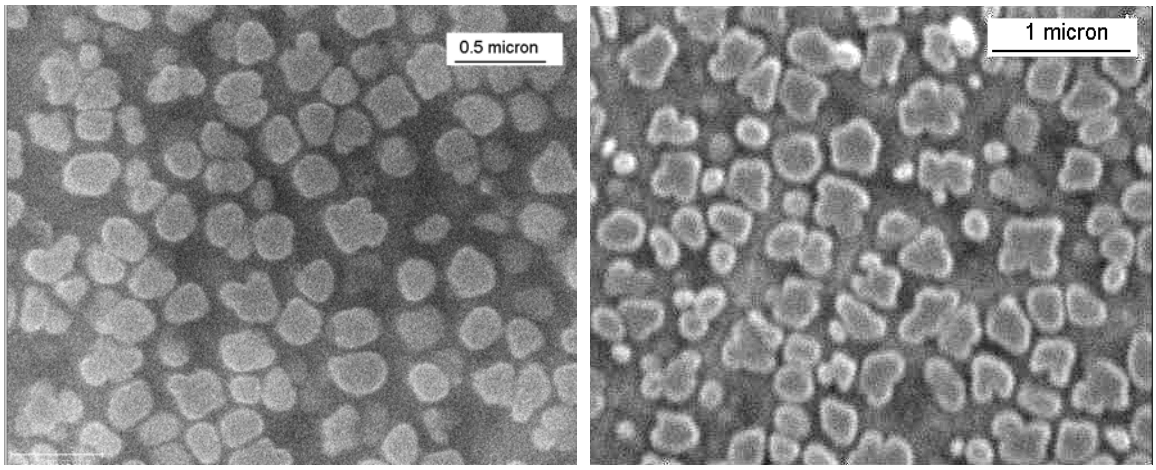

e) U720LI: Solution: 1175°C, Interrupt: 899°C f) U720LI: Solution: 1175°C, Interrupt: 650°C

Figure 4.2 Cooling γ′ precipitates in different temperature steps in U720LI

4.2 γ′ Growth kinetics as a function of interrupt temperature

4.2.1 γ′ precipitate size

To study the growth kinetics of the cooling γ′ precipitates during cooling, the relationship between the γ′ precipitate size and the decreasing temperature was carried out and results was plotted in Figure 4.3 and 4.4 for both Rene88DT and U720LI, respectively. In general, with the decrease of the interrupt temperature, the mean diameter of the cooling γ′ precipitates increased continuously with the decrease of the temperature.

In Rene88DT (Figure 4.3), the cooling γ′ precipitates size corresponding to the interrupt temperatures 1150°C and 1093°C was not included because the γ′ precipitates were too small to be counted. The growth of the γ′ precipitates as a function of the interrupt temperature was best fitted to a linear relation (given below).

$$\text{Rene88DT:} \quad D_{\gamma'} = -3.24\times10^{-4}T + 0.421, \quad R^2=0.98 \qquad 4\text{-}1$$

where the mean diameter of the cooling γ′ precipitates $D_{\gamma'}$ is in micron, and the interrupt temperature is in °C.

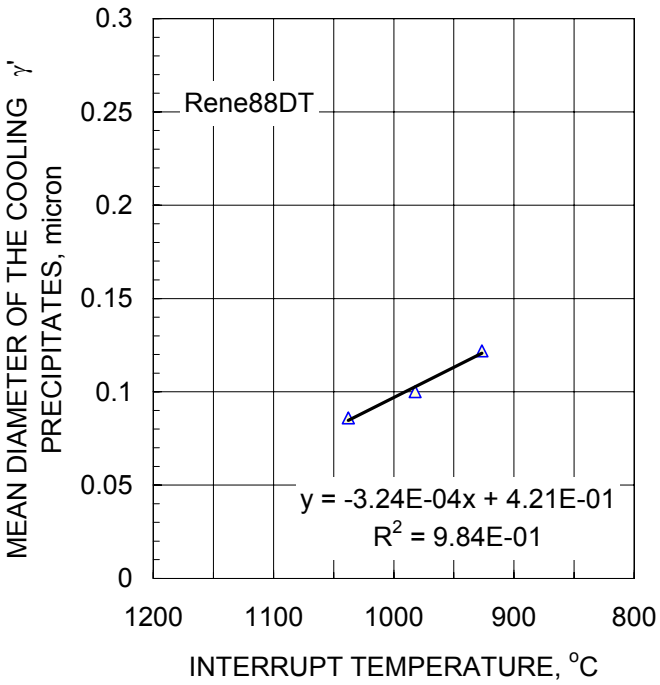

Figure 4.3 The cooling γ′ precipitates size against the interrupt temperature in Rene88DT

In U720LI, at the beginning of the quenching, when the supersaturation in the matrix is sufficiently, γ′ starts to nucleate. At a certain temperature range, the γ′ keeps its burst. As a result, the average size of these first burst γ′ precipitates remained almost stable. As temperature is decreased to below 1065°C, growth of the cooling γ′ precipitates dominates the rest of cooling process. Therefore, the average cooling γ′ precipitates size starts to increase rapidly, as shown in Figure 4.4. The growth kinetics of the cooling γ′ precipitates was expressed as a linear function of temperature through the best fitting:

U720LI: $D_{\gamma'} = -2.24\times10^{-4}T + 0.397, \quad R^2=0.96.$ 4-2

Where the mean diameter of the cooling γ′ precipitates $D_{\gamma'}$ is in micron and the interrupt temperature is in °C.

No detectable secondary burst of the cooling γ′ precipitates at the cooling rate of 55°C/min was observed under the current SEM examination, which was consistent with the result obtained from continuous cooling.

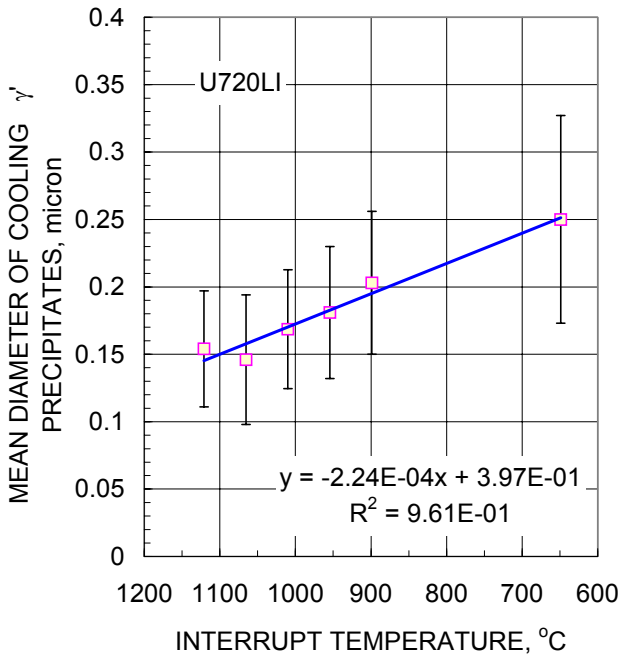

Figure 4.4 Mean diameter of the cooling γ′ precipitates against the interrupt temperatures in U720LI

In comparison with the growth kinetics of precipitates in Rene88DT, the growth rate of the cooling γ′ precipitates in U720LI is lower, but the mean diameter of the cooling γ′ precipitates is larger than that in Rene88DT.

4.2.2 Volume fraction of the cooling γ′ precipitates

The effect of cooling rate on both the volume fraction and the particle density of the cooling γ′ precipitate in Rene88DT is shown in Figure 4.5. Both the volume fraction and the particle density of the cooling γ′ precipitates show their initial increase and then decrease as the cooling temperature is decreased.

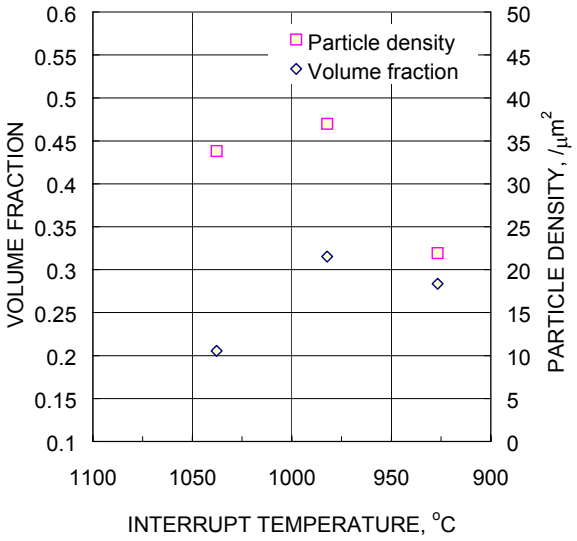

Figure 4.5 Variations of volume fraction and particle density of of the cooling γ′ precipitates with interrupt temperatures in Rene88DT

The variation of the particle density and the volume fraction of the cooling γ′ precipitates with the interrupt temperatures in U720LI were also measured and plotted in Figure 4.5. There are two bumps in both particle density curve and the volume fraction curve. It is believed to be due to the multi-stage nucleation during γ′ precipitates bursts, as explained earlier, but further confirmation is needed. The significant increase of the volume fraction actually occurs at a temperature below 1010°C.

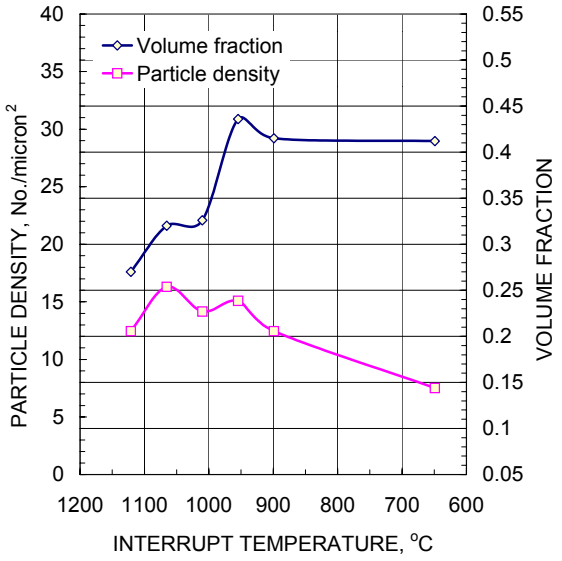

Figure 4.6 The plot of the volume fraction and the particle density of the cooling γ′ precipitates vs. interrupt temperature in U720LI

4.2.3 Histogram analysis of the cooling γ' precipitate

Histogram analysis was also carried out to study the size distribution of the cooling γ′ precipitates. The histogram charts of cooling γ′ precipitates in Rene88DT are shown in Figure 4.7. A normal size distribution with single peak of the cooling γ′ precipitates was noticed in both alloys. The size corresponding to the maximum frequency moved toward a larger value as the interrupt temperature decreases, which is similar to what we saw in continuous cooling study. However, no double-peak distribution in the precipitate size was found at any of the temperature steps in both alloys, which is different from what were observed in U720LI after continuous cooling study at lower cooling rate [7].

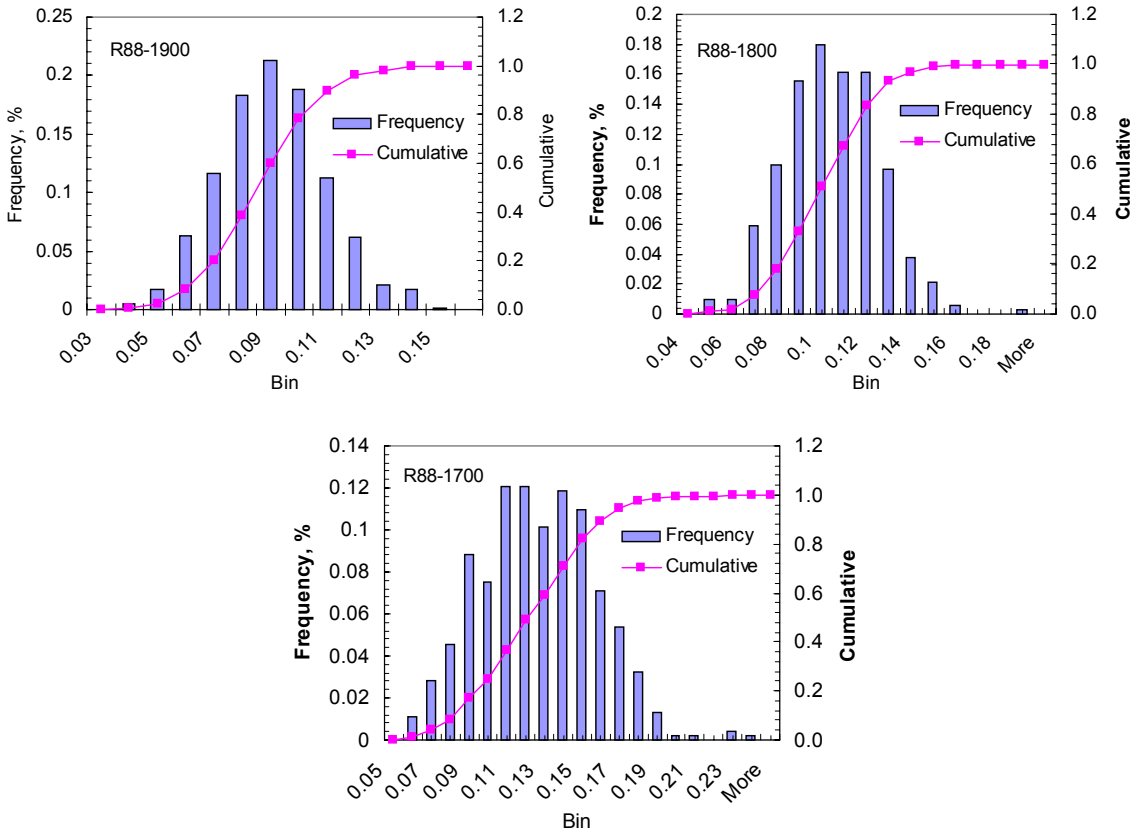

Figure 4.7 Histogram chart of cooling γ′ precipitates vs. interrupt temperature in Rene88DT

4.3 Discussion

Interrupt cooling enables the step-by-step study of the cooling γ′ precipitation. The results from the interrupt quenching suggest that at the beginning of the quench, nucleation plays a key role over a temperature range because of the undercooling. After nucleation, the growth of γ′ dominates the cooling process until the secondary burst of the cooling γ′ precipitates happens. Therefore, the starting cooling rate in quench process is of much significance in the control of γ′ precipitates size and the determination of the material strength.

In U720LI, from Figure 4.4, the relatively stabled average precipitate size at the early stage of the quenching is believed to be related to the continuous formation of the γ′ precipitates, which are considered to be the first burst cooling γ′ precipitates. Under practical circumstances, the γ′ burst temperature is lower than γ′ solvus temperature, e.g. the nucleation of the γ′ precipitates requires certain undercooling, which is also indicated by Dr. David Ferrer [27]. The temperature corresponding to the initial γ′ precipitation temperature is defined as the onset precipitation temperature T_{onset}. Another temperature corresponding to maximum γ′ precipitation rate is defined as the maximum precipitation temperature T_{max}. Figure 4.8 shows the variation of the T_{onset} and T_{max} with cooling rate obtained from DTA tests. With the increase in the cooling rate, T_{onset} stays almost the same. However, T_{max} decreases with the increase of cooling rate. Here, the undercooling is defined as the difference between the γ′ solvus temperature and the T_{max}. Therefore, the higher the cooling rate, the larger the undercooling is needed, the lower T_{max}. In addition, the temperatures range for precipitation (named precipitation range, from T_{onset} to T_{max}) becomes wider, which means that the γ′ precipitation actually spans over a wide temperature range. Observing the unchanged T_{onset} can eliminate the effect of thermal inertia of the thermocouple on the shift of the T_{max}. It is interesting to note that both the T_{max} and the magnitude of the γ′ precipitation range vary linearly with the cooling rate, as shown in Figure 4.9. A regression analysis gives:

$$T_{max} = -0.433 \times (dT/dt) + 1120.4 \qquad \text{with} \quad R^2 = 0.99 \qquad 4\text{-}3$$

$$\Delta T = T_{max} - T_{onset} = 0.433 \times (dT/dt) + 2.626 \quad \text{with} \quad R^2 = 0.99 \qquad 4\text{-}4$$

where the cooling rate is in °C/min, and the temperature in °C.

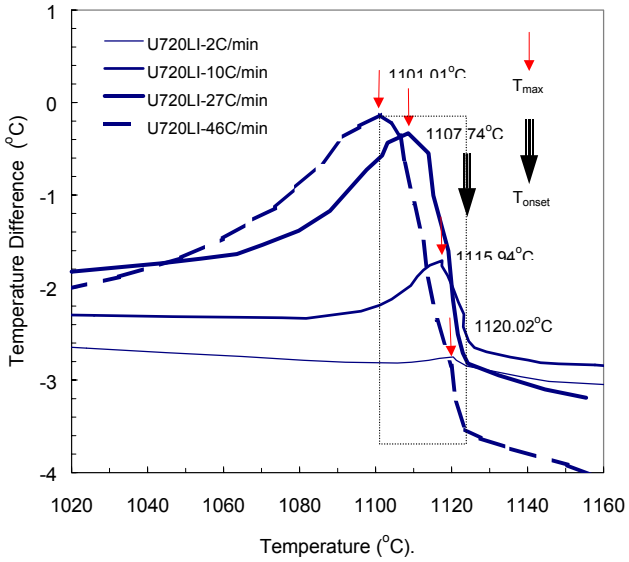

Figure 4.8 Variation of undercooling and precipitation range with cooling rate, DTA

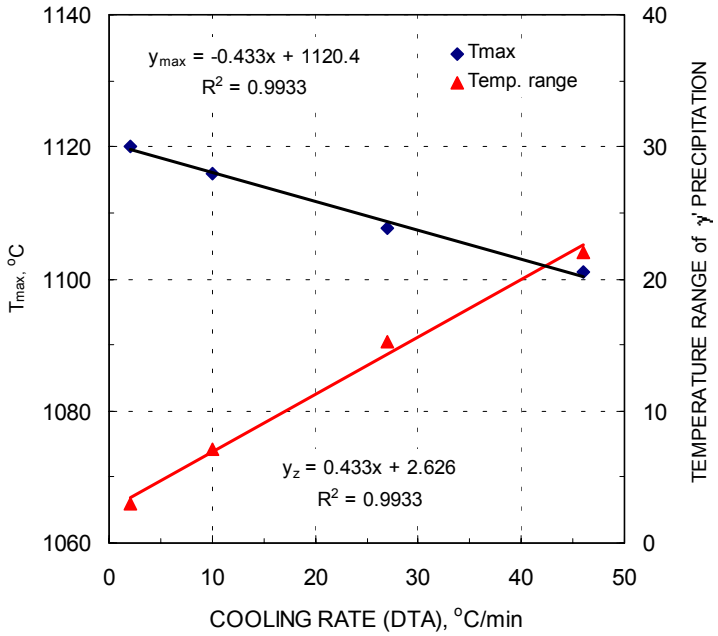

Figure 4.9 Maximum precipitation temperature and the precipitation range as a function of cooling rate in U720LI

For U720LI, at a cooling rate of 55°C/min, the temperature at which maximum precipitation takes place is around 1096°C (2000°F) from extrapolation. The precipitation range is from 1150°C to 1096°C (2100~2000°F), which shows an undercooling of 54°C. Because of the existence of the precipitation range where nucleation dominates, the average size of the precipitates remains relatively stable within that temperature range. As the temperature falls below the precipitation range, the growth of γ′ dominates the cooling process and the average size of the cooling γ′ starts to increase.

The similar studies were also conducted on Rene88DT. Figure 4.10 shows the variation of T_{onset} ans T_{max} with cooling rate obtained from DTA analysis. The T_{max} against cooling rate also follows a linear relationship. The undercooling varied with cooling rate implies that the γ′ nucleation not only is a result of thermodynamic process, but also of kinetically process.

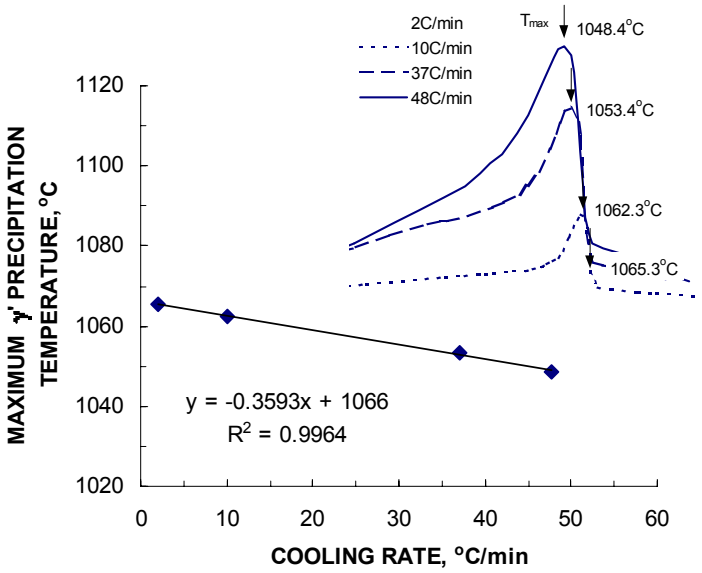

Figure 4.10 Maximum precipitation temperature as a function of cooling rate in Rene88DT

4.4 Summary

1. The cooling precipitation kinetics in U720LI and Rene88DT was studied by a specially designed interrupt cooling method. Empirical models were developed from

the interrupt cooling to describe the relationship between cooling precipitates size and interrupt temperature. And linear relationship was discovered between the mean diameter of the cooling γ′ precipitates and interrupt temperature in both alloys.

2. The size of the cooling γ′ precipitates in Rene88DT is found being smaller than that in U720LI. But the growth rate is higher than in U720LI. No binomial size distributions of the cooling γ′ precipitates were found in both alloys.

3. The γ′ nucleation is found at the certain undercooling, which is controlled by both thermodynamic and kinetic process and varied with cooling rate.

Chapter 5: Strengthening of the materials

The mechanical property of nickel-base alloys is mainly derived from the microstructure, such as grain size and the size distribution of precipitates inside grains and along the grain boundaries. When the solution temperature is fixed during heat treatment, the grain size is pre-determined. Therefore, the key variable left to control the final mechanical properties of the materials in this study is the size and distribution of the γ' precipitates, which is controlled by two key processes, quenching after supersolvus solution treatment and aging treatment. This chapter begins with the study of the tensile strength at different cooling rates in both Rene88DT and U720LI alloys. Then the strengthening behavior at each temperature stage is investigated through interrupt cooling, which gives better understanding of the strength development step-by-step through quenching. The effect of aging treatment on tensile strength is carried out as well.

5.1 The effect of cooling rate on tensile strength

Tensile strength as a function of the cooling rate in both alloys is plotted in Figure 5.1 and 5.2, respectively. In the charts, the dotted lines are as-quenched data and solid line are quenched plus aged data. The upper two lines represent the ultimate tensile strength, and the lower two lines represent the yield strength. It is shown that the cooling rate has a significant influence on the yield strength of both the as-quenched and quenched plus aged specimens. The relationship between the strength and cooling rate follows a power law. The highest cooling rate, which produces the smaller cooling γ' precipitates, results in the highest tensile strength. In practical, the gain in strength through cooling rate is only limited by the potential risk of quench cracking and distortion due to excessive thermal stresses generated during the quenching.

An empirical correlation between the as-quenched yield strength and the cooling rate has been established as:

U720LI: $\log\sigma_y = 2.877 + 0.0427 * \log (dT/dt)$, 5-1

Rene88DT: $\log\sigma_y = 2.935 + 0.0567 * \log (dT/dt)$ 5-2

where as-quenched yield strength σ_y is in MPa, and cooling rate in °C/min.

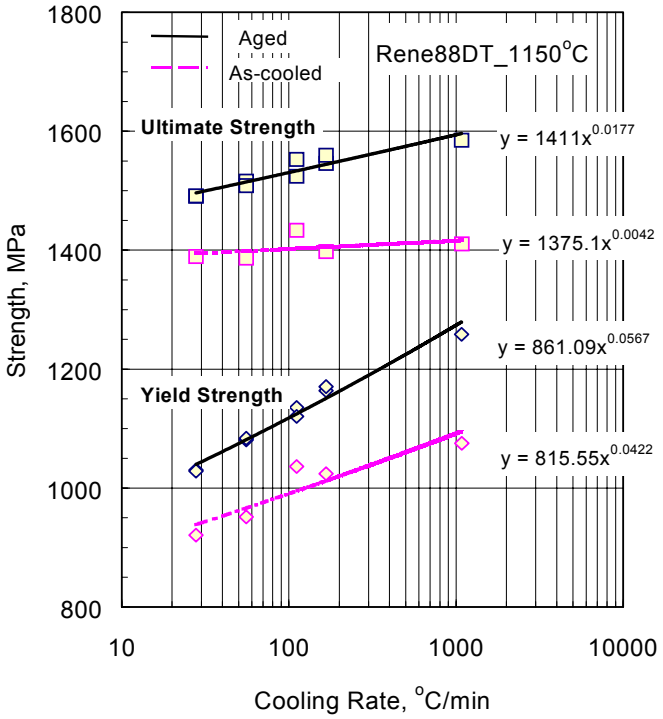

Figure 5.1 Relationship between the tensile strength and the cooling rate in Rene88DT

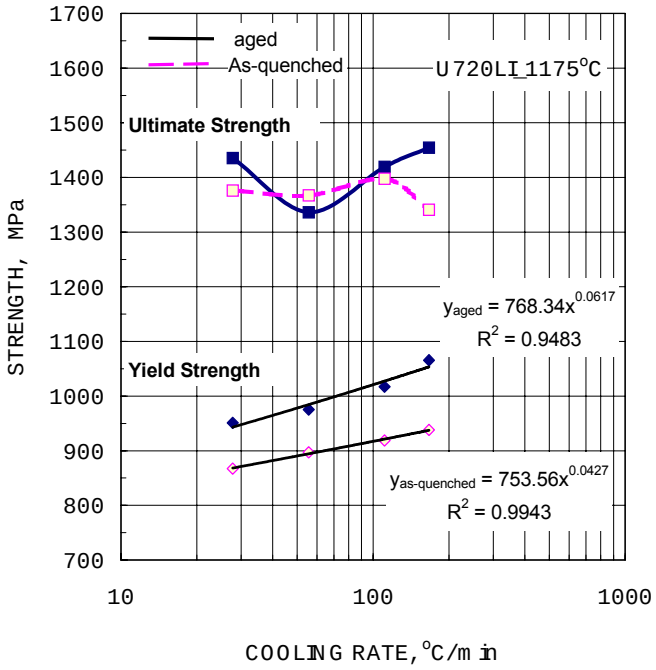

Figure 5.2 Relationship between the tensile strength and the cooling rate in U720LI

The effect of aging treatment on strength was also shown in Figure 5.1 and 5.2. After the single aging treatment (U720LI: 700°C/24hrs, Air Cool, Rene88DT: 760°C/8hrs), all specimens, regardless of cooling rates, show a remarkable improvement in the yield strength compared to the as-quenched specimens. The improvement is about 90 to 130MPa, at cooling rates from 27°C/min to 167°C/min in both alloys. The remarkable increase in the strength means that the aging treatment also plays an important role on the material strengthening. The yield strength of the aged materials can also be approximately estimated from the cooling rate by the following fitting function:

U720LI: $\log\sigma_y = 2.886 + 0.0617 * \log(dT/dt)$ $R^2=0.95$ 5-3

Rene88DT: $\log\sigma_y = 2.935 + 0.0567 * \log(dT/dt)$ 5-4

where the yield strength σ_y is in MPa, and cooling rate dT/dt in °C/min.

However, the equation above should be applied cautiously and only be used when an identical age treatment is excised.

Moreover, it is noted from Figure 5.1 and 5.2 that a higher cooling rate resulted in more aging improvement in strength than a lower cooling rate. That is because a faster quench produces more extensive fine γ' precipitates during late stage quenching or aging.

5.2 Strengthening tendency

Testing of the tensile strength of specimens cooled to different interrupt temperatures led to the study of the strength development during cooling. The as-quenched yield strength and ultimate strength as a function of the interrupt temperature are plotted in Figure 5.3 and 5.4. The first point (leftmost) on the plot corresponds to the strength from the specimen direct quenching to below 650C from the solution temperature. The rest of points correspond to the data for different interrupt temperatures. Before the temperature reached the γ' solvus temperature, the as-cooled strength remained almost constant, but as the interrupt temperature decreased further and passed γ' solvus temperature, both yield strength and ultimate strength decrease dramatically. However, when interrupt temperature reaches around certain temperatures, the strength starts to regain as the

temperature is decreased further. This non-monotonic decrease in yield strength was observed in both alloys. That implies that the material is actually softened at the beginning of quenching and then is strengthened again. However, the amount of the strengthening is not big enough to makeup the strength drops. Therefore, the strength of the interrupt cooled specimens is always lower than that of the one directly quenched to below 650C (or room temperature).

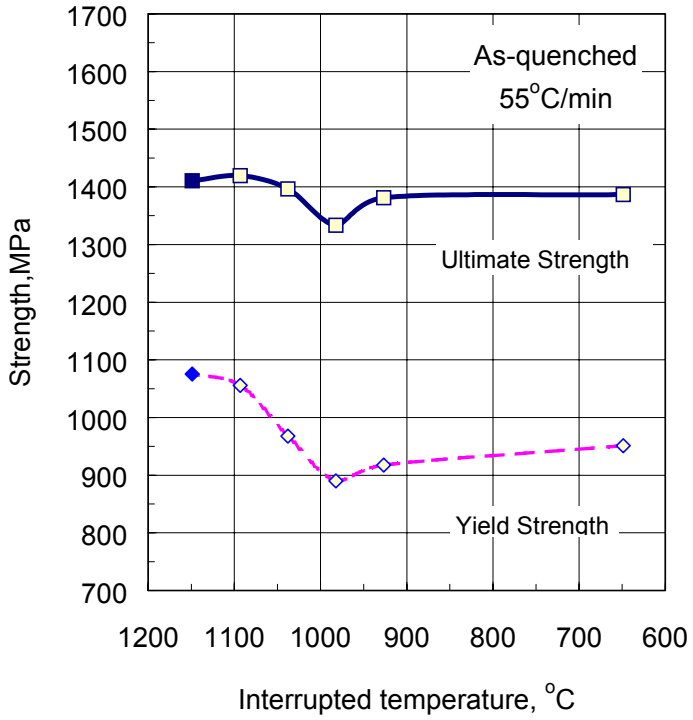

Figure 5.3 The plot of as-quenched strength against the interrupt temperature in Rene88DT

This non-monotonic decrease in yield strength has brought a great interest for further investigations.

To verify this non-monotonic decrease, another two sets of interrupt cooling tests were performed in U720LI samples with different cooling rate, 27°C/min and 176°C/min, and plus aged. Figure 5.5 plotted the yield strength of the quenched plus aged specimens against the interrupt temperatures. It was noted that after aging treatment, this non-

monotonic decrease of the strength still exists, which means that this phenomenon occurs during quench, aging treatment won't affect much.

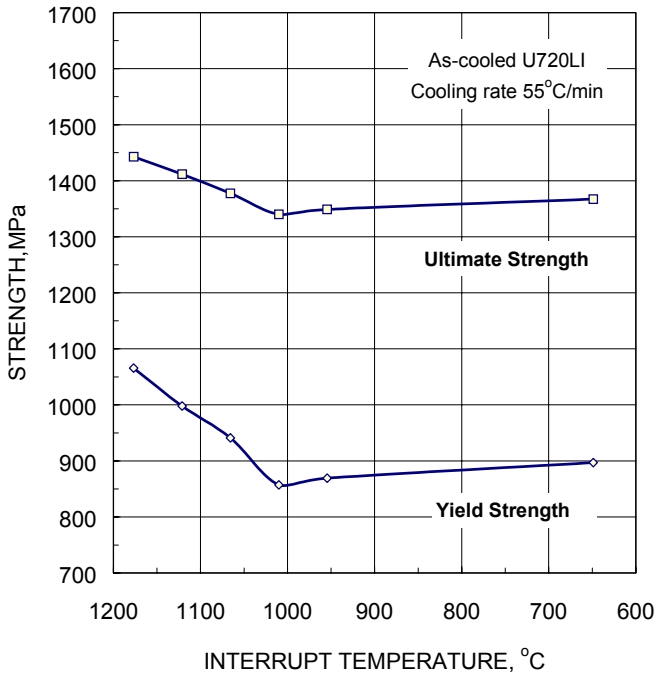

Figure 5.4 The plot of as-quenched strength against the interrupt temperature in U720LI

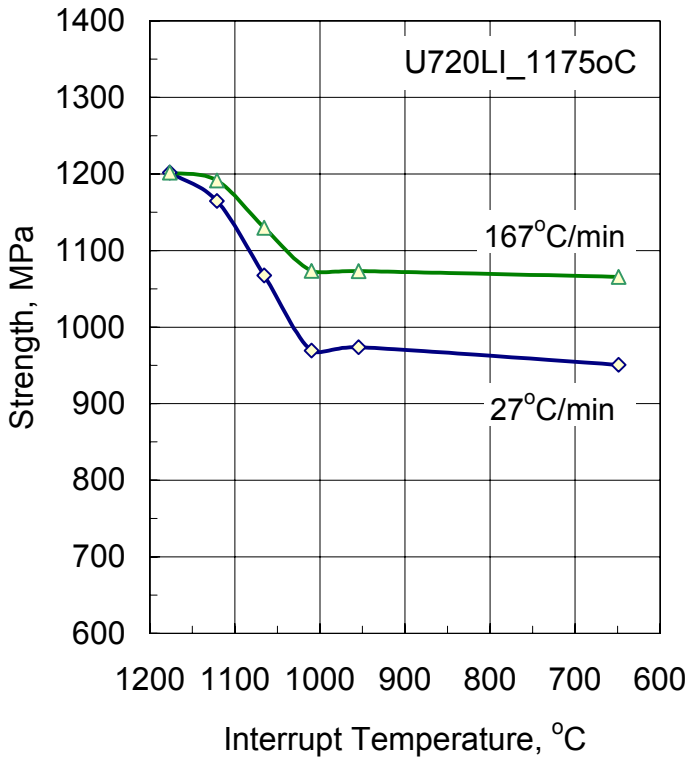

Figure 5.5 The plot of quenched plus aged yield strength against the interrupt temperature

In addition, it is indicated that higher cooling rate resulted in less decline in the strength and always results in higher final strength.

5.3 Fractograph analysis

After the tensile testing, the fracture surface of the specimens were examined under SEM. Figure 5.6 showed the fractograph of the as-quenched tensile specimens, prepared by the interrupt cooling.

In comparison to the specimen quenched directly from the solution temperature (natural cooling sample in Fig.5.6 a), the sample interrupted at 1065°C (Figure 5.6b) shows more ductile dimple fracture feature. The fracture is along the γ' precipitates formed during cooling. As interrupt temperature is further decreased to 954°C, e.g. in Fig.5.6 c, more fine dimples are observed, which is believed to be associated with the small secondary burst of the cooling γ' precipitates.

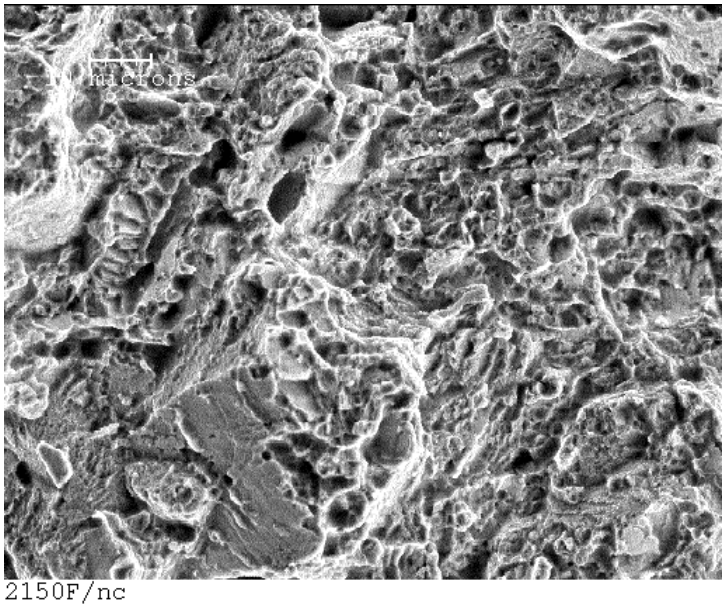

a) Solution: 1175°C, interrupt @ 1175°C

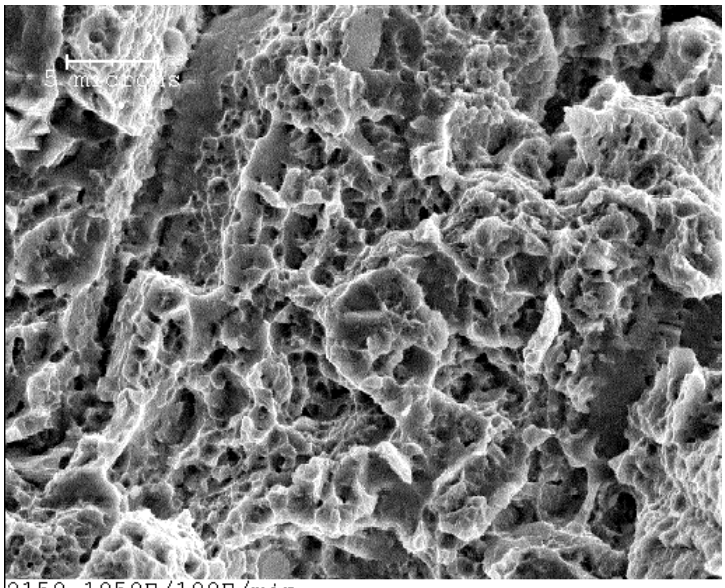

b) a) Solution: 1175°C, interrupt @ 1065°C

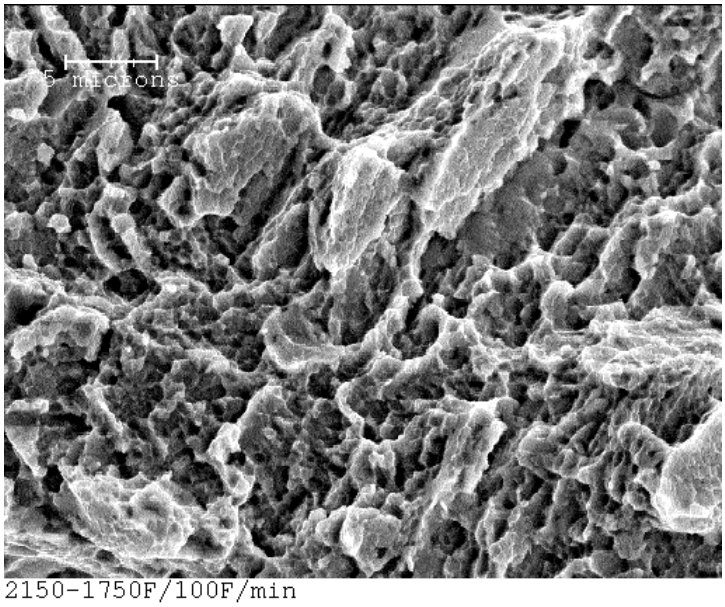

a) Solution: 1175°C, interrupt @ 954°C

Figure 5.6 Fractograph of as-quenched tensile specimen in U720LI

Figure 5.7 shows the fractographs of the quenched plus aged tensile specimens. Figure 5.7 a) is the fractograph of the specimen which was quenched directly to room temperature from the solution temperature and then aged. More brittle fracture feature was observed. The lower left two pictures, Fig.5.7 b) and d), are the fractographs of the specimens interrupted cooled with a quench cooling rate of 27°C/min, the lower right two pictures, Fig.5.7 c) and e), were quenched at 167°C/min. No significant difference is observed between these two groups of fracture features.

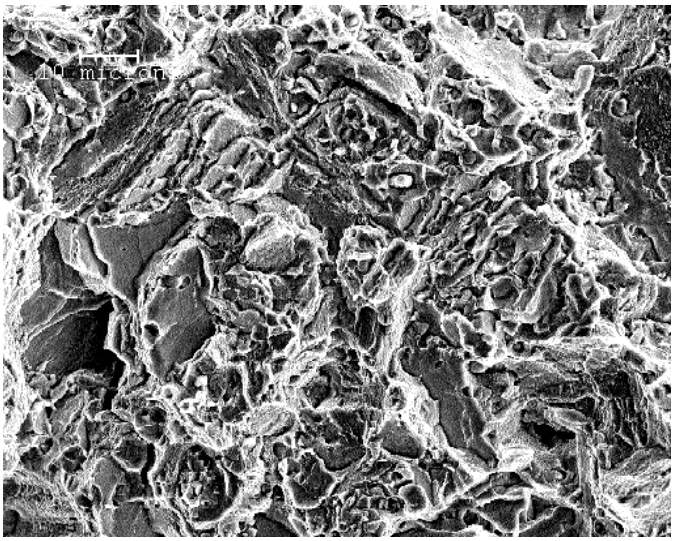

a) Solution: 1175°C, interrupt:1175°C

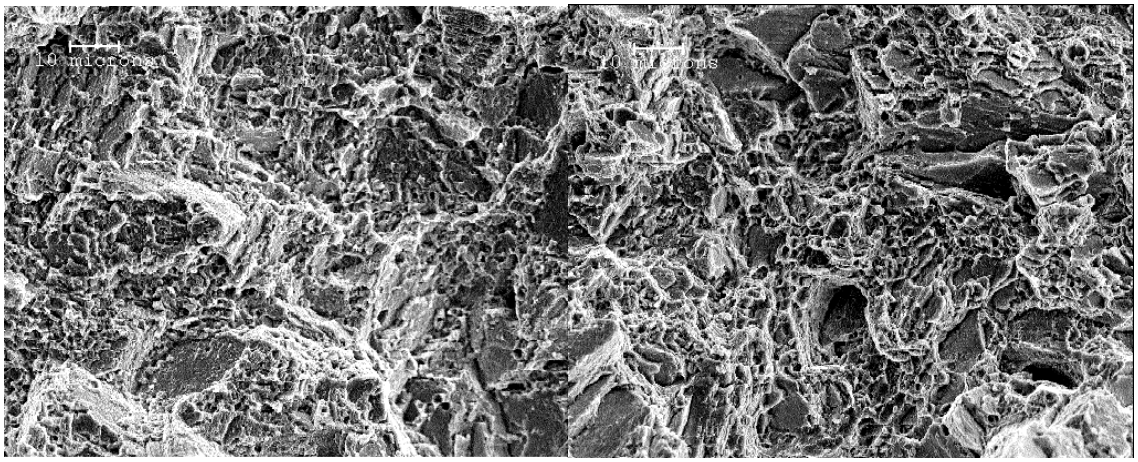

b) Sol: 1175°C, interrupt:1065°C, c) Sol: 1175°C, interrupt:1065°C,

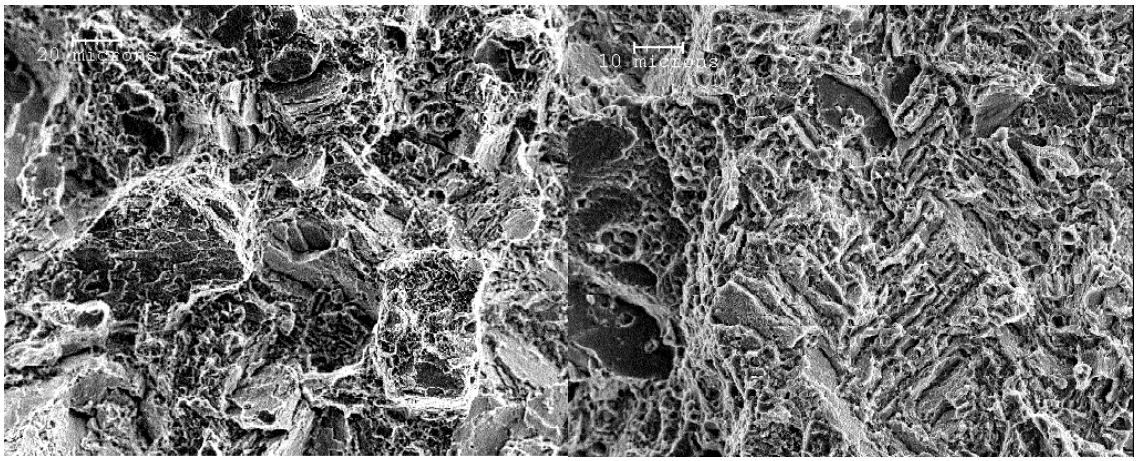

d) Sol: 1175°C, interrupt:1065°C, Cooling rate: 27°C/min

e) Sol: 1175°C, interrupt:1065°C, Cooling rate: 167°C/min

Figure 5.7 Fractograph of as-quenched + aged tensile specimen in U720LI
Ageing: 700°C / 24hrs /air cool

5.4 Discussion

Based on the hardening theory, strengthening of a precipitation-hardened alloy depends upon the precipitate size. There exists a critical precipitate size. If a precipitate size is smaller than the critical size, the precipitate can be cut or deformed by dislocations or weakly coupled dislocation pairs. In this case, the strength increases with the precipitate size. Otherwise, if a precipitate size is larger than the critical size, strongly coupled dislocations may cut in the ordered the precipitates or the dislocations find ways to pass around the precipitates. When by-pass happens, the strength actually decreases with the increase of the precipitate size[13].

In continous cooling circumstance, regardless of the cooling rate, all the precipitates counted are believed to be larger than the critical size. These precipitates act as larger precipitates to cause the decrease in strength as the precipitate size increases. Therefore, the lower cooling rate is, the larger the precipitate sizes are, and the lower strength is to be expected.

In the interrupt cooling with a cooling rate of 55°C, once the cooling precipitates burst as the temperature passes γ' solvus temperature, they grow fast with the further decrease in temperature. Those first burst cooling γ' precipitates actually behave as the larger

precipitates to cause the decrease of the strength with the growth of γ' precipitates at the early stage of quenching, which means that the first burst γ' precipitates will not continuous formed. This conclusion supports the burst theory. However, when the temperature is dropped to a certain point, the strength starts to increases with the further decrease of temperature. This increase is believed to be accounted by the additional tiny γ' precipitates burst [27]. The secondary nucleation of γ' precipitates is a result of the competing processes of supersaturation generation due to the continuous cooling and supersaturation consumption due to the first burst γ' precipitation and growth. Because these tiny γ' are formed at relative lower temperature, and therefore, their growth was strongly restricted by the diffusion-process. The sizes of those precipitates are very small and can only be observed under TEM [3]. Those tiny γ' actually behave as the small precipitates to resist the dislocation cutting-through and cause the increase of the strength with the growth of the tiny γ'. Therefore, the regaining from the initial decline of the strength observed during interrupt quench tests is believed to be the contribution of those secondary burst tiny γ' precipitates. However, because the volume fraction of these tiny γ' precipitates is much less than the first burst γ' precipitates, the strength will not be greatly increased.

Aging strengthening is also believed to be associated with the precipitation and growth of the tiny γ' precipitates during aging. In spite of the size difference in the cooling precipitates, strength increase due to aging always occurs. It has been proved that aging treatment does not cause the first burst cooling γ' precipitates grow significantly [14]. So it is believed that the main micro-structural activity during aging is the continuous growth of these tiny γ' precipitates. Because these tiny γ' participates are so small that weakly coupled dislocations can cut through. Therefore, the strength increases with the increase of the tiny γ' precipitates size during aging. Moreover, higher cooling rate results in more strengthening after aging. That is because higher cooling rate suppresses the growth of the first burst γ' precipitates and provides more supersaturation in the matrix, which results in more tiny γ' precipitates nucleation bursts and growth later on, consequently, more strengthening.

5.5 Summary

1. Cooling rate has strong influence on tensile strength. The relationship follows a power law in both alloys. Aging treatment also plays an important role in the strengthening, which improve the yield strength about 90 to 130 MPa in both alloys.

2. Of great interest is that the yield strength decreases with the interrupt temperature, and the decrease shows non-monotonic phenomenon. Multi-stage nucleation is considered to be accountable for the non-monotonic decreasing.

Chapter 6: γ′ growth kinetics during isothermal aging

Unlike in continuous cooling, where the supersaturation in the matrix is varied as temperature decreases, isothermal aging starts with a predetermined supersaturation in the matrix by the previous process, i. e. the quenching after the solution treatment. The precipitation at the onset of the isothermal holding consumes all the supersaturation, followed by the coarsening of the γ' precipitates at a fixed temperature. Therefore, the growth and coarsening kinetics of γ' precipitates will differ from that in the continuous cooling. This chapter is aimed to study the coarsening kinetics under isothermal aging conditions and the activation energy during coarsening.

6.1 Morphology of γ' precipitates during isothermal aging

The morphology of the γ' precipitates in Rene88DT is shown in Figure 6.1 and 6.2. For Rene88DT, the aging temperature is from 1020° to 1080°C and aging time is from 4 minutes to 128 minutes. For U720LI, the aging temperature is from 950°C to 1121°C with aging time up to 64 minutes. Figure 6.3 and 6.4 show the γ' morphology changes in U720LI.

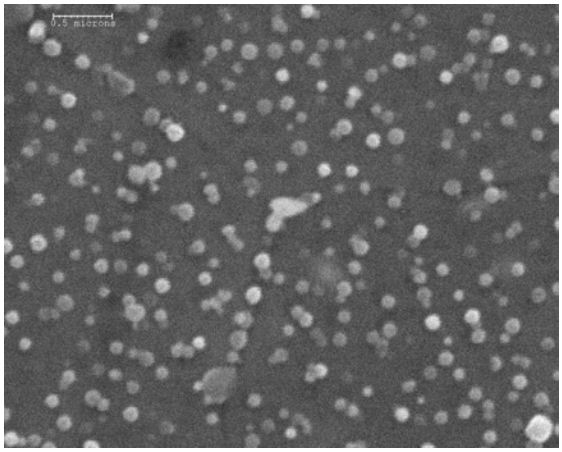

1080°C / 4min

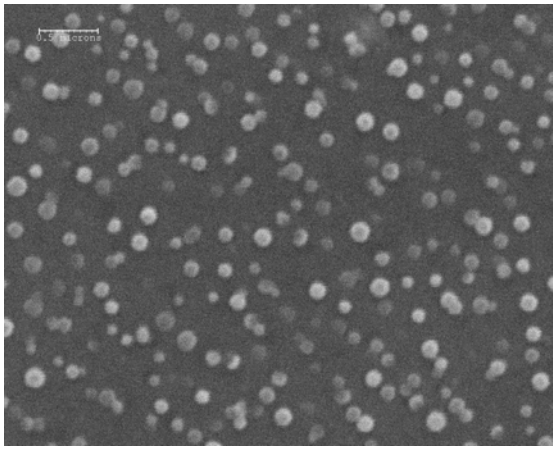

1080°C / 8min

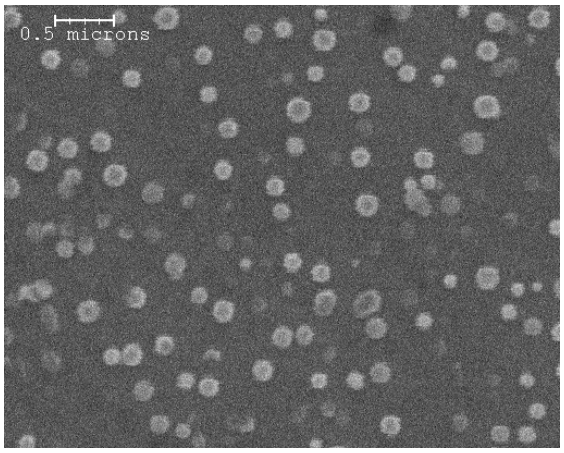

1080°C / 16min

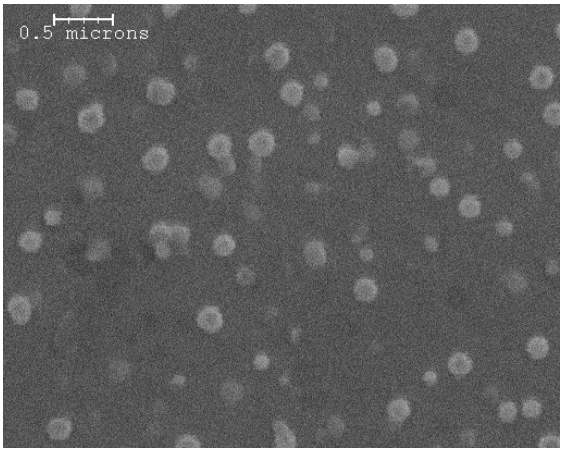

1080°C / 32min

Figure 6.1 Microstructure at 1080°C aging in Rene88DT

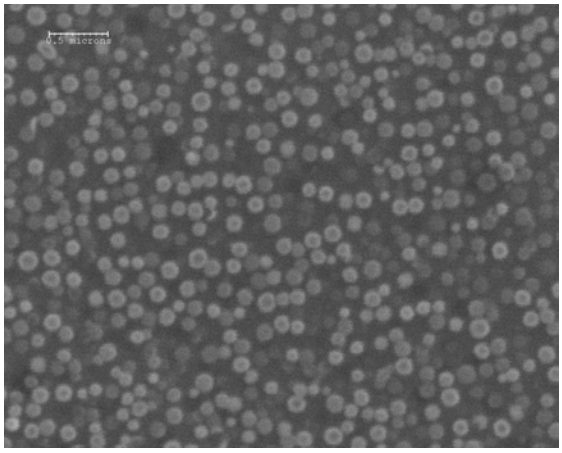

1020°C / 16min

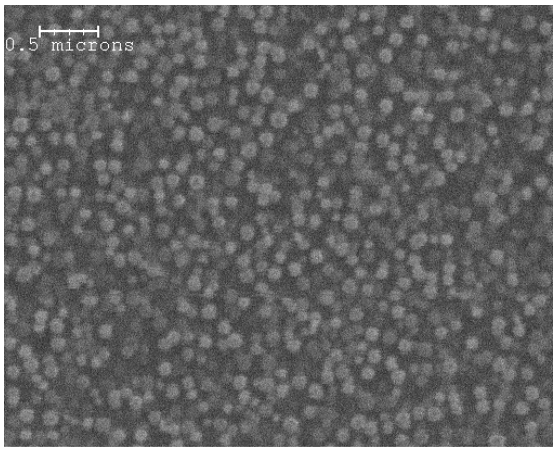

1020°C / 32min

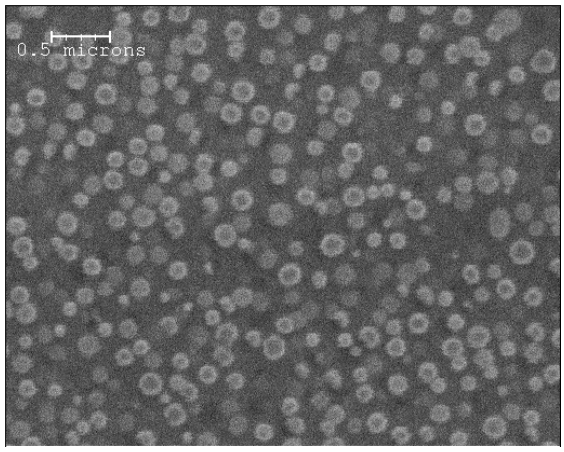

1020°C / 64min

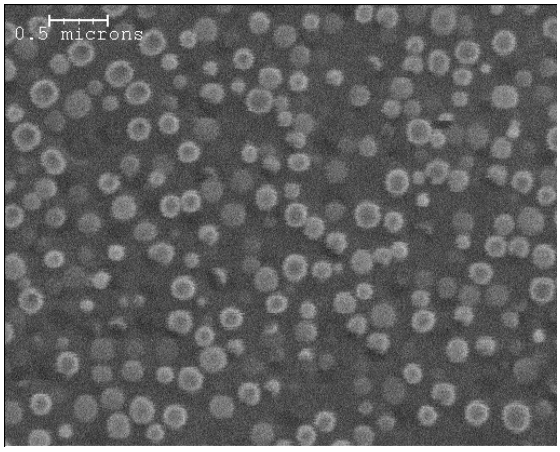

1020°C / 128min

Figure 6.2 Microstructure at 1020°C aging in Rene88DT

As seen in Fig.6.1 .and 6.2, all γ' phase appears to be spherical, even after 128 minutes aging. The γ' precipitates grow with the time increases. On the other hand, the particle density decreases with time increases, which indicates that coarsening is proceeded by the consumption of small particles.

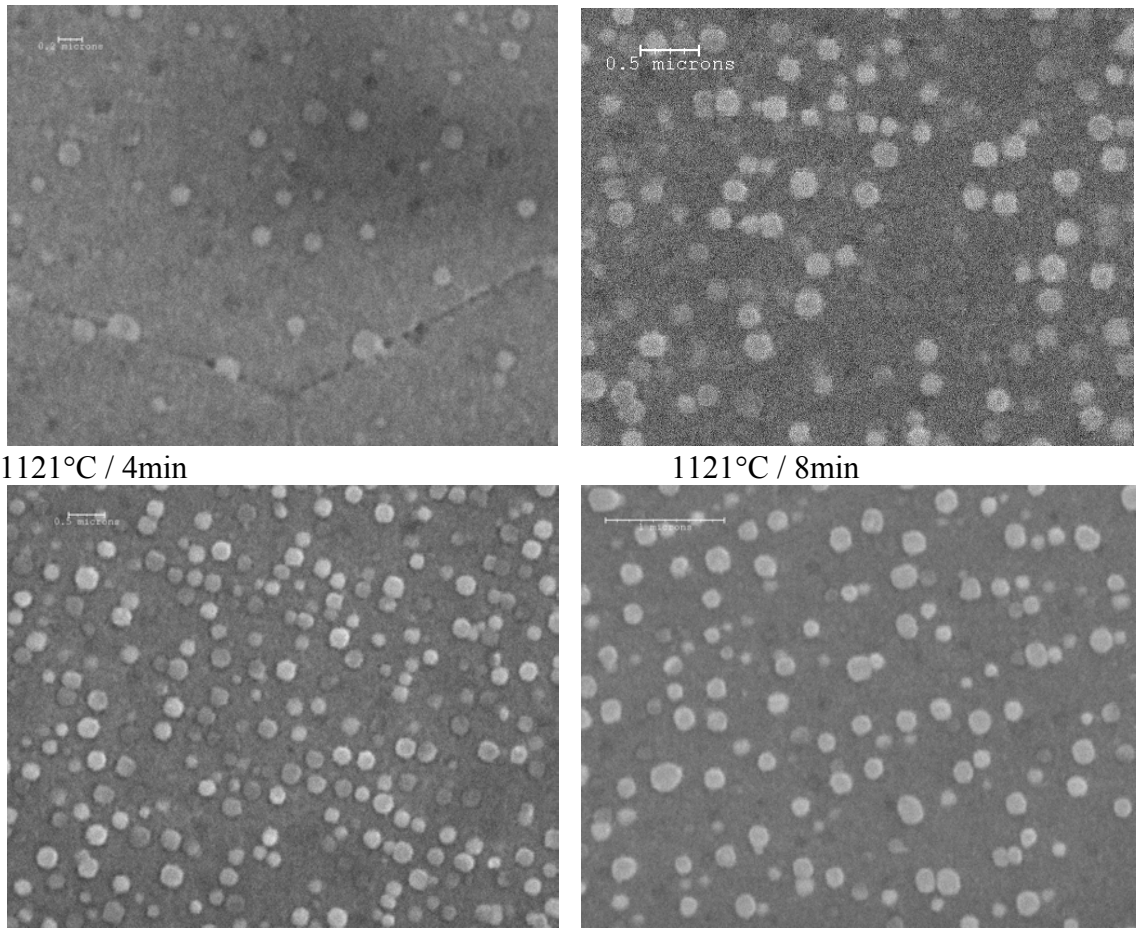

1121°C / 4min 1121°C / 8min

1121°C / 16min 1121°C / 32min

Figure 6.3 Microstructure at 1121°C aging in U720LI

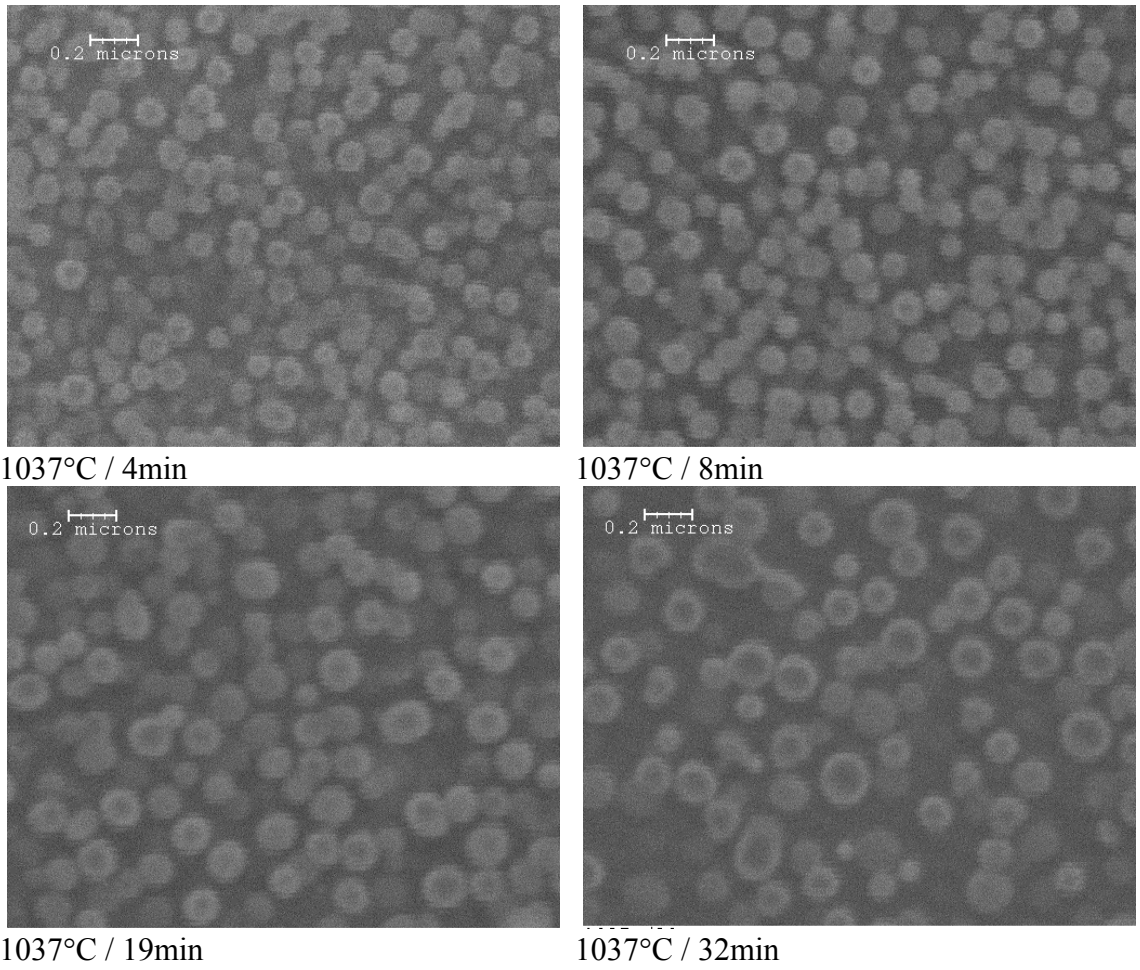

1037°C / 4min 1037°C / 8min

1037°C / 19min 1037°C / 32min

Figure 6.4 Microstructure at 1121°C aging in U720LI

6.2 Coarsening model

The mean radius of the γ' precipitates in Rene88DT and U720LI were shown as a function of holding time in Figure 6.5 and 6.6 over entire temperature range studied. It was found that even though the holding time is short and the aging temperature is high in both alloys, the coarsening kinetics of the γ' phase is in good agreement with the Lifshitz-Slyozov-Wagner (LSW) theory, which predicts the average particle radius, $\bar{r}$, increases with time t according to the following equation:

$$r^3 - r_0^3 = Kt \qquad 6\text{-}1$$

where $\bar{r}_0$ is the average particle radius at the onset of coarsening. The rate constant, K, is given by [24]:

$$K = 2\frac{\sigma D C_e V_m^2}{\rho_c^2 RT} = \frac{C_e}{T} A \exp(-Q/RT) \qquad 6\text{-}2$$

and $D = D_0 \exp(Q/RT)$

where σ is the precipitate-matrix interfacial energy. D is the diffusion coeffecient of the solute in the matrix. Ce is the concentration of solute in equilibrium with a particle of infinite size, Vm is the molar volume of the precipitate, ρc is a constant related to the distribution of particle sizes, R is universal gas constant, and T is the absolute temperature.

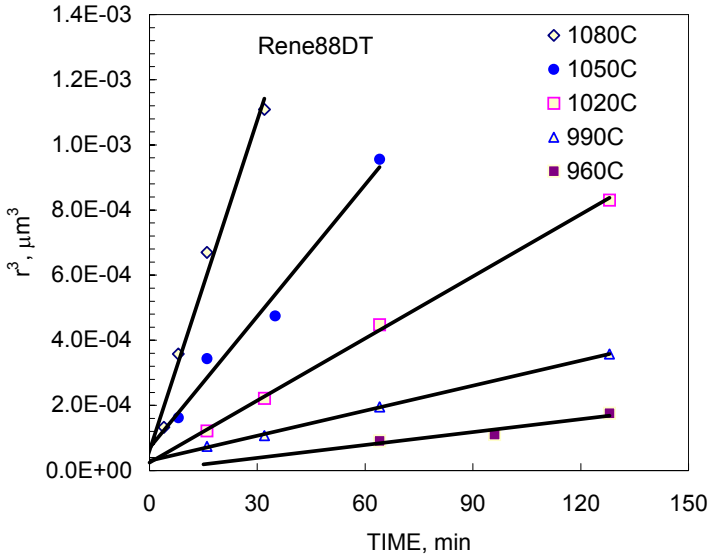

Figure 6.5 The mean radius of the γ' precipitates vs. holding time at different temperatures in Rene88DT

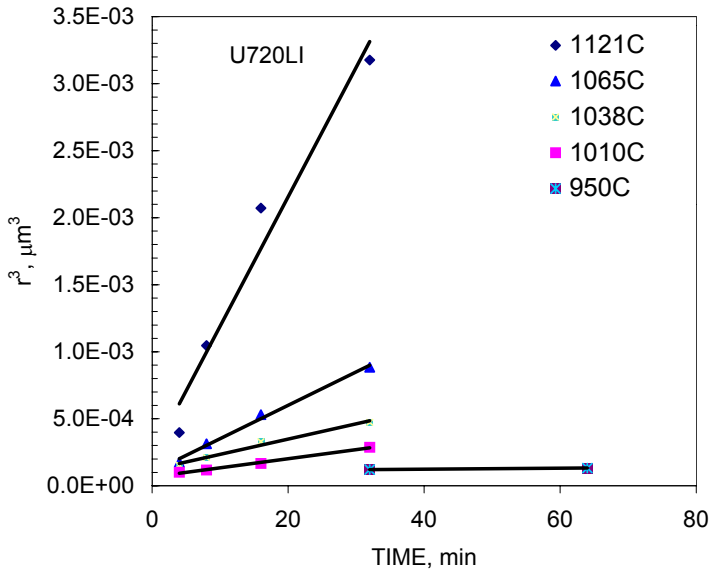

Figure 6.6 The mean radius of the γ' precipitates vs. holding time at different temperatures in U720LI

The activation energy, Q, for coarsening was obtained by plotting k vs 1/T, which usually assumes that the Ce/T term in equation 6-2 did not significantly influence the value of Q. However, it was found the dependence of temperature in our calculation. Using Thermo-Calc, all the mole fraction of the γ-matrix forming elements was calculated as a function of temperature. The Ce was obtained by summing up the mole fraction of Al, Ti, and Nb, and plotted as a function of temperature in Figure 6.7.

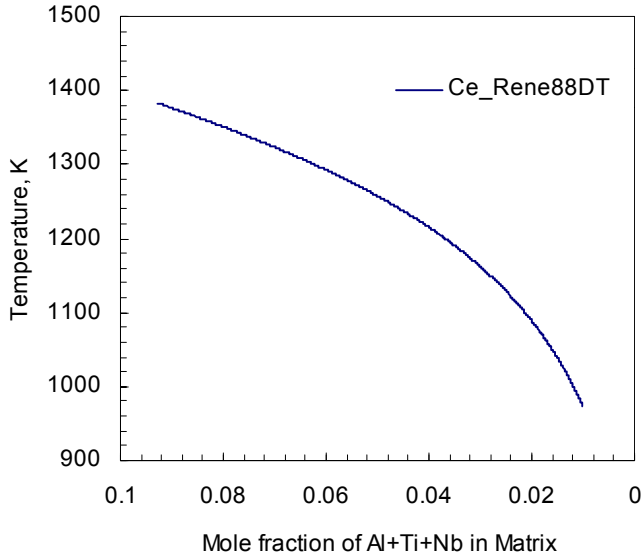

Figure 6.7 Matrix equilibrium compositions as a function of temperature in Rene88DT

By substituting the Ce into equation 6-2 and plotting ln(KT/Ce) vs 1/T, as shown in Figure 6.8 and equation 6-3, the slope of this line yielded an activation energy for γ' coarsening of 316KJ/mol.

$$Ln(KT/Ce) = LnA - \frac{Q}{R}\frac{1}{T} \qquad 6\text{-}3$$

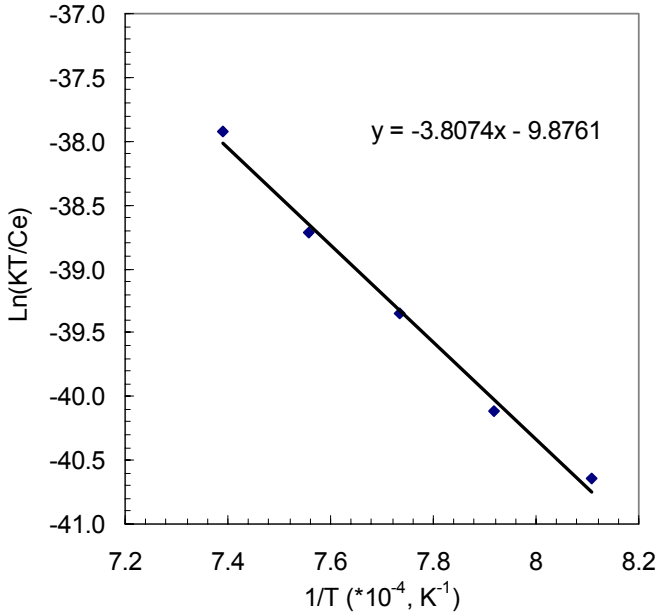

Figure 6.8 Plot of $Ln(KT/Ce)$ against 1/T in Rene88DT

The magnitudes of Q for both alloys seem higher than the published data for the other nickel base superalloys, which is between 250KJ/mol and 325KJ/mol [24, 41]. The reason is believed to be related to the following factors. One is that the isothermal aging temperature is much higher than usual aging temperature; the second is that the holding time is much shorter than common aging time. Therefore, the system actually might not reach to equilibrium condition.

6.3 Summary

1. Microstructure changes during isothermal aging in both alloys were studied. It is evidenced that coarsening happened as the larger particle grew by consumption of the

small particles, which resulted in the particle density decreases with the increase of time.

2. LSW law, $r^3 - r_0^3 = Kt$, for coarsening is obeyed even though the holding time is short and the aging temperature is high.

3. Activation energy, Q, for γ' coarsening yielded is 316KJ/mol for Rene88DT, which is alitter bit higher that published data for other nickel base superalloys. The reason is believed to be associated with the shorter aging time and the higher aging temperature.

Chapter 7: Computer simulation of the cooling γ′ precipitation

7.1 Introduction

The main objective of this chapter is to extend the understanding of the γ′ precipitation during continuous cooling using computer simulation. The simulation tool developed will be able to predict the size and the size distribution of the cooling γ′ precipitates. The model alloy studied is Rene88DT only because of the time limitation.

The chapter starts with the description of the related theories, including classic nucleation theory, diffusion-controlled growth theory and Ostwald ripening theory. Then, the energy-driving concept and thermodynamic calculation approach used in the simulation program is introduced with the help of a flowchart. This is followed by the determination of the individual variables such as Gibbs energy, composition and the energy criterion. Finally, the simulation result is presented and discussed, with the comparison between the simulation result and the experimental data.

7.2 Model theories

γ' precipitation during quenching is a complex thermodynamic and kinetic processes, which involves three basic stages: nucleation, growth and coarsening. These three stages compete with each other and must be taken into consideration simultaneously in any serious computer simulation models. The classic theories describing each of the stages are discussed below.

7.2.1 Nucleation[17]

Based on the classic nucleation theory, as described in Chapter 1, the nucleation is driven by the energy difference in a system. If a nucleus having a volume of V_β and a surface area of A_β is formed, the energy change in the system will be

$$\Delta G = V_\beta \cdot (\Delta G_V + \Delta G_E) + A_\beta \cdot \sigma \qquad 7\text{-}1$$

where ΔG_v represents the decrease in the volumetric Gibbs free energy which drives the nucleation of a new phase. ΔG_E represents the strain energy induced by the newly formed

phase. The introduction of the interface area between the matrix and the nucleus is represented by the interfacial energy σ. Equation 7-1 clearly shows that the energy change due to the nucleus formation is size dependent. A plot of the ΔG vs. the nuclei radius r is shown in Figure 7.1. Since the volumetric energy is proportional to r^3 and interfacial energy is r^2, the energy change with the nuclei radius is not synchronous, as show in Figure 7.2 by the red line. There is an energy barrier to overcome before any nuclei can grow stably. The critical radius r* for a nuclei to survive and the correspondent energy barrier ΔG* are given in Equation 7-2:

$$r^* = \frac{2\sigma}{\Delta G_V + \Delta G_E}$$

$$\Delta G^* = \frac{16\pi \cdot \sigma^3}{3(\Delta G_V + \Delta G_E)^2} = \frac{4\pi\sigma}{3} r^{*2} \qquad 7\text{-}2$$

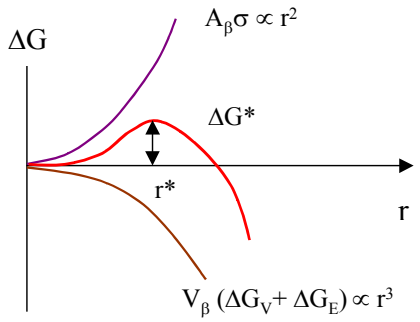

Figure 7.1 Scheme of critical energy of the nucleation

The physical meaning of Figure 7.1 and equation 7.2 is that if a nucleus formed by structural and energy fluctuation in the system exceeds the critical radius r*, any addition to it will reduce the system energy. Therefore, it obtains the momentum to grow autonomously.

Considerable discussion that has been given to the nucleation process in the literature is that it requires the system structural rearrangement besides the energy requirement as described above. The movement of atoms or components involved in the nucleation process is a rate-controlled kinetic process. The complicated theoretical treatment of the steady-state nucleation rate I (per unit volume) in a condensed system can be found in depicted as [17]:

$$I = n_v A^* \nu \exp(-\frac{\Delta G_m}{kT}) \exp(-\frac{\Delta G^*}{kT}) \qquad 7\text{-}3$$

where

ν — atom vibration frequency;

ΔG_m — atom imigrating activation energy;

$v\exp(-\frac{\Delta G_m}{kT})$ — the frequency of an atom nearby the nucleus surface jumping into the nucleus;

A* — the number of the sites on the surface of the critical nucleus which can accept atoms;

n_v — the number of the atomic site per unit volume which can form nucleus.

ΔG^* - the critical energy of the nucleation

Equation 7-3 represents that the physics involved in the formation of a nuclei includes two aspects: 1) the thermodynamic driving force ΔG as shown in equation 7.1, which is the function of the undercooling. Usually, the larger the undercooling is, the higher the driving force is, and therefore the higher rate of the nucleation is. 2) The kinetic possibility of the atoms located near the nuclei to be transferred into the nuclei. This is realized by the vibration of the atoms and the jumping of an atom out from its normal position into the nuclei. Naturally, the higher the temperature is, the stronger an atom vibrates and the higher possibility for an atom to get into the nuclei.

Detailed treatment of the nucleation kinetics can be found in literature [13]. It always concludes with very complicated formulas and several assumptions and simplifications. Some of the physical parameters are still not be able to quantify using any quantum physics methods. Therefore, a few empirical equations and adjustable constants are always introduced to calculate the nucleation rate in the past literature [13, 17, 18, 42], which makes the kinetic treatment more of an art for practical purposes.

Observations of the γ′ nucleation process in the past have shown that it is very easy to accomplish in nickel base alloys. Examples in literature have shown that γ′ nuclei are readily available in these alloys even under super high speed quenching processes. Nuclei of γ′ phase can be easily found in powders or ribbons quenched at 10^3K/s or higher [40]. Based upon these observations, it is believed that the structural fluctuation is not as

crucial a factor in the γ′ nucleation. The nucleation process can be simplified and treated as a thermodynamically controlled process.

7.2.2 Growth [42]

Once a precipitate nucleates, it will grow instantly to reduce the free energy of the system to its minimum level, and the system will tend to approach its equilibrium state. The driving force for the growth is the composition difference in the element solubility between the new γ′ precipitates and the γ-matrix. Precipitate grows through a long-distance diffusion of the solute elements. The diffusion moves the γ-γ′ interface from the precipitates into the γ-matrix.

The growth scheme of a γ′ precipitate with a composition of $C_{\gamma'}$ from the quenched γ-matrix is outlined in Figure7.2. The composition with the newly formed particle is assumed to be uniform. The composition of γ-matrix at the interface between the γ-matrix and the γ′ precipitate is C_{inf}. As the interface moves from the γ′ precipitate to the γ-matrix, analysis of the mass transfer at the interface combining the mass conservation equation yields[42]

$$A = \frac{(C_{\inf} - C_0)(C_{\inf} - C_0)}{(C_0 - C_{\gamma'})(C_{\inf} - C_{\gamma'})} \cdot D^{\gamma} \qquad 7\text{-}4$$

$$R^2 = R^2 + A \cdot \Delta t$$

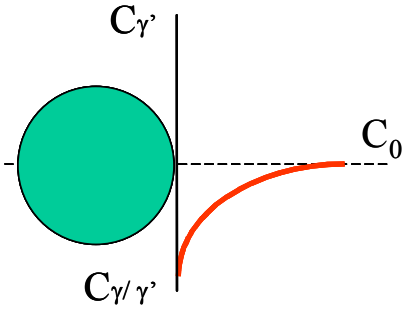

Figure 7.2 Scheme of a spherical particle growth

where R is a radius of the particle, t is time, C_{inf} is the solute content of γ-matrix at the interface, C_0 is the initial γ-matrix composition, $C_{\gamma'}$ is the γ′ phase composition. D^{γ} is the diffusivity of the solute elements in the matrix.

In above equation, the interface composition C_{inf} for a precipitate with radius r can be calculated using the Gibbs-Thompson equation [42]:

$$C_{\inf} = C_{\gamma}(1 + \frac{1 - C_{\gamma}}{C_{\gamma'} - C_{\gamma}} \cdot \frac{2V_m \cdot \sigma}{RTr}) \qquad 7\text{-}5$$

where C_γ is the γ-matrix composition,

7.2.3 Coarsening [42]

At the later stage of the precipitation, the molar fraction of the γ′ precipitates is close to the equilibrium amount. The γ-matrix is no longer saturated with the solute elements. Nucleation and growth cease to be the predominant mechanisms for the γ′ precipitation. However, the interface energy between the γ′ precipitates and γ-matrix can still drive the coarsening of the already formed particles and change their sizes. The particle coarsening is driven by the solubility difference between the large particles and the small particles, according to the Gibbs-Thompson equation. The driving potential is provided by the reduction of the total interfacial energy while the total volume fraction of γ′ precipitates remains the same. Therefore, the mass transfer from larger particle to small particle is the major activity during coarsening, which results in the growth of the larger particle accompanied by the shrinkage of the small particles, as seen in Figure 7.3.

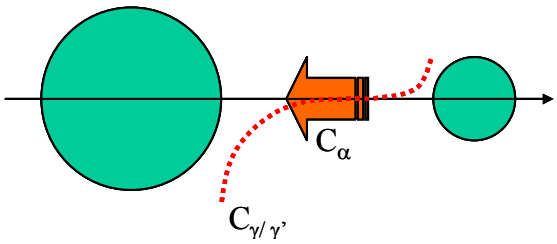

Figure 7.3 Scheme of a mass transform during coarsening

The classic theory developed by LSW on Ostwald ripening gives the following equation to calculate the size of the coarsened particles [42]:

$$a = \frac{6D\sigma V_m^2 C_e}{RT} \cdot \left(\frac{r}{\bar{r}} - 1\right) \qquad 7\text{-}6$$

$$R^3 = R^3 + a\Delta t$$

where n - the number of particles.

Ce -- the equilibrium solute concentration, which can be calculated from Thermo-Calc

$\bar{R} = \sum R_i / n$ -- the average particle size

There were several other much more complicated forms of the equation in the literature considering the volumetric effects of the precipitates, the morphology and other factors.

But their formulations remain essentially the same. Therefore we have selected to use equation 7-6 in our simulation.

Comparing equation 7-4 and equation 7-6, we can see the difference between growth and coarsening, even though their controlling mechanism of particle expansion is the same diffusion. The growth follows a square law, while the coarsening follows a cubic law.

7.3 Simulation model description

7.3.1 Energy-driving concept introduction

Based on the thermodynamics, a system is tending to precipitate another phase to lower its system energy if an equilibrium system becomes non-equilibrium. Since the γ′ precipitation reactions in superalloys are very complicated because of a dozen of components are involved, we use a simplified two-component system to illustration of the equilibrium precipitation . As temperature decreases during cooling, γ matrix becomes unstable, which provides a chemical potential for γ′ phase to nucleate and grow from the γ-matrix. Figure 7-4 illustrates the phase transformation situation. An alloy having composition Co will have system energy at point O if no decomposition occurs. This energy is much higher than the equilibrium energy at point C.

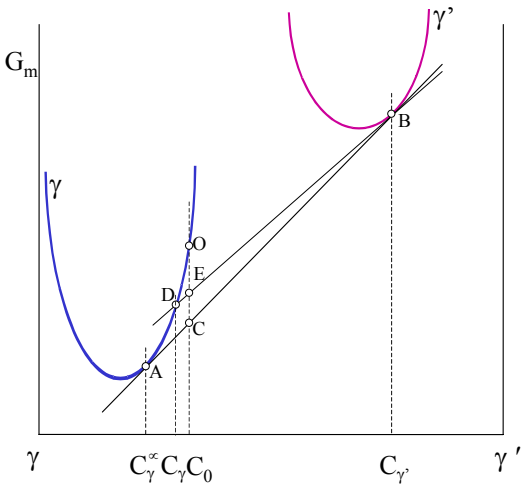

Figure 7.4 Scheme of nucleation driving force

Therefore there is a driving force for the precipitate formation. Under equilibrium precipitation condition, the energy and composition of the different phases in the system is defined by the tangential line between the γ-matrix and the γ′ phase energy curves and hence the points A, B and C. The equilibrium compositions of the γ-matrix and γ′ phase will be C_γ at point A and $C_{\gamma'}$ at point B, respectively. The equilibrium energy of the γ-

matrix, γ′ and the system is determined by A, B and C respectively. The γ′ volume fraction in the system is the ratio between the line segment AC and AB (The leveler rule), i.e.

$$_{e}Vf_{\gamma'}=AC/AB \qquad 7\text{-}7$$

It can be seen that under equilibrium conditions, the tangential line completely defines the system: the energy and composition of each phase and the ratio of phase quantity.

However, it is impossible to obtain an equilibrium condition in a quenched system. It is actually the purpose of quenching to retain a highly supersaturated not-equilibrium matrix for further exploitation of the phases to obtain desired mechanical properties. The quenching process takes advantage of the kinetic factors, i.e., the slow movement of the atoms during nucleation and diffusion, to freeze the solute elements in the matrix. The γ-matrix composition in this non-equilibrium case will be at point D, which is more close to the original alloy composition. Assuming the γ′ composition remains the same as in the equilibrium case, which have been generally accepted true in literature[13], we can apply the same leveler rule on point D, E and B. Thereafter, we have the descriptives of the system:

- Gibbs energy and composition of the γ′ ($G_{\gamma'}$ and $C_{\gamma'}$)*:* point B, same as in the equilibrium condition.
- Matrix composition: point D, defined by the leveler rule and the composition conservation.

$$C_0 = Vf_{\gamma} * C_{\gamma} + Vf_{\gamma'} * C_{\gamma'} \qquad 7\text{-}8$$

- System energy (Gsys): Point E, which is higher than the equilibrium system energy C.

$$G_{sys} = Vf_{\gamma} * G_{\gamma} + Vf_{\gamma'} * G_{\gamma'} \qquad 7\text{-}9$$

- The difference between them is EC, defined by the kinetic factors that prevent the system to obtain its equilibrium, such as nucleation (excess energy for nucleation) and diffusion.

And remember that

$$Vf_{\gamma} + Vf_{\gamma'} = 1 \qquad 7\text{-}10$$

And the relationship between the γ-matrix energy G_{γ} and the composition C_{γ} is defined by the Gibbs energy function of the matrix,

$$G_{\gamma} = G_{\gamma}(C_{\gamma})$$

which is obtained from the Thermo-Calc in this study.

Since the four unknowns for the matrix need to be solved by the four equations, the complete system is well defined. The tasks left are to determine the equilibrium composition and energy of phases (point A and B), equilibrium volume fraction to calculate the system energy (Point C), the energy barrier for the nucleation (to determine point E) and the Gibbs energy function of the matrix (to determine point D).

7.3.2 The algorithm and code description

The code was developed in Microsoft Excel®to integrate the three basic processes and embed the energy-driving concept into the simulation. The algorithm is explained by the flow chart in Figure 7.5.

1) The alloy is initially hold at its solution temperature. The γ-matrix has the alloy composition C_0. When alloy is cooled to below γ'-solvus, excess energy, which is above the equilibrium system energy, is built up (E-C in Figure 7-4).
2) If the excess energy exceeds the energy barrier, then nucleus may form & grow to consume the excess energy. This step is cycled until all the excess energy is consumed and no more nuclei can be formed. At that point, the excess energy is equal to the energy barrier for nucleation.
3) At the next time step of cooling, the nucleus form & grow to counterbalance the system energy increase. However, the growth may not be quick enough to consume all the excess energy. If the excess energy left is still higher than the energy barrier for nucleation, more nucleus are formed and grown to consume the excess energy down to the level that no more nucleus can be formed, i.e., to the level as the energy barrier for the nucleation, as described in 2). If the growth process can consume the excess energy to the level less than the nucleation

energy barrier, no new particles can be formed and the system has to be cooled further to provide the energy needed for either growth or nucleation

4) At a certain point of the cooling process, excess energy in the system may be very low. The system is close to equilibrium. Growth cannot happen because there is not enough supersaturation available. At that point, the only mechanism for the precipitation is coarsening. The excess energy for the coarsening to set in is called coarsening energy barrier.
5) Every particle was treated individually in the model. Therefore, the size distribution of γ′ precipitates can be obtained.

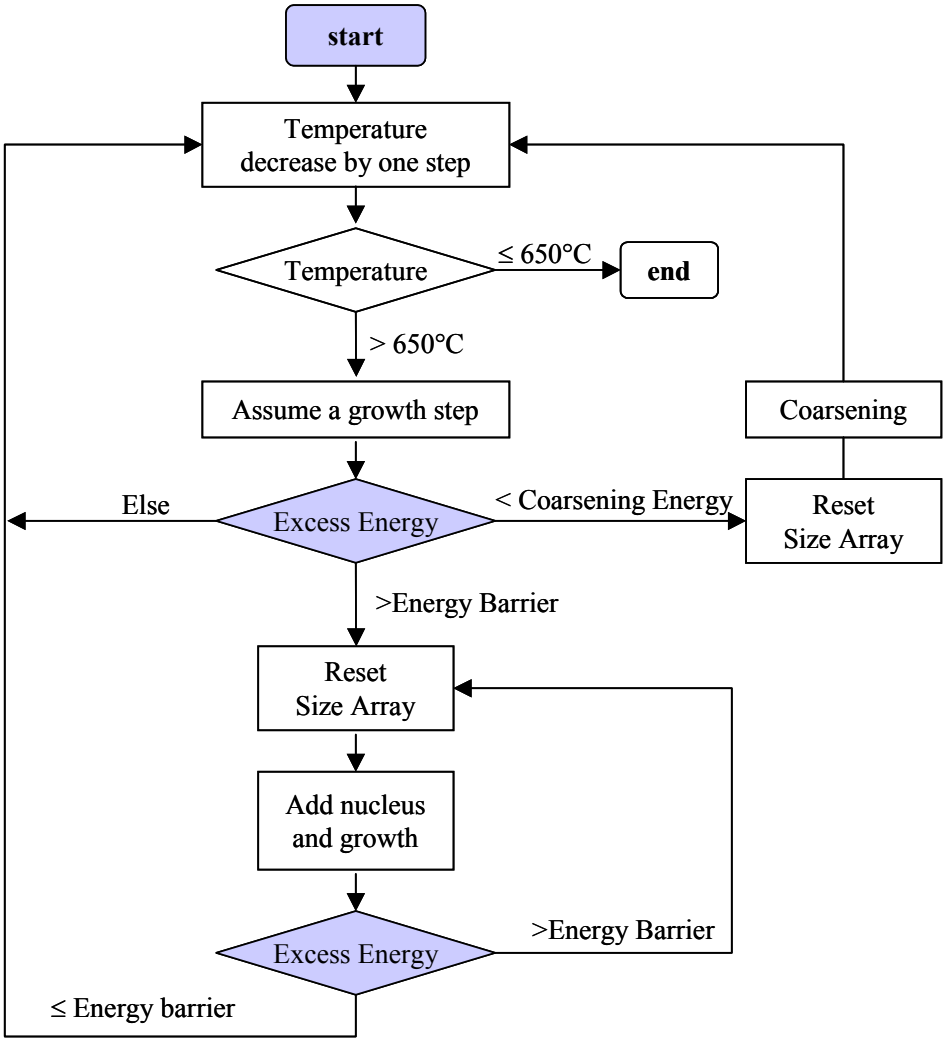

Figure 7.5 Flowchart of the model

7.3.3 Constants and other physical parameters

The constants and parameters used in the model are listed in Table 7-I:

Table 7-I The constants and parameters used in the model

Term	Symbol	Value	Reference
γ′ Solvus temperature	$T_{\gamma'}$	1382.9K	Calculated from Thermo-Calc
Temperature to stop simulation		973.15K	
Atoms in a mole	K	6.023E+23	
Universal gas constant	R	8.3145 J/mol/K	
Initial diffusivity =	D_0	0.001 m^2/s	[13]
Activation energy for coarsening	Q	283KJ/m^2	Estimated from [41]
Interface energy	σ	0.022 J/m^2	[41]
Initial nuclei size		5nm	[43]
Lattice parameter of γ′ phase	$a_{\gamma'}$	3.57 A°	Calculated from PHACOMP software.
Atoms in a cell		4	Face-center crystal
Simulation domain	V	0.1 μm^3	Regulated to limit the total number of the γ′ precipitates.
γ’ volume	$V_{\gamma'}$	$\sum (4 * \pi * r(i)^3/3)$	

7.4 Composition and Gibbs energy at equilibrium

Equilibrium calculation is performed by Thermo-Calc. The alloy contains metallic elements such as major γ′ forming elements Al, Ti, Nb, and matrix forming elements Co, Cr, W, Mo, Ni, Zr, as well as carbide and boride former B and C. The phase transformation in the alloy is very complicated if all the elements are included in the equilibrium calculation. Therefore, we decide to exclude C and B from the equilibrium calculation for this specific purpose to avoid numerical instability in our non-equilibrium simulation. This is not expected to introduce any significant difference to the γ’ characteristics in the overall temperature range we considered because the precipitation

of carbides and boride impacts strongly on the γ–matrix and γ' composition at a narrow temperature range and the lower temperature.

Figure 7.6 to 7.10 are the composition of γ' phase and γ-matrix, Gibbs energy and the volume fraction of the γ' precipitates at the state of equilibrium obtained by the Thermo-Calc calculation.

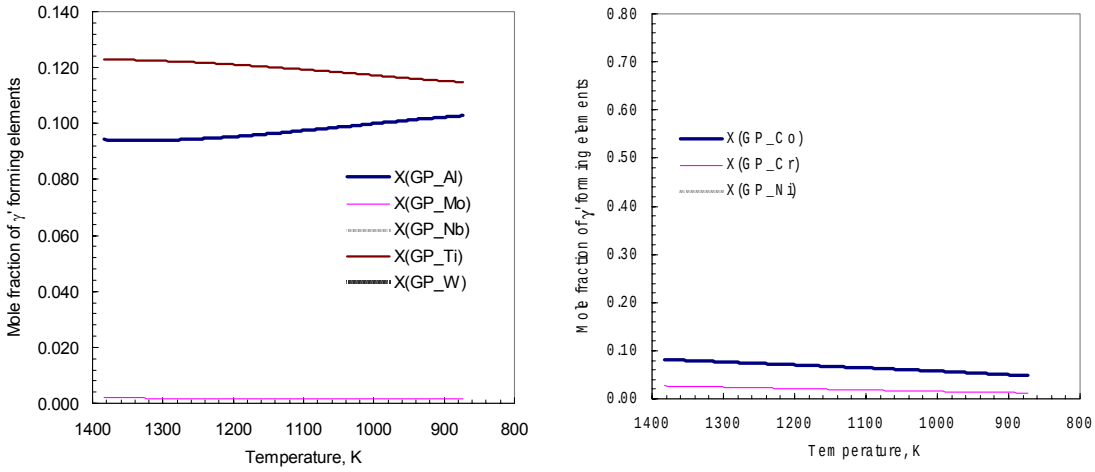

Figure 7.6 γ′ forming elements as a function of temperature

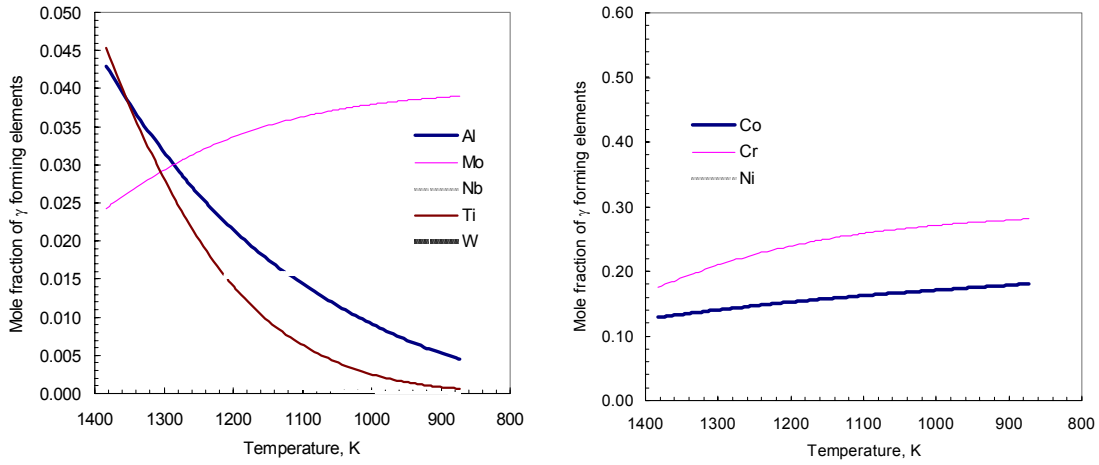

Figure 7.7 γ-forming elements Al, Ti, Mo W and Nb as a function of temperature

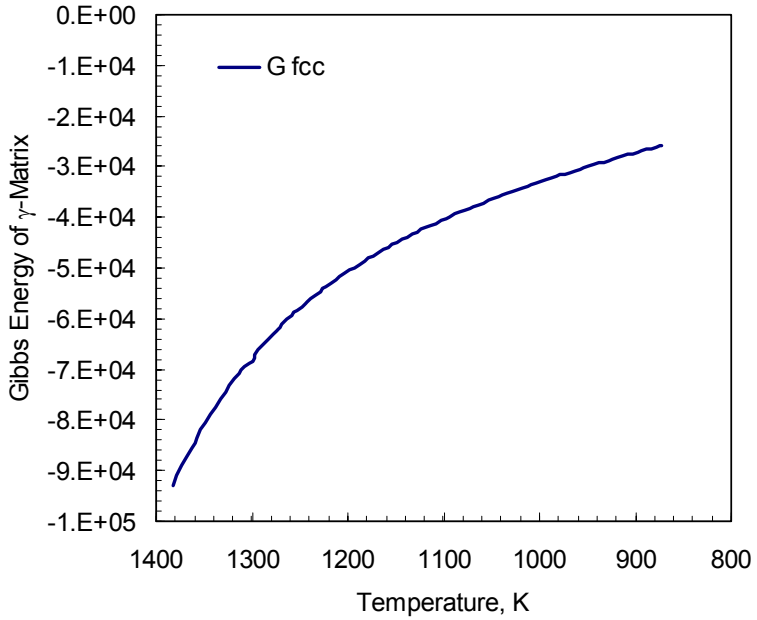

Figure 7.8 Gibbs energy of γ-matrix as a function of temperature

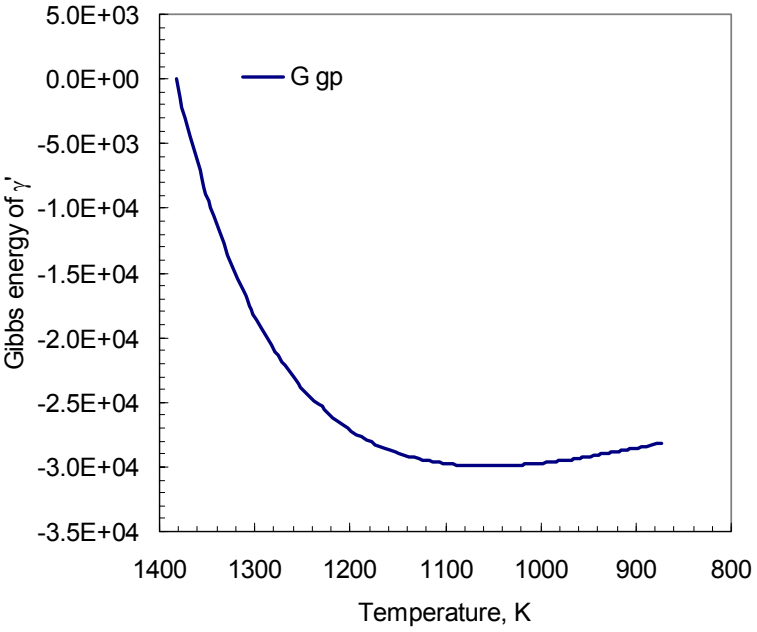

Figure 7.9 Gibbs energy of γ' phase as a function of temperature

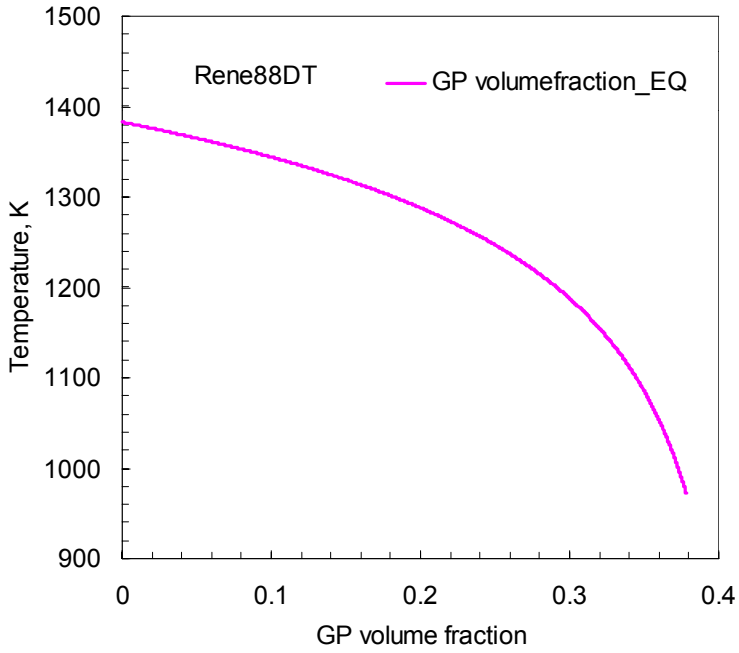

Figure 7.10 The volume fraction of γ′ precipitates as a function of temperature

The regression of the composition, Gibbs energy and the γ' volume fraction used six-order polynomial functions to give enough precision for the numerical stability during non-equilibrium calculation. The equations take the form:

$$y_i^{\gamma'} = aT^6 + bT^5 + cT^4 + dT^3 + eT^2 + fT + g \qquad 7\text{-}11$$

i represents the elements, Al, Ti, Co, Cr, W, Nb, Mo, Zr and Ni, respectively. The coefficients for each element or phase are summarized in Table 7-II through Table 7-V:

Table 7-II Coefficients of the mole fraction function for γ′ forming elements

	a	b	c	d	e	f	g
Ni	*7.06805774E-19*	*- 4.54808113E-15*	*1.20976546E-11*	*- 1.70760672E-08*	*0.0000135227544*	*- 0.00579341662*	*1.78066264*
Ti	*1.912866621E-19*	*- 1.241219453E-15*	*3.356846611E-12*	*- 4.885529421E-09*	*0.000004057795173*	*- 0.001807062861*	*0.4451373485*
Al	*-5.624519588E-20*	*4.08077962E-16*	*- 1.189964731E-12*	*1.88294676E-09*	*- 0.000001753576646*	*0.0008901689172*	*- 0.08147572782*
Co	*1.442116212E-20*	*- 1.91022622E-17*	*- 9.07188937E-14*	*2.744942307E-10*	*- 3.352582846E-07*	*0.000290055521*	*- 0.07648799073*
Cr	*-5.715532708E-19*	*3.614736931E-15*	*- 9.527396205E-12*	*1.339233037E-08*	*- 0.00001056943479*	*0.004452676431*	*- 0.7760230419*
Nb	*-2.359031986E-19*	*1.475156771E-15*	*- 3.8228628E-12*	*5.261097636E-09*	*- 0.000004056133659*	*0.001662564275*	*- 0.2725265621*
W	*-1.263768211E-20*	*8.42325713E-17*	*- 2.315813573E-13*	*3.206953872E-10*	*- 2.106177297E-07*	*0.000030340997*	*0.02587049374*
Mo	*-4.832008733E-20*	*3.04381545E-16*	*- 8.023302116E-13*	*1.13298145E-09*	*- 0.00000090065799*	*0.0003799094664*	*- 0.06452175361*
Zr	1.182306201E-20	- 7.609142664E-17	2.0474028E-13	- 2.949645444E-10	2.387782757E-07	- 0.0001025577424	0.01889672968

Table 7-III Coefficients of the mole fraction function for γ forming elements

	a	b	c	d	e	f	g
Ni	*-3.197371545E-18*	*1.985609044E-14*	*- 5.105593368E-11*	*6.980848239E-08*	*- 0.00005357300367*	*0.02196380062*	*- 3.309564623*
Ti	*-3.110360636E-18*	*1.990500769E-14*	*- 5.262624601E-11*	*7.387107961E-08*	*- 0.00005814356275*	*0.02434140207*	*- 4.234806546*
Al	-1.313840754E-18	8.548774906E-15	- 2.289217986E-11	3.240174124E-08	- 0.00002556559551	0.01067869912	- 1.848450944
Co	*1.905323773E-18*	*- 1.19574152E-14*	*3.107904919E-11*	*- 4.293949261E-08*	*0.00003330042516*	*0.01382309756*	*2.605967774*
Cr	*5.052338528E-18*	*- 3.217012187E-14*	*8.462633051E-11*	*- 1.181687385E-07*	*0.00009245570588*	*0.03847343735*	*6.948936164*
Nb	*-4.508863795E-19*	*2.983668663E-15*	*- 8.141706203E-12*	*1.176256065E-08*	*- 0.000009501716218*	*0.004071760338*	*- 0.7234505615*
W	*3.13253303E-19*	*- 2.03524375E-15*	*5.447710098E-12*	*- 7.711315983E-09*	*0.000006079399825*	*0.00251632919*	*0.4383959652*
Mo	*7.927835072E-19*	*- 5.066366961E-15*	*1.337421582E-11*	*- 1.873811596E-08*	*0.00001470883096*	*0.006137187262*	*1.103736998*
Zr	*8.853067299E-21*	*- 6.499332617E-17*	*1.903684899E-13*	*- 2.884986031E-10*	*2.413606987E-07*	*0.0001063997775*	*0.01937633945*

Table 7-IV The coefficients of the energy functions

	a	*b*	*c*	*d*	*e*	*f*	*g*
G_{mtx}	*-3.451759362E-12*	*2.09666519E-08*	*-0.00005338847581*	*0.0727623174*	*-55.91624866*	*22912.42011*	*-3917987.185*
G_{GP}	*3.439571571E-12*	*-2.089345205E-08*	*0.00005320061458*	*-0.07249723316*	*55.68153256*	*-22851.46055*	*3890707.606*
G_{Sys}	*-1.205426563E-14*	*7.231405188E-11*	*-1.854137317E-07*	*0.0002614833729*	*-0.2317430201*	*59.65448543*	*-27041.52953*

Table 7-V The coefficients of the gamma prime volume fraction

	a	*b*	*c*	*D*	*e*	*f*	*g*
G_{mtx}	*-2.261714326E-17*	*1.356925424E-13*	*-3.419183304E-10*	*0.0727623174*	*-0.0003517672*	*0.1432116357*	*-3917987.185*

The growth and coarsening segments of the non-equilibrium calculation use Al plus Ti as the diffusing elements to assess the size of the γ′ precipitates in their models. Therefore, the summation of Ti and Al is carried out for later use.

$$\gamma\text{' phase :} \quad C_{\gamma'}(T) = y_{Ti}^{\gamma'}(T) + y_{Al}^{\gamma'}(T) \qquad 7\text{-}12$$

$$\gamma\text{-matrix :} \quad C_{\gamma}(T) = y_{Al}^{\gamma}(T) + y_{Ti}^{\gamma}(T) \qquad 7\text{-}13$$

The summations as a function of temperature are plotted in Figure 7.11. In contrast with the γ′ composition, the summation in γ-matrix decreased dramatically with temperature.

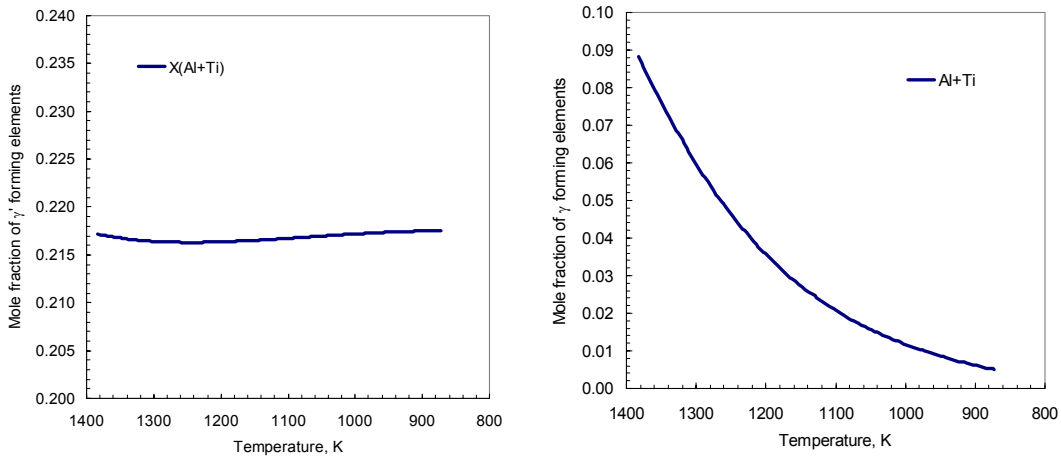

Figure 7.11 The Al+Ti concentration as a function of temperature

7.5 Non-Equilibrium calculation

7.5.1 Non-Equilibrium composition calculation

The growth and coarsening of γ′ precipitates are the diffusion-controlled process. During continuous cooling, rapid cooling limits the full diffusion of the solute elements. Therefore, the composition of the γ-matrix is not able to reach equilibrium composition. For γ′ composition, we have assumed that the composition of γ′ kept as same as that at the state of equilibrium and it is only a function of temperature. Therefore, based on the mass conservation, the mole fraction of the elements in the γ-matrix was calculated as

$$V_f^{\gamma} = 1 - V_f^{\gamma'}$$

$$y_i^{\gamma}(\mathrm{T}) = (y_i^0 - V_f^{\gamma'} * y_i^{\gamma'}(\mathrm{T})) / V_f^{\gamma}, \qquad 7\text{-}14$$

where i represents each element including Ni, Cr, Co, Al, Ti, W, Mo, Nb, and Zr.

y_i^0 -- the composition of the alloy,

$y_i^{\gamma'}$ (T) -- solute elements concentration in γ′, which is described in the previous section.

$V_f^{\gamma'}$ -- the molar fraction of total γ′ precipitates formed

From the calculation of the $y_i^0, y_i^{\gamma'}, V_f^{\gamma'}$, the non-equilibrium y_i^{γ} could be obtained.

7.5.2 Non-equilibrium Gibbs energy calculation

Gibbs energy of a phase is the state function of the temperature and composition under constant pressure. Thermo-Calc provides a great tool to calculate the Gibbs equilibrium for the system of γ-matrix, γ′ phase and the system. However, it only provides the results at the state of equilibrium. A new stand-alone module has to be developed to calculate the Gibbs energy of the γ matrix at the non-equilibrium state, because the composition of γ-matrix no longer remains at its equilibrium. This was accomplished by extracting the data in the nickel-iron database used in the above Thermo-Calc calculation. The database is developed by Nigel Saunders [44].

The Gibbs energy of a solution (γ-matrix in this case) is given as [44]:

$$G_m = G_m^0 + \Delta G_m^{ideal} + \Delta G_m^{xs} \qquad 7\text{-}15$$

where G_m^0 -- the Gibbs energy of pure component

ΔG_m^{ideal} -- Gibbs energy of ideal mixing

ΔG_m^{xs} -- Gibbs energy of a non-ideal mixing, which refers to the interaction between elements.

γ-matrix is a crystal structure with sub-lattices. The main lattice is the metallic elements. The other is the interstitial elements such as B, C, or simply vacancy. The sublattice can be described as:

$(Ni, Cr, Co, W, Mo, Ti, Zr, Al, Nb)_1(B, C, Va)_1$

where Va represents the vacancy. Ni, Cr, Co, W, Mo, Ti, Zr, Al, Nb are the substitutional elements.

In our case, we neglected B and C for simplification. Therefore we have:

$(Ni, Cr, Co, W, Mo, Ti, Zr, Al, Nb)_u(Va)_v$

The composition of the of three Gibbs energy terms in equation 7-16 are given as Saunders' book [44]:

$$G_m^0 = y_{Ni}^1 y_{Va}^2 G_{Ni:Va}^0 + y_{Cr}^1 y_{Va}^2 G_{Cr:Va}^0 + y_{Co}^1 y_{Va}^2 G_{Co:Va}^0 + y_W^1 y_{Va}^2 G_{W:Va}^0 + y_{Mo}^1 y_{Va}^2 G_{Mo:Va}^0 + y_{Ti}^1 y_{Va}^2 G_{Ti:Va}^0 + y_{Zr}^1 y_{Va}^2 G_{Zr:Va}^0 + y_{Al}^1 y_{Va}^2 G_{Al:Va}^0 + y_{Nb}^1 y_{Va}^2 G_{Nb:Va}^0 = \sum_i y_i^1 G_{i:2}^0 \quad 7\text{-}16$$

$$\Delta G_m^{ideal} = RT(u \cdot (y_{Ni}^1 \cdot \log_e y_{Ni}^1 + y_{Cr}^1 \cdot \log_e y_{Cr}^1 + y_{Co}^1 \cdot \log_e y_{Co}^1 + y_W^1 \cdot \log_e y_W^1 + y_{Mo}^1 \cdot \log_e y_{Mo}^1 + y_{Ti}^1 \cdot \log_e y_{Ti}^1 + y_{Zr}^1 \cdot \log_e y_{Zr}^1 + y_{Al}^1 \cdot \log_e y_{Al}^1 + y_{Nb}^1 \cdot \log_e y_{Nb}^1) + v(y_{Va}^1 \cdot \log_e y_{Va}^1)) = RTu \sum_i y_i^1 \log_e y_{Va}^2 \quad 7\text{-}17$$

$$\Delta G_m^{xs} = y_{Ni}^1 \cdot y_{Cr}^1 \cdot y_{Va}^2 \left[\sum_v L_{Ni,Cr:Va}^v (y_{Ni}^1 - y_{Cr}^1)^v \right] + y_{Ni}^1 \cdot y_{Co}^1 \cdot y_{Va}^2 \left[\sum_v L_{Ni,Co:Va}^v (y_{Ni}^1 - y_{Co}^1)^v \right] + y_{Cr}^1 \cdot y_{Co}^1 \cdot y_{Va}^2 \left[\sum_v L_{Cr,Co:Va}^v (y_{Cr}^1 - y_{Co}^1)^u \right] + \ldots + y_{Al}^1 \cdot y_{Nb}^1 \cdot y_{Va}^2 \left[\sum_v L_{Al,Nb:Va}^v (y_{Al}^1 - y_{Nb}^1)^u \right] + y_{Ni}^1 \cdot y_{Cr}^1 \cdot y_{Co}^1 \cdot y_{Va}^2 \left[\sum_v L_{Ni,Cr,Co:Va}^v (y_{Ni}^1 - y_{Cr}^1 - y_{Co}^1)^v \right] + \ldots = \sum_v (y_i^1 \cdot y_j^1 \cdot y_{Va}^2 (\sum_v L_{i,j:Va}^v (y_i^1 - y_j^1)^v)) + \sum_v (y_i^1 \cdot y_j^1 \cdot y_k^1 \cdot y_{Va}^2 (\sum L_{i,j,k:Va}^v (y_i^1 - y_j^1 - y_k^1)^v)) \quad 7\text{-}18$$

ΔG_m^{xs} is the sum of all the two-element interactions and all the three-element interactions.

In the above equations y is the number of occupancy in the crystal lattice, here is the mole fraction of the γ-matrix forming elements (see the previous section), and i, j, k represent the elements Ni, Cr, Co, W, Mo, Ti, Zr, Al, Nb. Upcase 1 represents the substitution elements, and upcase 2 represents the vacancy.

$G^0_{i:2}$ is the Gibbs energy of each pure element, which is a function of temperature. To be more specific, they are $G_{Al:0}(T)$, $G_{Co:0}(T)$, $G_{Cr:0}(T)$, $G_{Fe:0}(T)$, $G_{Mo:0}(T)$, $G_{Nb:0}(T)$, $G_{Ni:0}(T)$, $G_{Ti:0}(T)$, $G_{W:0}(T)$, $G_{Zr:0}(T)$. The functions can be found in the Ni-Fe database.

$L^v_{Ni,Cr:Va}$ and $L^v_{Ni,Cr,Co:Va}$ are the Gibbs energy of any two elements and any three elements interaction, respectively, which were also obtained from the Ni-Fe database by Saunders [44].

With the matrix Gibbs energy and the assumption that the γ′ still retains its equilibrium composition and energy, the non-equilibrium system energy, G_{sys}, can be calculated by the equation in section 7.3.1.

7.5.3 Energy barrier for nucleation

The direct estimation of energy barrier is very difficult in reality. This basic energy involved is the Gibbs free energy of the γ-matrix and the γ′ precipitates, which can be precisely determined by the above approach. However, other energy terms concerning lattice are less well defined, such as the lattice mismatch, elasticity at that high temperature and the applicability of classic elasticity theory. But we believe that we may be able to find direct experimental approach to derive the energy we need for the calculation.

According to David Furrer's research on U720LI growth kinetics, the burst of the precipitates takes place under a certain undercooling. Figure 7.12 shows the cooling profile recorded during the quenching. In the chart, the bumps in the curve indicate the burst of the precipitation. The undercooling corresponding to the bump varies with the

cooling rate, as shown in Figure 7.13. This phenomenon was also confirmed by our test results of Rene88DT[38].

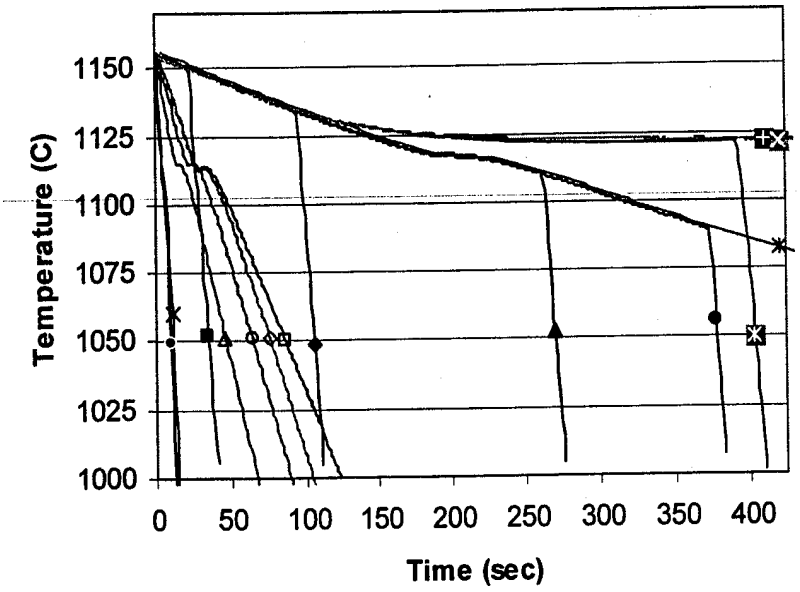

Figure 7.12 Cooling curves from solvus to 1000°C of U720LI[26, 27]

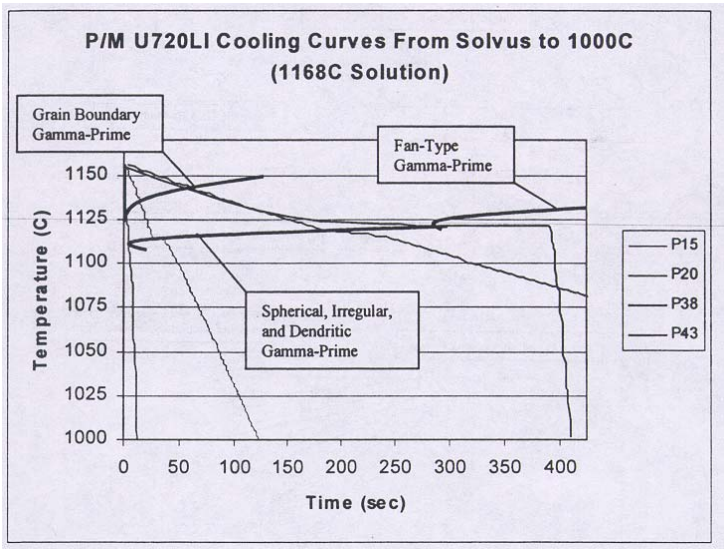

Figure 7.13 The undercooling varies with the cooling rate in U720LI[26, 27]

For Rene88DT, the effect of cooling rate on the undercooling was conducted. Figure 7.14 shows the DTA results of the maximum precipitation temperature versus cooling rate. The maximum precipitation temperature, T_{max}, is defined as the temperature, at which precipitation rate reaches to its maximum.

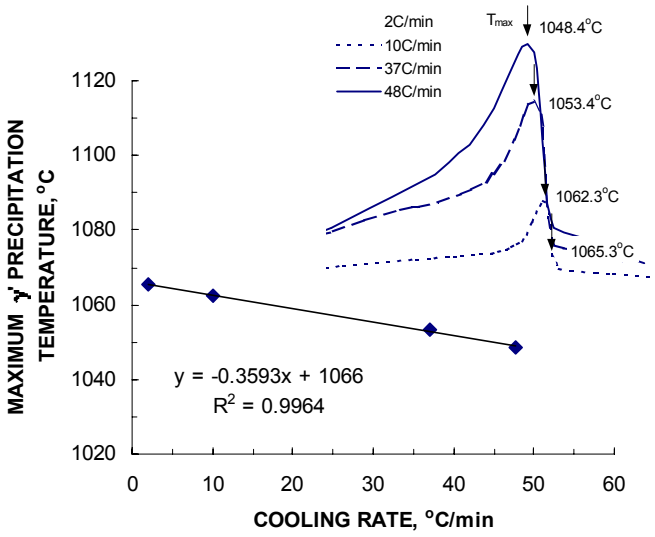

Figure 7.14 Variation of the maximum precipitation temperature with cooling rate

Relationship between the T_{max} and cooling rate is described as:

$$T_{max} = -0.3593*(dT/dt) + 1066 \qquad 7\text{-}19$$

Where T_{max} is in K and dT/dt is in °C/min.

The above undercooling actual reflects the effect of the energy barrier. If we take into consideration of the relationship of the undercooling and the cooling rate, we actually introduced the kinetic influence mentioned in the theory part. This is what we expected to see. To determine the energy barrier, we should consider both thermodynamic and kinetic effects. First, from thermodynamic point of view, the excess energy is calculated as a function of temperature before the γ' nucleation when the energy barrier is set very high, as shown in Figure 7.15. By combining Figure 7-19 with the kinetics effect of equation 7-19, the excess energy as a function of the cooling rate was obtained, which was then considered as the energy barrier, EnergyBarrier (EB). Physically, the energy barrier

should be a function of temperature. In order to simplify the computer program, the energy barrier is considered as a constant responding to temperature and only varied with the cooling rate, which is given in Equation 7-20 and plugged in Figure 7.15:

$$\text{EnergyBarrier} = 3.0888(dT/dt)^2 + 18.25(dT/dt) + 18.569 \qquad 7\text{-}20$$

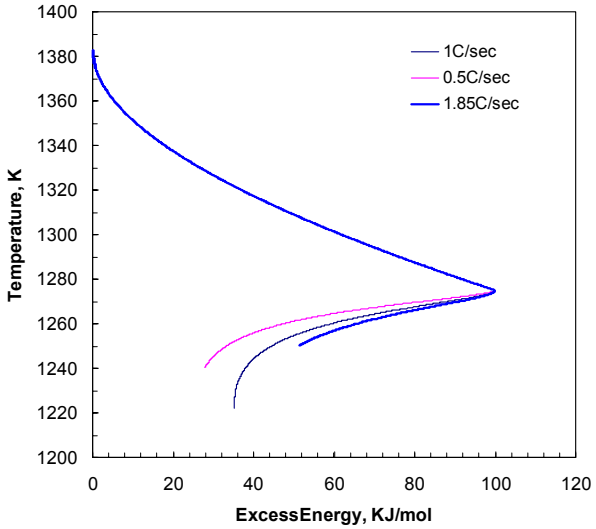

Figure 7.15 ExcessEnergy as a function of temperature in Rene88DT

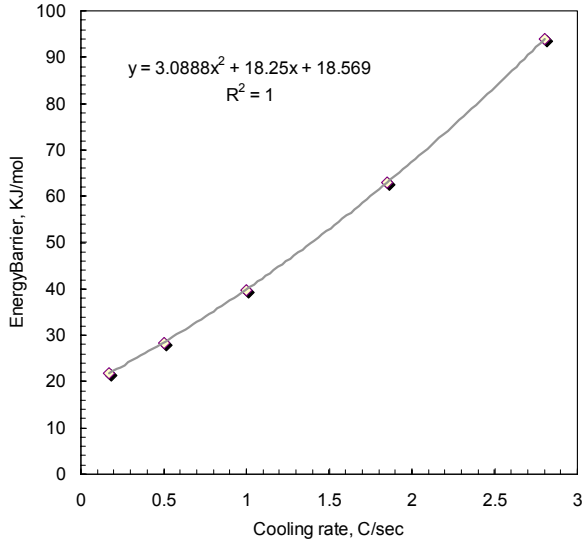

Figure 7.16 EnergyBarrier versus cooling rate in Rene88DT

7.6 Simulation result and Validation

With the energy-driven model, γ′ precipitation simulation during continuous cooling was performed at different cooling rates, 6°C/min, 30°C/min, 56°C/min, and 168°C/min. From the simulation, following outputs were obtained: the γ′ precipitate radius, γ′ precipitate size distribution, number of particles, volume fraction of γ′ precipitates, the excess energy and the supersaturation of the system during the cooling. The simulation result was then compared with the experimental data.

7.6.1 Excess energy and supersaturation simulation

Figure 7.17 and 7.18 show the ExcessEnergy and supersaturation variation with the decreasing temperature during continuous cooling at the cooling rate of 167°C/min, respectively. As the temperature decreased, the supersaturation started to build up, while the Gibbs energy of the system increased, e.g. excess energy increased. As the excess energy exceeded the energy barrier, the nucleation occurred. After that, the supersaturation and the excess energy dropped dramatically and continued to drop while the γ′ particles grew. As the excess energy reached to minimum, the growth of the γ′ particle was ceased, the particles started to coarsen. As the temperature decreased further, the supersaturation regained and the excess energy of the system accumulated again, as seen the second bump in Figure 7.17, 7.18. Once it exceeded the energy barrier at the certain temperature, then the secondary burst of the γ′ precipitates occurred, which caused the average size decreased dramatically (see in Figure 7.19).

Unlike the first burst, the diffusion-driven growth of the secondary burst γ′ precipitates is limited at the lower temperature due to continuous cooling. Therefore, the secondary burst γ′ is much smaller than the first ones. In additional, the secondary burst γ′ did not cause any significant decrease of the excess energy and supersaturation due to the limited growth. It should be pointed out that in reality, the energy barrier for the second burst should differ from the first one. However, we took a simplified approach to use the same energy barrier.

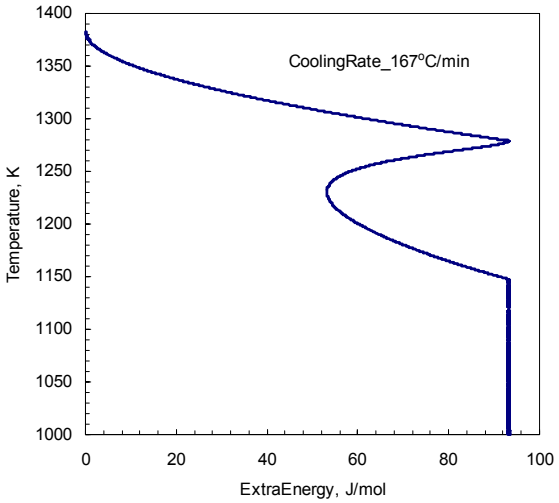

Figure 7.17 ExcessEnergy vs decreasing temperature @Cooling rate 167°C/min

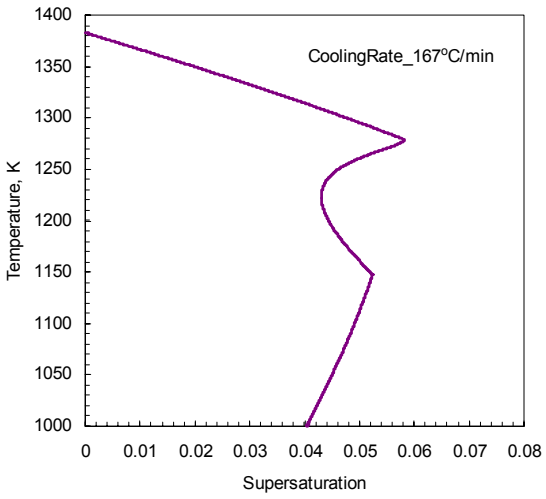

Figure 7.18 Supersaturation vs decreasing temperature @ Cooling rate 6°C/min

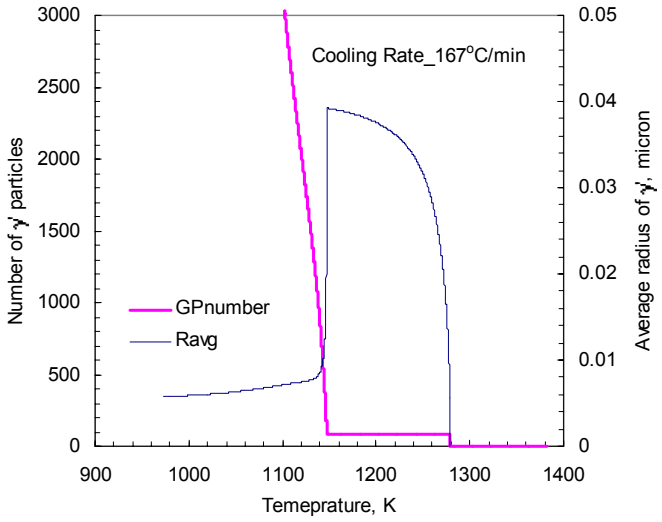

Figure 7.19 Average radius and the number of particles vs decreasing temperature @Cooling rate 6°C/min

The Multi-stage nucleation shows more significant at the lower cooling rate. Figure 7.20 and 7.21 show the excess energy and supersaturation varied with the decreasing temperature during continuous cooling at the cooling rate of 6°C/min. It was found that there are two drops in the ExcessEnergy and supersaturation curves. The third turn of

energy accumulation is accountable for the enough growth and coarsening of the secondary burst of γ′ precipitates at the lower cooling rate case, as seen in Figure 7.22. The size of the third burst of the γ′ precipitates is even smaller than the secondary burst ones and then resulted in the average radius obvious dropped again.

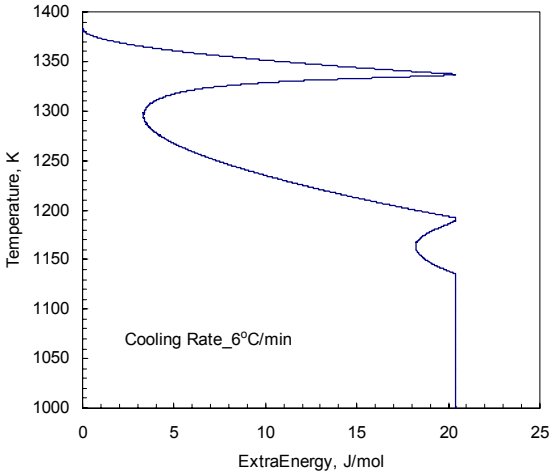

Figure 7.20 ExcessEnergy vs decreasing temperature @Cooling rate 6°C/min

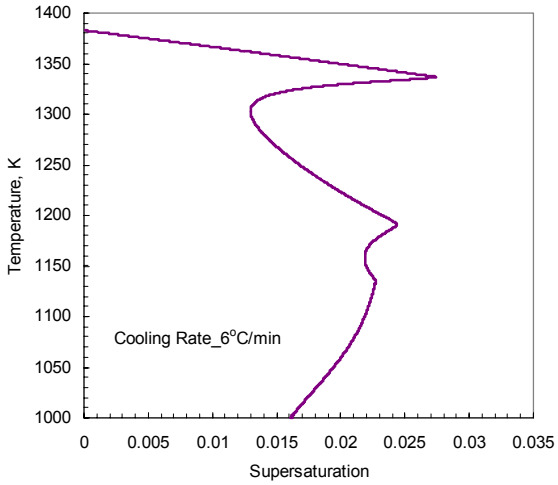

Figure 7.21 Supersaturation vs decreasing temperature @ Cooling rate 6°C/min

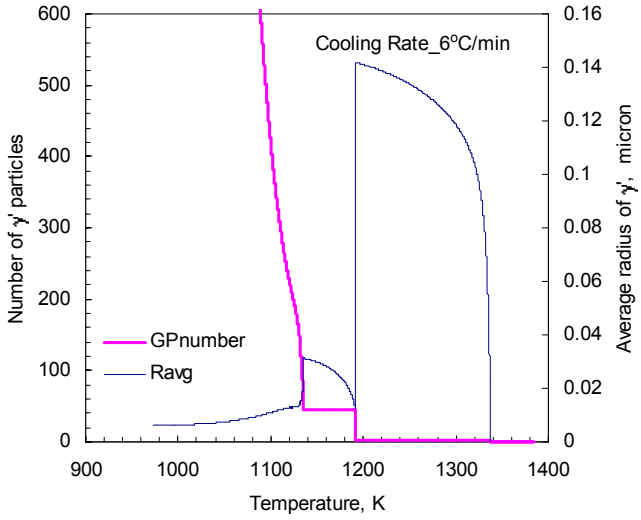

Figure 7.22 Average radius and the number of particles vs decreasing temperature @ Cooling rate 6°C/min

7.6.2 Cooling γ' precipitates versus cooling rate

The effect of cooling rate on the cooling γ' precipitation was simulated and the results were validated by the experimental data. Figure 7.23 shows the mean diameter of the γ′ precipitates varied with the cooling rate. In the chart, the up solid line represents the simulated the average diameter of the first burst of γ′ precipitates after cooling from γ′ solvus to 973K and the square marks are the experimental data. As we see, the simulation result shows good consistent with experimental results, especially at the lower cooling rate case. And the relationship between the size of the first burst γ′ precipitates and cooling rate also obeys a power law:

$$D\gamma' = 0.5764\ (dT/dt)^{-0.39} \qquad 7\text{-}21$$

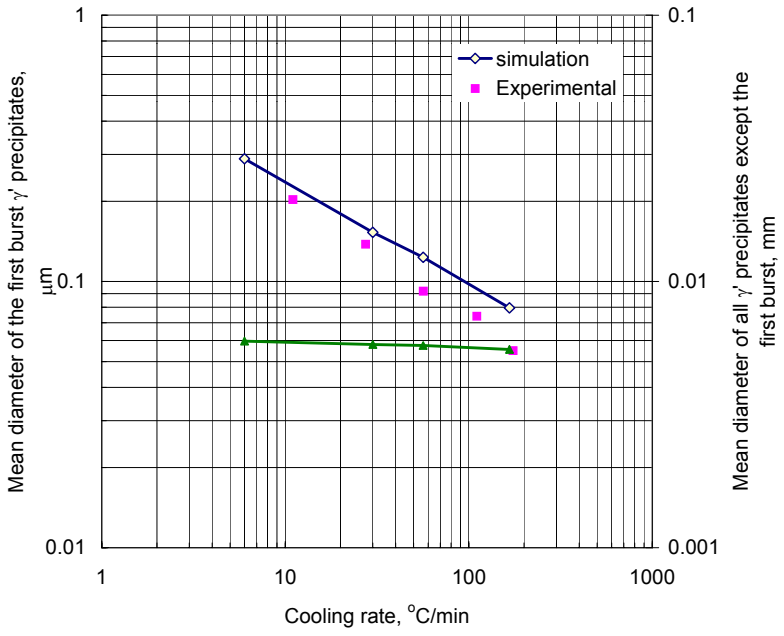

Figure 7.23 The mean diameter of the γ' precipitates as a function of cooling rate

The size of the secondary burst γ′ precipitates was also obtained from the simulation. The relationship between the secondary γ′ precipitates and cooling rate was also plotted in Figure 7.23. As we see, the secondary burst γ′ precipitates size did not show significant dependence on the cooling rate although the higher cooling rate results in a litter bit

smaller the size of the secondary burst γ′ precipitates. Note that the average size of the secondary burst of the γ′ precipitates counted is the all γ′ precipitates except the first burst ones in the chart 7.23.

The volume fraction of the γ′ precipitates varied with cooling rate was plotted at the Figure 7.24. It is noted that the volume fraction of the γ′ precipitates decreased with the increase in cooling rate and results also shown good consistence with the experimental data.

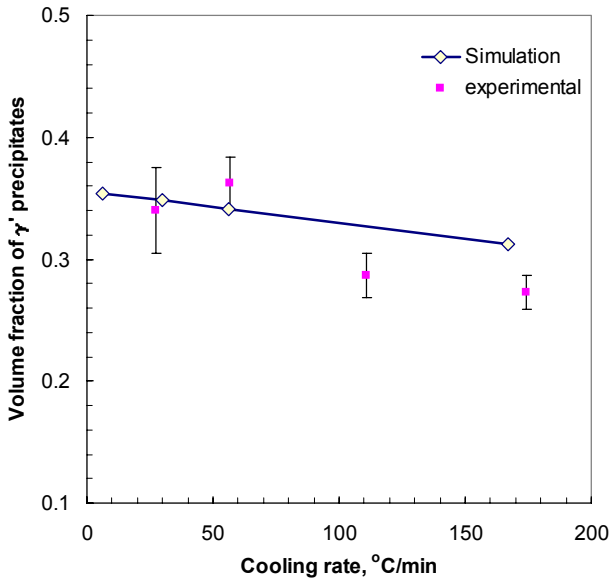

Figure 7.24 The volume fraction of the first burst γ' precipitates varies with cooling rate

The number of γ′ particles both of the first and the secondary burst varied with the cooling rate can also be obtained through the computer simulation. The number of the first burst γ′ precipitates shows a linear proportional relationship with the cooling rate, but the number secondary burst γ′ precipitates shown the exponential function of the cooling rate, as shown in Figure 7.25. In addition, the higher the cooling rate, the more the first burst γ′ precipitates with smaller size, and the more secondary burst γ′ precipitates. Therefore, the higher the cooling rate, the more strengthening is resulted in due to the more secondary and tertiary γ′ precipitates generated.

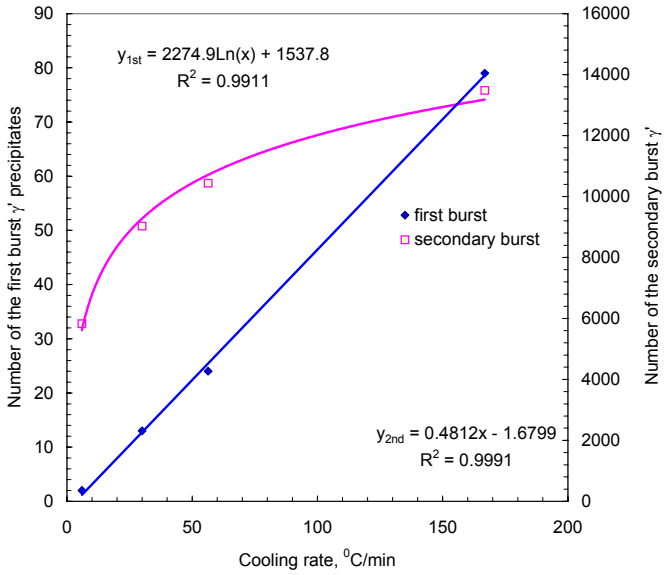

Figure 7.25 The number of the γ′ precipitates

Of interesting is the slope of the number of particles versus cooling rate which is very similar to the slope of the particle density versus cooling rate obtained from experimental, being 0.5416 in equation 3-3.

7.6.3 The γ' precipitate size distribution versus cooling rate

The size distribution of the γ′ precipitates could also be simulated using the model. In figure 7.26, the frequency represents the number of the γ′ particles with the size at a bin range. It was shown that the size distribution is not like what we saw in experimental work. For the first burst γ′ precipitates, all the particles have almost the same size, which proved the burst terminology, e.g. the precipitation happens promptly.

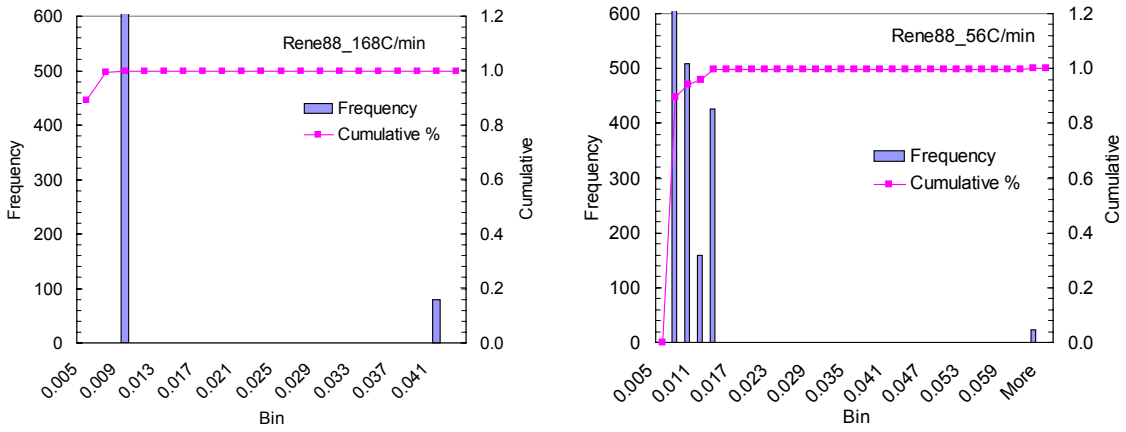

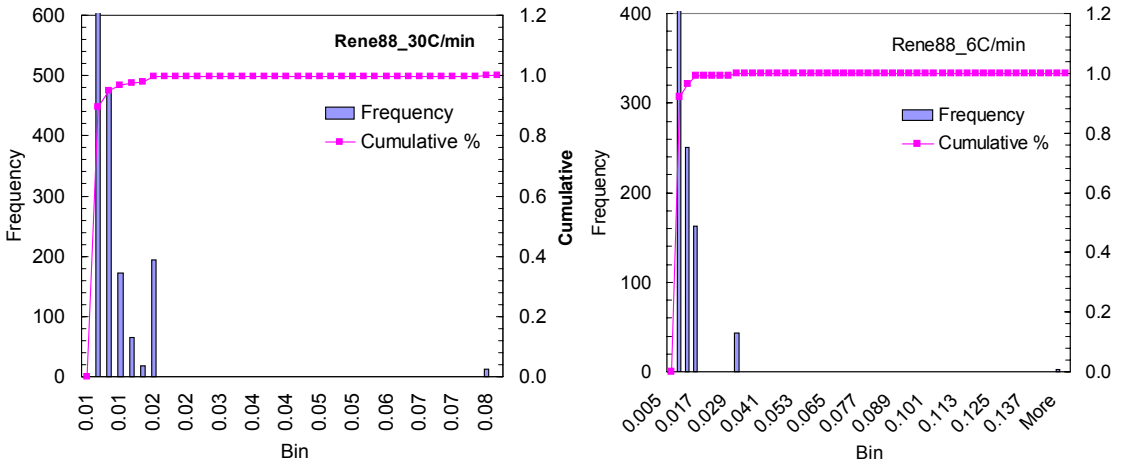

Figure 7.26 The size distribution of the γ' precipitates at different cooling rate

Unlike the first burst, the secondary burst or third burst of γ′ precipitates continue occur with the decrease of the temperature, which caused the average size keep decreasing and the number of γ′ precipitates keep increasing with the cooling proceeds. Therefore, the size distribution more or less shows the normal distribution as cooling rate decreases, as shown in Figure 7-19, 7-22 and 7-26.

7.6.4 Cooling γ' precipitates versus temperature

The development of γ′ precipitates during the cooling process was studied experimentally by the interrupt cooling. The simulation result was also presented in Figure 7.27. In the chart, only first burst of γ′ precipitates were included. The good consistence with the experimental results was shown again.

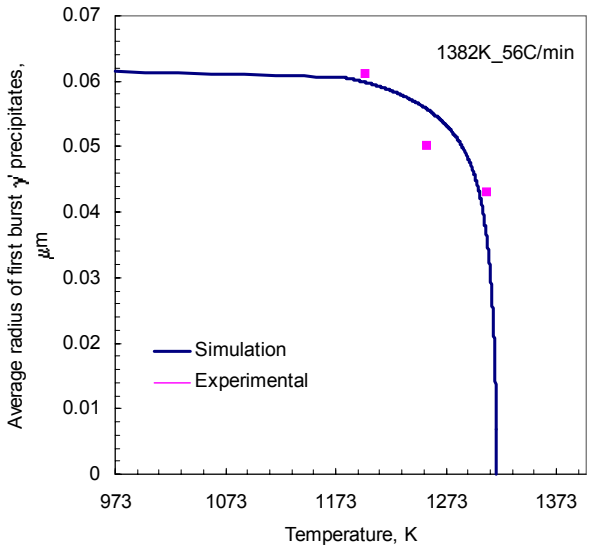

Figure 7.27 The mean radius of the first burst γ' precipitates varies with temperature

The γ' precipitates development at the different cooling rate was shown in Figure 7.28. As we see, the higher cooling rate, the more undercooling, and the smaller γ′ precipitates are. The drops in the curves represent that there is new turn of γ′ precipitates occurred with much smaller size, which causes the average radius decrease dramatically. The multi-stage precipitation was demonstrated as the cooling rate decreases, as seen in the case of cooling rate lower than 30°C/min.

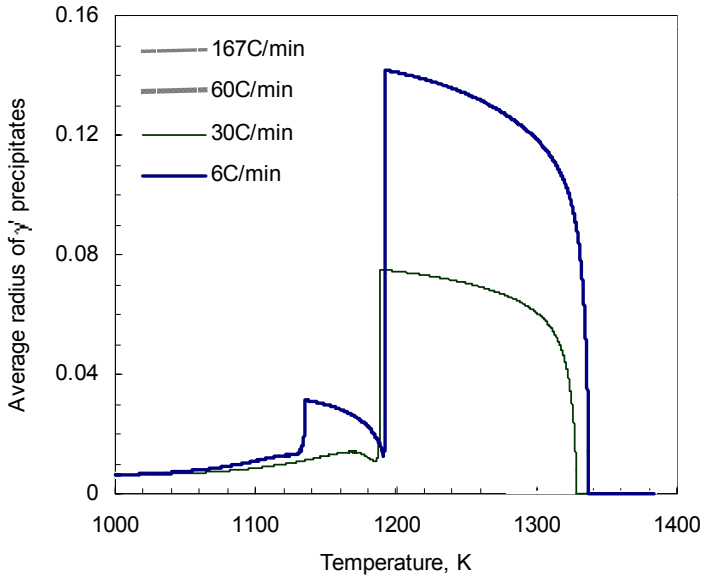

Figure 7.28 The γ′ precipitates growth versus cooling rate

7.7 Discussion

As we studied in the continuous cooling, the double nucleation was found in U720LI, but didn't see evidence in Rene88DT. However the study of tensile strength against decreasing temperature in Chapter 5, we did found the non-monotonic decrease of the tensile strength in both alloys. At the time, we suggested that must have very fine γ′ precipitates nucleation that cause the regaining of the decreasing strength. From the above simulation, we are cleared that the secondary burst of the γ′ precipitates does happens regardless the cooling rate. Those tiny γ′ precipitates are accountable for the strength regained.

The burst theory was validated from 7.19, 7.22 and 7.26. The γ′ precipitates nucleate at a very short period. The last period varies with the cooling rate. Figure 7.29 shows the number of the γ′ nucleated increases as the temperature decreases at the cooling rate of 167°C/min. The last period will be even shorter when the cooling rate is slower.

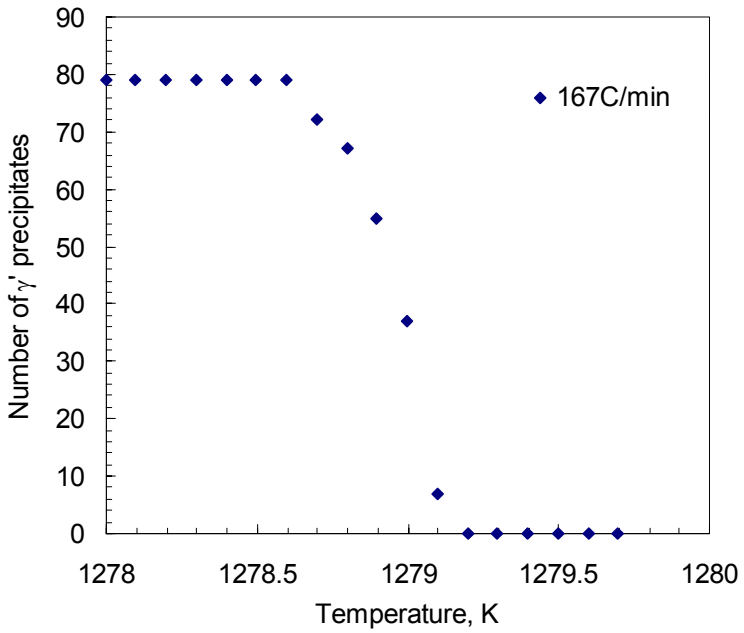

Figure 7.29 The number of the γ′ nucleated varies with the temperature

In chapter 3, we also discussed the multi-stage γ′ formation mechanism as shown in Figure 3.15. The higher cooling rate results in more undercooling, and then more supersaturation build up. As a result, the more first burst of γ′ with smaller size and smaller inter-spacing between the particles will formed. This was verified by the simulation results shown in Figure 7.23, 7.25 and 7.28. In contrast, lower cooling rate will provide possibility to supersaturate the area between the first burst γ′ precipitates and to stimulate the secondary burst of γ′ precipitates.

In the Figure 7.28, it is noted that after γ′ development passes the sharp curved part, the slopes of the line almost the same for all cooling cases, which is considered to be dominated by coarsening process. Before that point, it is growth dominated. Therefore, the cooling rate strongly influences the early stage of the γ′ development including nucleation stimulation and the long distance diffusion-controlled growth of the γ′ precipitates.

Of interesting is that the development of the γ′ precipitates follows a power low with having exponential of 2.56, which is between 2 of the growth law in equation 7-4 and 3 of the coarsening law in equation 7-6. The power law with having an exponential of 2.56 can be derived from the equation 7-21, i.e.:

$D\gamma' = 0.5764\ (dT/dt)^{-0.39}$

If dT is fixed at a temperature step, then

$D_{\gamma'} = k(\Delta t)^{0.39}$

i.e. $R^{2.56} = K\Delta t$

Which means that the γ′ overall precipitation is controlled by both growth and coarsening processes as long as the nucleation is simulated.

7.8 Summary

The energy-driving model is developed based on the first principle thermodynamic law. Three basic processes: nucleation, diffusion-controlled growth and coarsening, were integrated into one model. The model utilizes the thermodynamic data output from

Thermo-Calc and the nickel database, and used it to develop Gibbs energy and composition calculation in γ-matrix and γ′ phase at the state of equilibrium and non-equilibrium condition. An excess energy was introduced to serves as criteria to control the processes. The thermodynamic and kinetic approaches were combined to determine the energy barriers in the model. A program was developed in Excel to simulate the γ′ precipitation. Some key conclusions were made:

1) The energy-driven model was successfully embedded in a computer program to simulate γ′ precipitation during continuous cooling. The combination of the thermodynamic and the kinetic approaches provided a practical method to determine the critical nucleation energy.

2) The classic diffusion-controlled growth and Ostwald ripening coarsen theories were integrated with the energy-controlled nucleation process. And the dissolving of the smaller particle during coarsening was also taken into accounted. The whole precipitation process was under the control of the exceed energy in the system. The general approach was proved to be successful.

3) By utilizing the thermodynamic data and model in Thermo-Calc and nickel data base, and combining with the mass conservation, the program was able to calculate the Gibbs energy and the composition either in γ-matrix or γ′ phase both at the state of equilibrium and non-equilibrium, as well as the supersaturation in the matrix.

4) The simulation results verified the burst theory and the existences of the multi-stage burst of γ′ precipitates in a various aspects, and show good agreement with the experimental data both in continuous cooling and interrupt cooling. And it solved the puzzle of the non-monotonic decrease in tensile strength during interrupt cooling.

5) The simulation results depict the effect of the cooling rate on the mechanism of the multi-stage nucleation. It was also concluded that the γ′ precipitation is mainly

dominated by the growth even though the nucleation and coarsening also play an important role.

6) The model treated every particle as an individual. As a result, the program was able to present the average size, the volume fraction, the number of precipitates and the size distribution both of the first burst and the second burst of γ' precipitates.

Conclusion

1) The fully computer-controlled quenching system equipped with an infrared high power quartz heater allowed accurate simulation and control of any desired cooling profile. Two novel cooling methods: one is continuous cooling at fixed cooling rate and the other is interrupt cooling, were conducted in the system. Modified DTA furnace enables the isothermal aging tests.

2) The growth and coarsening kinetics of the cooling γ′ precipitates were experimentally studied under different cooling and aging conditions, and the empirical equations to describe the relationships between the size of the cooling γ′ precipitates and the cooling rate, decreasing temperature during the cooling, and the aging time were established. It was found that the cooling γ′ precipitate versus the cooling rate follows a power law with an exponential being about 0.47 for Rene88DT and 0.35 for U720LI. The cooling γ′ precipitate size versus aging time obeys the LSW cube law for coarsening.

3) The strengthening of the material responses to the cooling rate and the decreasing temperature during cooling was investigated in both alloys as well. The tensile strength increases with the cooling rate. The strength responding to interrupt temperature shows a non-monotonic decrease, which was interpreted as the result of the multi-stage γ′ precipitation.

4) An energy-driven model integrated with the classic diffusion-controlled growth and Ostwald ripening coarsen theories was successfully embedded in the developed computer program to simulate the cooling γ′ precipitation, which is based on the first principle of thermodynamics. The combination of the thermodynamic and the kinetic approaches provided a practical method to determine the critical nucleation energy.

5) By utilizing the thermodynamic data and model in Thermo-Calc and nickel data base, and combining with the mass conservation, the program could calculate the Gibbs energy and the composition either in γ-matrix or γ′ phase both at the state of equilibrium and non-equilibrium, as well as the supersaturation in the matrix.

6) The simulation results proved the γ′ burst theory and the existence of the multi-stage burst of γ′ precipitates, which was experienced during the experimental study, based on the result of the size distribution, excess energy and supersaturation change during the cooling, and the average size varies with the temperature. The results also depict the effect of the cooling rate on the mechanism of the multi-stage nucleation.

7) The simulation results show good agreement with the experimental data in a variety of aspects, such as average size versus cooling rate, average size versus temperature, volume fraction versus cooling rate and particle density versus cooling rate.

8) The simulation results concluded that the γ′ precipitation is mainly dominated by the growth even though the nucleation and coarsening also play an important role.

Reference

[1] Chester T. Sims, William C.Hegel, Superalloys, ISBN 0-471-79207-1, 1972, John Wiley&Sons, Inc.

[2] K.M.Chang, M.F. Henry and M.C. Benz, Metallurgical control of fatigue crack propagation in superalloys, JOM, December, 1990, p29-35

[3] S.T.Wlodek, M.Kelly and D.A.Alden, The structure of Rene88DT, Superalloy 1996, R.D.Kissinger, D.J.Deye, D.L.Anton, et al., eds., pp.129-136

[4] N. Gayraud, F.Moret, X.Baillin, P.E.Mosser, Precipitation kinetics in N18 P/M superalloy: experimental study and numerical modeling, Journal de Physique III, volume 3, Nov. 1993, pp271-276

[5] M.Chang, A.K.Koul and C.Cooper, Damage Tolerance of P/M Turbine disk materials, Superalloy 1996, p677-685

[6] Hiroshi hattori, Mitsuhiro Takekawa, David Furrer, et al, Evaluation of P/M U720 for gas turbine engine disk application, Superalloy, 1996, 705-711

[7] David U.Furrer, Microstructure and mechanical property development in alloy U720LI, Ph.D Dissertation, Universitat Ulm, Germany, 1999

[8] R.A.Wallis and P.R.Bhowal, Property optimization in superalloys through the use of heat treat process modeling, Superalloys 1988, p525-534

[9] R.A.Wallis, Modeling quenching-the state of the art, Advanced materials & processes, Sept.1995, p42kk-42NN

[10] Jian Mao, Keh-Minn Chang, David U.Furrer, Quench Cracking Characterization of Superalloys Using fracture Mechanics Approach, Superalloy 2000, Proceeding of 9th international symposium on superalloys, Sept.2000, Sevenspring, PA.

[11] Jian Mao, V.L.Keefer, Keh-Minn Chang, and David Furrer, An investigation on quench cracking behavior of superalloy Udimet 720LI using a fracture mechanics approach, Journal of Materials Engineering and Performance, Vol.9, No.2, 2000, p204-214

[12] Dwaine L. Klarstrom, Heat treat cracking of superalloys, Advanced Materials & Processes, April, 1996

[13] Timothy P.Gabb, Daniel G. Backman, Daniel Y.Wei et al, r' formation in a Nickel-base disk superalloy, Superalloy 2000.

[14] Jian mao, KelanYu and Ruifa Zhou, The study of γ' precipitation during heat treatment in HIP+forged Rene'95 alloy, Aeronautical Materials (in Chinese), Vol.9, No. 4, 1989, p1-9

[15] Charles E. Bates, George E. Totten, Quantifying quench-oil cooling characteristics, Advanced materials and processes, March, 1991, p25-28

[16] C.A.Klepser, Effect of continuous cooling rate on the precipitation of gamma prime in Nickel-based superalloys, Scripta Metallurgica et Materialia, Vol.33, No.4, pp.589-596

[17] Yongling Yu, Physical Metallurgy (in Chinese), Metallurgical Industry publication Co., Beijing, 1999

[18] H.Wendt and P Hassen, Nucleation and growth of γ'-precipitates in Ni-14at%Al, Acta Metall. Vol.31, No.10, pp.1649-1659, 1983

[19] I.M.Lifshizs and V.V.Slyozov, J.Phys. Chem. Solids 19, 35(1961).

[20] C.Wagner, Z.Elektrochemie 65, 581 (1961)

[21] V. Vaithyanathan and L.Q.Chen, Scripta mater. 42(2000) 967-973

[22] V. Vaithyanathan and L.Q.Chen, Mat. Res.Soc.Symp.Proc., Vol.580, Nov. 29-Dec.1, 1999, Materials Research Sociaty, pp327-332

[23] N. Gayraud, F.Moret, X.Baillin, P.E.Mosser, Kinetics of γ' precipitation in N18 P/M Superalloy, Euromat Conference: Materials development in Rail, tire, wing, hull transpotation, Genes, 22-24 Sept.1992, pp1225-1233

[24] R.A>MacKAY and M.V.Nathal, Acta metall. Mater. Vol.38, No.6, pp993-1005, 1990

[25] M.P.Jackson and R.C.Reed, Heat treatment of udimet720Li: the effect of microstructure on properties, Materials science and engineering, A259, 1999, p85-97

[26] David Ulrich Furrer, γ' formation in Superalloy U720LI, Scripta Materialia, Vol.40, No.11, 1999,pp.1215-1220

[27] Dave U. Furrer, Doctorate of Engineering Dissertation, University UIM, UIM German, 1999

[28] S.T.Wlodek, M.Kelly and D.Alden, The structure of N18, Superalloy 1996, R.D.Kissinger, D.J.Deye, D.L.Anton, et al., eds., pp467-476

[29] P.R.Bhowal, E.F.Wright, and E.L.Raymond, Effects of cooling rate and γ' morphology on creep and stress-rupture properties of a PM Superalloy, Metallurgy transactions A, Volume 21A, June 1990, pp1709-1717

[30] J.R.Groh, Effect of cooling rate from solution heat treatment on Wasploy microstructure and properties. Superalloy 1996, p621-626.

[31] W.I.Mitchel, Z.Metallk. 57, 586(1966)

[32] George.E.Dieter, Mechanical Metallurgy, McGraw-Hill Co., ISNB 0-07-016893-8, 1986

[33] Eckhard Nembach and Gunter Neite, Precipitation hardening of superalloys by ordered γ'-particles, Progress in Materials Science, Vol.29, 1985, p179

[34] R.F.Decker, Strengthening mechanism in nickel base superalloys.

[35] Jian Mao, Keh-Minn Chang, Wanhong Yang, Koushik Ray, Suhas Vaze and Dave Durrer, Metallurgy and Materials Transactions A, Vol.32A Oct. 2001, pp2441-2452

[36] Dave Furrer, Internal presentation, D.C. Washington, 2000

[37] W.H.Yang, W. Chen, K-M Chang, S. Mannan and J. deBarbardillo, Proceeding of the Ninth International Symposium on Superalloys, 2000, T.M Pollock, R.D.Kissinger, and R.R. Brown, et.al, eds., TMS, Warrendale, PA, pp75-84

[38] Jian Mao, Keh-Minn Chang, Wanhong Yang, Koushik Ray, Suhas Vaze and Dave Durrer, Materials Science and Engineering, Structure A, 2002, to be published.

[39] Keh-Minn Chang and Jian Mao, Internal report, West Virginia University, Morgantown, WV 26505, July, 2000

[40] K. Kusabiraki, Xiao-min Zhang, and Takayaki Ooka, Iron Steel Inst. Jpn. Int., 1995, Vol.35(9), pp1115-1120

[41] D. McLean, Predicting growth of γ' in Nickel alloys, Metal Science, Vol.18, May 1984, p249-256

Page: 140

[42] John D. Verhoeven, Physical Metallurgy (in Chinese), translated by Guangxi Li and Zhiwei Zhao, July, 1980

Page: 140

[43] R.A.Ricks, A.J.Porter and R.C.Ecob, The growth of γ' precipitates in Nickel base superalloys, Acta Metall. Vol.31, 1983, pp43-53

Page: 140

[44] N. Saunders and A.P. Miodownik, CALPHAD Calculation of phase diagram comprehensive guide, Pergamon materials series, Elsevier Science Limited, Pergamon, 1998.